

The role of electronic interactions for two-dimensional topological insulators



Habilitationsschrift

zur Erlangung der Lehrbefähigung für

Theoretische Physik

der Fakultät für Physik und Astronomie

der Julius-Maximilians-Universität Würzburg

vorgelegt von

Dr. Martin Hohenadler

Würzburg, im Juli 2016

Preface

This document constitutes my habilitation thesis (*Habilitationsschrift*), which is based on the publications listed on page v. It is intended to provide a unified, current, and accessible overview of my contributions to the field of correlated topological insulators. The level of detail of the discussion is a compromise between a self-contained presentation and the cumulative character of the thesis. Although a short overview of the relevant recent literature and references to more extensive reviews will be given, the thesis does not aim at or come close to summarising the entire body of work in this rapidly growing field. A more complete (at the time of writing) invited review article on the same topic has been published before in

- [1] M. Hohenadler, F. F. Assaad,
Correlation effects in two-dimensional topological insulators,
J. Phys.: Condens. Matter **25** (2013) 143201.

It is a pleasure to thank the people that have contributed in one way or another to the existence of this thesis. First and foremost, I'm grateful to Fakher Assaad for a very fruitful collaboration, and for getting me interested in the topic of topological insulators on my return to academia in 2008. I also want to thank Björn Trauzettel and Ralph Claessen, the other two members of the *Fachmentorat*, for their efforts and advice. Furthermore, I would like to acknowledge my collaborators Martin Bercx, Maria Daghofer, Igor Herbut, Thomas Lang, Zi Yang Meng, Alejandro Muramatsu (1951 – 2015), Francesco Parisen Toldin, Manuel Weber, and Stefan Wessel.

My work was financially supported by the Deutsche Forschungsgemeinschaft as part of the Forschergruppe 1807 and the Sonderforschungsbereich 1170, and benefited enormously from the generous allocation of computer time at the Jülich and Leibniz Supercomputing Centres.

Finally, any worthwhile enterprise also requires moral support, which came in particular from Holger Fehske and Joe Bhaseen, as well as from my dear wife Kathrin.

List of publications

- [A1] M. Hohenadler, T. C. Lang and F. F. Assaad,
Correlation Effects in Quantum Spin-Hall Insulators: A Quantum Monte Carlo Study,
Phys. Rev. Lett. **106** (2011), 100403.
- [A2] M. Hohenadler and F. F. Assaad,
Luttinger liquid physics and spin-flip scattering on helical edges,
Phys. Rev. B **85** (2012), 081106.
- [A3] M. Hohenadler, Z. Y. Meng, T. C. Lang, S. Wessel, A. Muramatsu and F. F. Assaad,
Quantum phase transitions in the Kane-Mele-Hubbard model,
Phys. Rev. B **85** (2012), 115132.
- [A4] F. F. Assaad, M. Bercx and M. Hohenadler,
*Topological Invariant and Quantum Spin Models from Magnetic π Fluxes
in Correlated Topological Insulators*,
Phys. Rev. X **3** (2013), 011015.
- [A5] M. Daghofer and M. Hohenadler,
Phases of correlated spinless fermions on the honeycomb lattice,
Phys. Rev. B **89** (2014), 035103.
- [A6] M. Weber, M. Hohenadler and F. F. Assaad,
Kondo screening of spin-charge separated fluxons by a helical liquid,
Phys. Rev. B **89** (2014), 205125.
- [A7] M. Hohenadler, F. Parisen Toldin, I. F. Herbut and F. F. Assaad,
Phase diagram of the Kane-Mele-Coulomb model,
Phys. Rev. B **90** (2014), 085146.
- [A8] M. Bercx, M. Hohenadler and F. F. Assaad,
Kane-Mele-Hubbard model on the π -flux honeycomb lattice,
Phys. Rev. B **90** (2014), 075140.
- [A9] M. Hohenadler and F. F. Assaad,
Rashba coupling and magnetic order in correlated helical liquids,
Phys. Rev. B **90** (2014), 245148.

For Maggie

‘Topology is destiny,’ he said, and put the drawers on. One leg at a time.

N. Stephenson, *Anathem*, 2008.

Contents

1	Introduction	1
2	Models	5
2.1	Dirac semimetal	5
2.2	Topological insulators	9
2.3	Interaction terms	16
3	Quantum Monte Carlo methods	19
3.1	Auxiliary-field method	21
3.2	CT-INT method	25
4	Bulk correlation effects	29
4.1	Phase diagram	30
4.2	Magnetic phase transition	34
4.3	Topological invariant from π -fluxes	38
5	Edge correlation effects	41
5.1	Effective model	42
5.2	Generic correlation effects	43
5.3	Edge-Mott transition	46
6	Topological Mott insulators	51
6.1	Existence of a topological Mott insulator	54
6.2	Charge-modulated phase	58
	Summary	61
	Zusammenfassung	63
	Bibliography	65

1 Introduction

At the beginning of the millennium, after decades of remarkable progress in our understanding of materials, it seemed almost certain that exciting new condensed matter physics would emerge from interaction or many-body effects rather than from single-particle properties. However, the experimental realisation of graphene—a two-dimensional Dirac semimetal at low energies [2, 3]—by Novoselov *et al.* [4] in 2004 had a major impact on both experimental and theoretical physics [5, 6]. While the band structure of graphene had been known theoretically before [2, 7], the work of Kane and Mele [8, 9] revealed that spin-orbit coupling can give rise to a new state of matter—a topological insulator with time-reversal symmetry and protected edge states. The latter was experimentally realised in semiconductor heterostructures [10] following theoretical proposals [11, 12]. Since then, it has become clear that topological insulators are only part of a remarkably rich set of phenomena, and topology has become a central topic in condensed matter physics. Introductions and surveys of the literature can be found in several reviews [1, 13–15] and books [16, 17].

Landau’s theory of second-order phase transitions [18] classifies matter in terms of spontaneously broken symmetries and the corresponding order parameters. Remarkably, topological insulators fall outside this classification because they are not distinguished from trivial insulators by a local order parameter. The same is true for the integer quantum Hall states of electrons in strong magnetic fields [19, 20]. For the latter, the quantised and robust Hall conductance $\sigma_{xy} = Ce^2/h$ can be related to an integer-valued topological invariant (the first Chern number C) calculated from a single-particle Hamiltonian of Landau levels [21–23]. States with different C are topologically distinct but have the same symmetries. As is well known, the nontrivial topological properties of quantum Hall states also manifest themselves in terms of characteristic metallic edge states [24]. Two-dimensional *topological insulators*¹ are conceptually closely related to integer quantum Hall states, as illustrated in figure 1.1. They are characterised by a Z_2 topological invariant $\nu = 1$, in contrast to trivial insulators which have $\nu = 0$ [8, 9]. The bulk is insulating, while the sample edges carry helical edge states in which the direction of motion is tied to the direction of spin [8, 9]. The edge states connect the valence and conduction bands, and have a crossing protected by time-reversal symmetry [8, 9]. While the latter implies $\sigma_{xy} = 0$, an electric field gives rise to spin currents due to a nonzero spin-Hall conductivity $\sigma_{xy}^{\text{spin}}$ [8, 9]. If spin is conserved, the quantum spin Hall insulator can be constructed from two integer quantum Hall states with opposite sign of the Hall conductivity [8, 25], and has a quantised spin-Hall response $\sigma_{xy}^{\text{spin}} = \pm e/2\pi$ [8]. The role of the external magnetic field is played by

¹The term *topological insulator* will be used for insulators with protected gapless edge or surface states, short-range entanglement, but no adiabatic connection to trivial band insulators. For the specific case of two-dimensional topological insulators protected by time-reversal symmetry, we shall also use the term *quantum spin Hall insulator*.

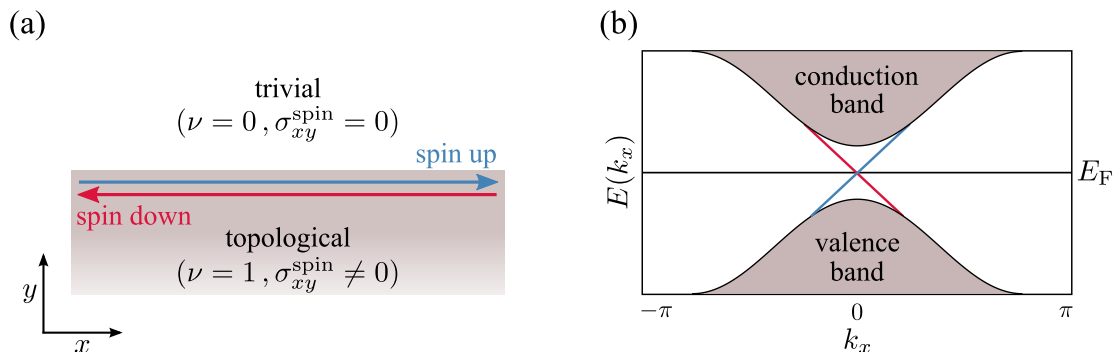


Figure 1.1: (a) Helical edge states at the interface between a topological insulator and a trivial insulator. (b) Corresponding band structure containing the bulk valence and conduction bands (grey-shaded), as well as the gapless edge states with a crossing at the Fermi level protected by time-reversal symmetry.

spin-orbit coupling that modifies the band structure, and the topological properties are hence intrinsic. Time-reversal symmetry is essential for the stability of topological insulators against disorder or interactions [8, 9]. Current experimental realisations are based on HgTe/CdTe or InAs/GaSb quantum well structures [10, 26].² Considerable experimental efforts are also being made to realise the two-dimensional topological insulator in honeycomb materials such as silicene [28, 29] and stanene [30, 31]. Z_2 topological insulators protected by time-reversal symmetry also exist in three dimensions [32, 33] and were first realised in bismuth selenide [34, 35]. More generally, the concept of symmetry-protected topological states extends to topological superconductors [36], topological crystalline insulators [37], Floquet topological insulators [38], and interacting systems [39]. A complete classification of single-particle Hamiltonians in terms of the generic time-reversal, particle-hole, and chiral symmetries has been given in [40, 41].

The present thesis reviews exact numerical results for the Mott transition—a key problem of condensed matter physics [42, 43]—of Dirac semimetals with long-range Coulomb repulsion, as well as for interaction-driven magnetic transitions in topological insulators both in the bulk and at the edge. Moreover, numerical findings regarding the existence of a topological Mott insulator [44]—with interaction-generated spin-orbit-like bond order—are discussed.

Correlated electrons in topological bands (Landau levels) have been studied extensively in the context of the fractional quantum Hall effect [20]. In contrast to topological insulators, fractional quantum Hall states have fractional quasi-particle excitations and cannot be adiabatically connected to noninteracting states. Similar to quantum spin liquids [45, 46], they are characterised by intrinsic topological order [47] and long-range quantum entanglement [48]. In close analogy to the noninteracting case, *fractional topological insulators* can be constructed by combining two fractional quantum Hall states [49]. On the experimental side, SmB₆ has been argued to be a correlated topological (Kondo) insulator [50], whereas Sr₂IrO₄ is a candidate

²The physics of this system is determined by the gap at the Γ point [12]. If the HgTe quantum well has a thickness $d < 6.3$ nm, the band structure is dominated by the surrounding CdTe layers, and the s (Γ_6) bands lie above the p (Γ_8) bands. For $d > 6.3$ nm, the band structure becomes dominated by that of the quantum well and band inversion takes place. The prediction that the inverted regime realises the quantum spin Hall insulator [12] was experimentally verified in [10, 27]. The helical edge states in HgTe had been predicted much earlier [11].

for a topological Mott insulator [51, 52]. Correlated helical edge states with tunable Luttinger parameters have been reported for InAs/GaSb [53]. A coexistence of strong correlations and strong spin-orbit coupling is also expected in Ir-based transition metal oxides [54], decorated graphene [55], and molecular graphene [56]. A time-reversal invariant spin liquid phase with helical edge states was predicted for Na_2IrO_3 [57]. Another promising direction are transition-metal oxide heterostructures (e.g., $\text{LaNiO}_3/\text{LaAlO}_3$), which provide substantial tunability [58, 59] and may realise topological phases either from intrinsic spin-orbit coupling [58] or from interaction-induced orbital order [60–63]. Z_2 topological insulators with tunable interactions may be accessible with cold atoms in artificial gauge fields [64, 65]. Finally, interacting Dirac fermions can also be engineered with electrons in artificial crystals [66] or molecular graphene [56], and with cold atoms in optical lattices [67].

Exact numerical methods, such as quantum Monte Carlo or exact diagonalisation, have played a key role for the progress in understanding strongly correlated electrons. They provide unbiased information about the properties of models that do not permit general analytical solutions. The applicability of such methods has increased significantly in recent decades as a result of the combined progress in computer hardware and algorithms. For certain classes of models, quantum Monte Carlo methods are free of a sign problem, allowing the simulation of system sizes large enough to investigate exotic quantum spin liquid phases [68] or the universality of phase transitions [69]. Nevertheless, while systems of bosons or non-frustrated spins can be solved to almost arbitrary accuracy, the simulation of fermions remains challenging. Therefore, the development of new algorithms is a central topic of current research. Numerical methods have predictive power, but can also be used to validate predictions based on mean-field theory or other approximations. Remarkably, certain models for correlated topological insulators can be simulated without a sign problem [A1, 70]. Quantum Monte Carlo results for the Kane-Mele model with electronic interactions will be reviewed in chapters 4 and 5. In contrast, the models proposed to support topological Mott insulators are not currently amenable to Monte Carlo simulations in the parameter region of interest, and have instead been investigated by exact diagonalisation and cluster methods, see chapter 6.

The thesis is organised as follows. Chapter 2 gives an introduction to honeycomb lattice models with or without spin-orbit coupling, which describe Dirac fermions and topological insulators, respectively. It also defines the different interaction terms considered. Chapter 3 explains the main aspects of the quantum Monte Carlo methods used. Bulk correlation effects in Dirac semimetals and topological insulators with either a Hubbard or a Coulomb interaction are reviewed in chapter 4. Interaction effects on the helical edge states of topological insulators are the subject of chapter 5. Chapter 6 is devoted to numerical results regarding the topological Mott insulator. Brief summaries in English and German are given, and the appendix contains the original publications listed on page v.

2 Models

The two-dimensional topological insulator can be realised in a variety of microscopic models. While a review of other models can be found in [1], here we only discuss the Kane-Mele model defined on the honeycomb lattice, from which Kane and Mele originally deduced the existence of two-dimensional topological insulators exhibiting the quantum spin Hall effect [8, 9]. Another model of great significance is the tight-binding model of Bernevig, Hughes, and Zhang for HgTe quantum wells [12].¹ The two key ingredients of the Kane-Mele model are nearest-neighbour electronic hopping and spin-orbit coupling. In the absence of spin-orbit coupling,² the hopping term gives rise to a gapless, linear band dispersion at isolated points in the Brillouin zone, as realised in graphene [3, 5, 7]. Remarkably, the low-energy physics of graphene is described by massless Dirac fermions [2]. Spin-orbit coupling opens a gap in the band structure and gives rise to a topological insulator [8, 9]. While not observable in graphene, direct experimental realisations of the topological phase of the Kane-Mele model seem possible in other honeycomb materials with significantly stronger spin-orbit coupling [72]. The Kane-Mele model can be combined with different forms of electron-electron interactions to model correlated Dirac fermions or topological insulators. Importantly, the symmetries of the model allow the application of exact quantum Monte Carlo methods without a sign problem [A1], see chapter 3. Here, we first introduce the honeycomb lattice and discuss the relation between graphene and Dirac fermions, before exploring how topological insulators emerge from spin-orbit coupling.³ Finally, we define the interaction terms considered in chapters 4–6.

2.1 Dirac semimetal

Graphene is a two-dimensional, hexagonal or honeycomb lattice of carbon atoms, as shown in figure 2.1(a), with a lattice constant $a = 0.142$ nm [5]. The lattice can be considered to be a triangular Bravais lattice with a two-site unit cell and lattice spacing $\sqrt{3}a$. The sublattices are commonly denoted as A and B. The lattice vectors can be chosen as⁴ [see figure 2.1(a)] [73]

$$\mathbf{a}_1 = \sqrt{3} \mathbf{e}_x, \quad \mathbf{a}_2 = \frac{\sqrt{3}}{2} (\mathbf{e}_x + \sqrt{3} \mathbf{e}_y). \quad (2.1)$$

¹See footnote 13 on page 11.

²The spin-orbit gap in graphene is approximately 10 mK and therefore not observable experimentally [71].

³The discussion will be partly based on references [13, 16, 73].

⁴In this introductory chapter, we set $a = 1$. In contrast, $\sqrt{3}a = 1$ in some of the original papers, see also page 16.

2.1. Dirac semimetal

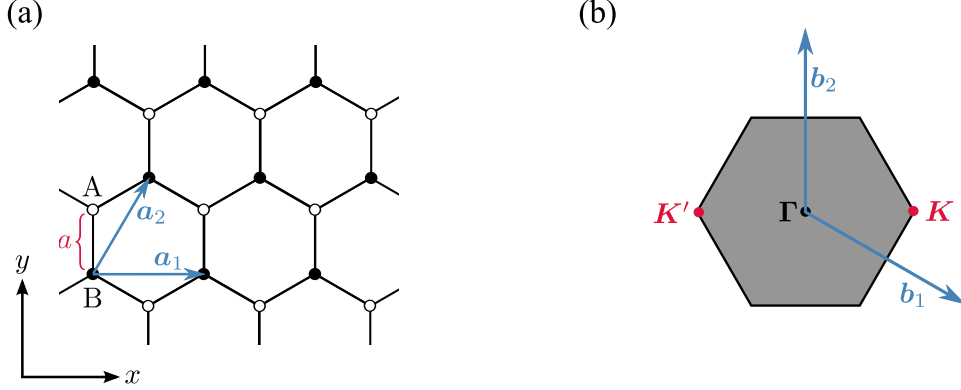


Figure 2.1: (a) The honeycomb lattice, a triangular lattice with a two-site (A, B) unit cell and lattice constant $\sqrt{3}a$. The basis vectors are \mathbf{a}_1 and \mathbf{a}_2 [equation (2.1)]. (b) The Wigner-Seitz construction gives a hexagonal first Brillouin zone containing the Dirac points K and K' [equation (2.3)]; \mathbf{b}_1 and \mathbf{b}_2 [equation (2.2)] are the basis vectors of the reciprocal lattice fulfilling $\mathbf{a}_i \cdot \mathbf{b}_j = 2\pi\delta_{ij}$.

The basis vectors of the reciprocal lattice are given by

$$\mathbf{b}_1 = \frac{2\pi}{\sqrt{3}} \left(\mathbf{e}_x - \frac{1}{\sqrt{3}}\mathbf{e}_y \right), \quad \mathbf{b}_2 = \frac{4\pi}{\sqrt{3}} \mathbf{e}_y, \quad (2.2)$$

and the first Brillouin zone takes the form of a hexagon, see figure 2.1(b). The zone corners, only two of which (K and K') are inequivalent, are referred to as the *Dirac points*. Here, we use the choice shown in figure 2.1(b),

$$\mathbf{K} = \frac{4\pi}{3\sqrt{3}} \mathbf{e}_x, \quad \mathbf{K}' = -\mathbf{K}. \quad (2.3)$$

Hybridisation of the 2s and 2p orbitals leads to three $2sp^2$ orbitals oriented in the xy -plane with a mutual angle of 120° , and a $2p_z$ orbital perpendicular to the plane. In the two-dimensional lattice, the planar orbitals form bonds with three neighbouring carbon atoms. The perpendicular orbitals give rise to a valence (π) and a conduction (π^*) band that determine the electronic properties. In the absence of dopants graphene has two electrons per unit cell (one electron per site) corresponding to a completely filled valence band.

A minimal tight-binding description takes into account nearest-neighbour hopping of electrons. As illustrated in figure 2.2(a), such processes connect the A and B sublattices and are described by vectors $\pm\boldsymbol{\delta}_i$ with

$$\boldsymbol{\delta}_1 = \frac{1}{2} \left(\sqrt{3}\mathbf{e}_x + \mathbf{e}_y \right), \quad \boldsymbol{\delta}_2 = \frac{1}{2} \left(-\sqrt{3}\mathbf{e}_x + \mathbf{e}_y \right), \quad \boldsymbol{\delta}_3 = -\mathbf{e}_y. \quad (2.4)$$

The tight-binding Hamiltonian can be written as⁵

$$\hat{H}_t = -t \sum_{\langle i,j \rangle} \sum_s c_{is}^\dagger c_{js} = -t \sum_{\langle i,j \rangle} \mathbf{c}_i^\dagger \mathbf{c}_j \quad (2.5)$$

⁵The notation $\langle i,j \rangle$ implies summation over $c_i^\dagger c_j$ and its Hermitian conjugate $c_j^\dagger c_i$.

where t is the hopping integral and we introduced the spinor $\mathbf{c}_i^\dagger = (c_{i\uparrow}^\dagger, c_{i\downarrow}^\dagger)$. The operator c_{is}^\dagger creates a π electron with spin s at lattice site i .

To derive the band structure we introduce operators $a_{ls}^\dagger, b_{ls}^\dagger$ acting on the A and B sites of unit cell l , respectively. For each of the two spin directions, Fourier transformation then gives the 2×2 matrix representation

$$\mathcal{H}(\mathbf{k}) = \begin{pmatrix} 0 & -g^*(\mathbf{k}) \\ -g(\mathbf{k}) & 0 \end{pmatrix} \quad (2.6)$$

with $g(\mathbf{k}) = 1 + e^{i\mathbf{k}\cdot\mathbf{a}_2} + e^{i\mathbf{k}\cdot\mathbf{a}_3}$ and energy eigenvalues [7]

$$E^\pm(\mathbf{k}) = \pm|g(\mathbf{k})| = \pm t \sqrt{3 + 2 \cos(\sqrt{3}k_x) + 4 \cos(3k_y/2) \cos(\sqrt{3}k_x/2)}, \quad (2.7)$$

where E^- (E^+) corresponds to the valence (conduction) band. As illustrated in figure 2.2(b), the valence and conduction bands touch at the six zone corners of the first Brillouin zone,⁶ near which the spectrum is linear and isotropic. The graphene band structure exhibits inversion, time-reversal, and particle-hole symmetry.⁷ If the Fermi level E_F lies exactly at zero energy, as is the case for undoped graphene, the system is a semimetal with zero density of states at E_F but gapless excitations. The density of states vanishes linearly on approaching E_F , $N(\epsilon) \sim |\epsilon|$ for $\epsilon = E - E_F \ll t$ [7]. As confirmed experimentally [3], the semimetal is stable with respect to weak interactions. At strong coupling, it can undergo a variety of symmetry-breaking phase transitions, see chapters 4 and 6.

The connection to Dirac fermions at low energies can be revealed by expanding the energies around the gapless Dirac points using $\mathbf{k} = \pm\mathbf{K} + \mathbf{q}$ with $|\mathbf{q}| \ll 1$. Interchanging the spinor components of A and B sublattices near \mathbf{K}' this leads to [73]

$$\mathcal{H}(\pm\mathbf{K} + \mathbf{q}) = \pm v_F (q_x \sigma^x + q_y \sigma^y), \quad (2.8)$$

with the Fermi velocity $v_F = 3t/2\hbar$, about 300 times smaller than the speed of light in vacuum [73]. Equation (2.8) has the Dirac-Weyl form $\mathcal{H}(\mathbf{p}) = \pm\boldsymbol{\sigma} \cdot \mathbf{p}$ with energies $E(\mathbf{p}) = \pm\hbar|\mathbf{p}|$. Hence, neglecting the physical spin of the electrons, the low-energy excitations in graphene resemble two *flavours* (valley \mathbf{K} and valley \mathbf{K}' , or left-handed and right-handed) of massless Dirac fermions with a *pseudospin* degree of freedom σ corresponding to the wavefunction components on the A and B sublattices. Excitations near a given Dirac point also have definite eigenvalues of the helicity operator $\boldsymbol{\sigma} \cdot \mathbf{p}/|\mathbf{p}|$. The resulting locking of pseudospin and momentum suppresses intravalley backscattering $\mathbf{q} \rightarrow -\mathbf{q}$ and underlies the high carrier mobility of graphene [75].

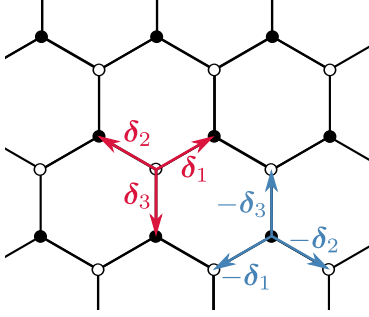
While it has become common in the literature to use the term Dirac fermion more loosely, the low-energy excitations in graphene indeed have all the required properties. In spatial dimension $d \geq 1$,⁸ Dirac particles with mass m are described by a Hamiltonian $\mathcal{H} = \boldsymbol{\alpha} \cdot \mathbf{p} + \beta m$, where

⁶The location at the zone corners is due to the C_3 rotational symmetry of the triangular Bravais lattice.

⁷The bands are spin-degenerate, $E_\uparrow^\pm(\mathbf{k}) = E_\downarrow^\pm(\mathbf{k}) = E^\pm(\mathbf{k})$, which follows from the combination of space inversion symmetry [$E_s^\pm(\mathbf{k}) = E_s^\pm(-\mathbf{k})$] and time-reversal symmetry [$E_\uparrow^\pm(\mathbf{k}) = E_\downarrow^\pm(-\mathbf{k})$] [74]. Finally, considering only nearest-neighbour hopping, the spectrum also exhibits particle-hole symmetry [$E_s^\pm(\mathbf{k}) = -E_s^\mp(\mathbf{k})$] [73].

⁸See [76] for a concise discussion of Dirac Hamiltonians and their symmetries in different dimensions.

(a) hopping



(b) band structure

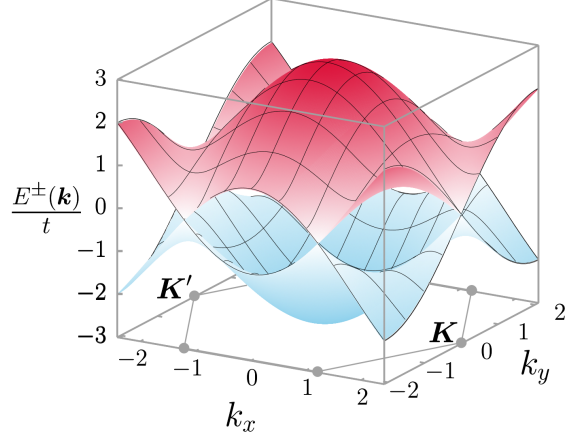


Figure 2.2: (a) Nearest-neighbour hopping is described by the vectors $\pm\delta_i$ [equation (2.4)]. (b) Band structure of the model (2.5) with a gapless, linear dispersion near the Dirac points \mathbf{K} and \mathbf{K}' .

the matrix β and the d -dimensional vector of matrices α depend on d . Symmetries impose conditions on the form of α and β [76]. A relativistically covariant representation is given by $\mathcal{H} = \gamma^\mu P_\mu - m$ with the $(d + 1)$ -momentum P_μ . The matrices γ^μ ($\mu = 0, 1, \dots, d$) fulfil the Clifford algebra, $\{\gamma^\mu, \gamma^\nu\} = 2g^{\mu\nu}$. For $d = 3$, they are 4×4 matrices, and there exists an additional matrix γ^5 that commutes with the others and generates the chiral symmetry of massless Dirac fermions. The latter implies the conservation of the left- and right-handed components and is broken for $m \neq 0$ [77]. For $d = 2$ and a single flavour, the 2×2 matrices $\gamma^0, \gamma^1, \gamma^2$ can be expressed in terms of the Pauli matrices $\sigma^x, \sigma^y, \sigma^z$. Since there is no additional matrix that commutes with all γ 's, chiral symmetry is undefined and the massive and massless cases have the same symmetry [78].

At low energies graphene corresponds to two flavours of Dirac fermions [equation (2.8)]. Defining the bi-spinor fields [u (v) denotes the component on the A (B) sublattice]

$$\Psi^\dagger(\mathbf{q}) = (u^\dagger(\mathbf{K} + \mathbf{q}), v^\dagger(\mathbf{K} + \mathbf{q}), u^\dagger(-\mathbf{K} + \mathbf{q}), v^\dagger(-\mathbf{K} + \mathbf{q})) , \quad (2.9)$$

and the corresponding slowly-varying field $\Psi^\dagger(\mathbf{x}) = \int^\Lambda \frac{d^2q}{(2\pi)^2} e^{i\mathbf{q}\cdot\mathbf{x}} \Psi^\dagger(\mathbf{q})$ with ultra-violet cutoff Λ , the low-energy physics is described by the Hamiltonian density [8]

$$\mathcal{H} = -i\hbar v_F \Psi^\dagger(\mathbf{x}) (\tau^z \otimes \sigma^x \partial_x + \tau^0 \otimes \sigma^y \partial_y) \Psi(\mathbf{x}) . \quad (2.10)$$

Here, the Pauli matrices σ^α act in sublattice (pseudospin) space whereas the τ^α act in valley (flavour) space.⁹ For $\hbar = v_F = 1$ the corresponding Lagrangian can be written as [79, 80]

$$\mathcal{L}_0 = \bar{\Psi}(\mathbf{x}, \tau) \gamma^\mu \partial_\mu \Psi(\mathbf{x}, \tau) \quad (2.11)$$

⁹We also define the matrices σ^0, τ^0 , and s^0 corresponding to 2×2 identity matrices.

with $\bar{\Psi} = \Psi^\dagger \gamma^0$, $\partial_\mu = (\partial_\tau, \nabla)$, and the 4×4 matrices $\gamma^0 = \tau^0 \otimes \sigma^z$, $\gamma^1 = \tau^z \otimes \sigma^y$, and $\gamma^2 = \tau^0 \otimes \sigma^x$ that fulfil the Euclidean Clifford algebra $\{\gamma^\mu, \gamma^\nu\} = 2\delta_{\mu\nu}$. Given two flavours, there exist additional matrices $\gamma^3 = \tau^x \otimes \sigma^y$, $\gamma^5 = \tau^y \otimes \sigma^y$, and $\gamma^{35} = -i\gamma^3\gamma^5$ that commute with $\gamma^0, \gamma^1, \gamma^2$ and generate a chiral symmetry [81]. Similarly, time-reversal, inversion, and translation symmetry can be defined in terms of the γ matrices [81]. Of particular importance for the discussion below will be time reversal (which in the spinless case corresponds to an exchange of the Dirac points) and inversion (exchange of the sublattice components) [81]. Finally, the physical spin s doubles the number of components to eight. Adding a spin index to equation (2.9) and redefining $\Psi^\dagger = (\Psi_\uparrow^\dagger, \Psi_\downarrow^\dagger)$ the Lagrangian becomes [79, 80]¹⁰

$$\mathcal{L}_0 = \bar{\Psi}(\mathbf{x}, \tau) (s^0 \otimes \gamma^\mu) \partial_\mu \Psi(\mathbf{x}, \tau). \quad (2.12)$$

2.2 Topological insulators

While the Dirac character of the low-energy excitations in graphene is extremely interesting in its own right, Kane and Mele [8, 9] showed that spin-orbit coupling gives rise to an entirely new state of matter, namely the two-dimensional topological insulator introduced in chapter 1. Here, using the Kane-Mele model, we will illustrate how this state emerges from a microscopic Hamiltonian, how it can be identified from the Z_2 topological invariant and the characteristic edge states, and how it relies on time-reversal symmetry.

Our starting point is the Kane-Mele model of graphene [8, 9], which takes into account nearest-neighbour hopping and spin-orbit coupling. We write the Hamiltonian as

$$\hat{H}_{\text{KM}} = -t \sum_{\langle i,j \rangle} \mathbf{c}_i^\dagger \mathbf{c}_j + i\lambda \sum_{\langle\langle i,j \rangle\rangle} \mathbf{c}_i^\dagger (\mathbf{v}_{ij} \cdot \mathbf{s}) \mathbf{c}_j. \quad (2.13)$$

Here, $\mathbf{c}_i^\dagger = (c_{i\uparrow}^\dagger, c_{i\downarrow}^\dagger)$ as before. The first term is identical to equation (2.5), while the second term describes spin-orbit coupling [8, 9]. It corresponds to a complex-valued next-nearest-neighbour hopping term with amplitude $\pm i\lambda$ defined in terms of a vector \mathbf{v}_{ij} (see below) and the Pauli vector $\mathbf{s} = (s^x, s^y, s^z)$ acting on the physical spin s . As shown below, the sign depends on the spin, the sublattice, and the direction of the hop (left-turn or right-turn to get from j to i).

As illustrated in figure 2.3(a), hopping between next-nearest-neighbour pairs $\langle\langle i, j \rangle\rangle$ connects sites on the same sublattice and is described by the vectors \mathbf{a}_1 , \mathbf{a}_2 [defined in equation (2.1)], and $\mathbf{a}_3 = \mathbf{a}_2 - \mathbf{a}_1$. To determine the sign of the spin-orbit term for given $\langle\langle i, j \rangle\rangle$ the hop from, say j to i (and likewise for i to j) is decomposed into a hop from j to the intermediate site k , followed by a hop from k to i . The unit vector \mathbf{v}_{ij} in equation (2.13) is then defined as

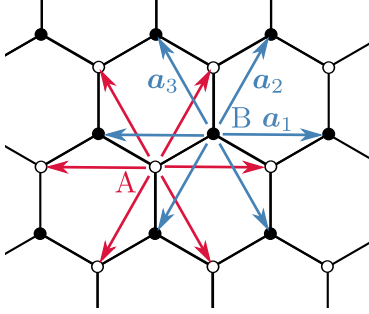
$$\mathbf{v}_{ij} = \frac{\mathbf{d}_{jk} \times \mathbf{d}_{ki}}{|\mathbf{d}_{jk} \times \mathbf{d}_{ki}|}, \quad (2.14)$$

where \mathbf{d}_{jk} and \mathbf{d}_{ki} connect site j to site k and site k to site i , respectively, and can be expressed in terms of $\boldsymbol{\delta}_i$ [see figure 2.2(a)]. The vector \mathbf{v}_{ij} is perpendicular to the xy -plane of the honeycomb

¹⁰In the following, identity matrices and tensor products are suppressed if no confusion can arise.

2.2. Topological insulators

(a) spin-orbit coupling



(b) band structure

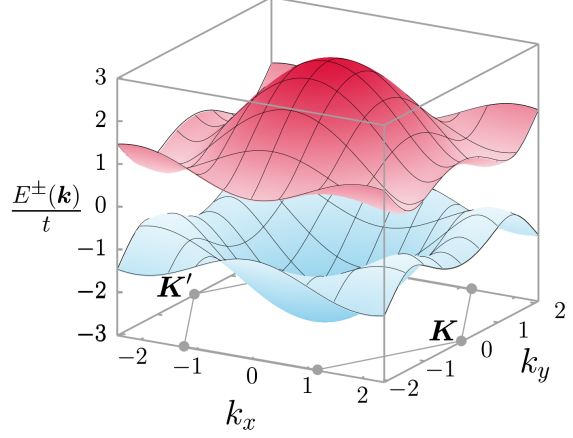


Figure 2.3: (a) Spin-orbit terms described by the vectors $\pm\mathbf{a}_i$, see also figure 6.2(a). (b) Band structure of the Kane-Mele model with a spin-orbit gap Δ_{SO} . Here, $\lambda/t = 0.1$.

lattice. Hence, $\mathbf{v}_{ij} \cdot \mathbf{s} = v_{ij}^z s^z = \pm s^z$.¹¹ Choosing the z -direction as the spin quantisation axis, we see that the spin-orbit term conserves S^z but reduces the spin-symmetry from $\text{SU}(2)$ to $\text{U}(1)$.

Similar to the tight-binding Hamiltonian (2.5), we diagonalise the Kane-Mele model by Fourier transformation. Because of spin-orbit coupling, we use the basis $(a_{\mathbf{k}\uparrow}^\dagger, b_{\mathbf{k}\uparrow}^\dagger, a_{\mathbf{k}\downarrow}^\dagger, b_{\mathbf{k}\downarrow}^\dagger)$ to obtain the matrix representation

$$\mathcal{H}(\mathbf{k}) = \begin{pmatrix} \gamma(\mathbf{k}) & -g^*(\mathbf{k}) & 0 & 0 \\ -g(\mathbf{k}) & -\gamma(\mathbf{k}) & 0 & 0 \\ 0 & 0 & -\gamma(\mathbf{k}) & -g^*(\mathbf{k}) \\ 0 & 0 & -g(\mathbf{k}) & \gamma(\mathbf{k}) \end{pmatrix} \quad (2.15)$$

with $g(\mathbf{k})$ as in equation (2.7) and the spin-orbit contribution

$$\gamma(\mathbf{k}) = 2\lambda \left[2 \cos(3k_y/2) \sin(\sqrt{3}k_x/2) - \sin(\sqrt{3}k_x) \right]. \quad (2.16)$$

The eigenvalues are

$$E^\pm(\mathbf{k}) = \pm \sqrt{|g(\mathbf{k})|^2 + [\gamma(\mathbf{k})]^2}, \quad (2.17)$$

and reduce to the graphene dispersion (2.7) in the limit $\lambda = 0$. The spin-orbit coupling opens a gap $\Delta_{\text{SO}} = 3\sqrt{3}\lambda$ at the Dirac points [8, 82]. As for graphene, the resulting bands are Kramers degenerate and particle-hole symmetric. If the gap is small, the low-energy theory corresponds to massive Dirac fermions [8],

$$\mathcal{H} = -i\hbar v_F \Psi^\dagger(\mathbf{x}) (\tau^z \sigma^x \partial_x + \sigma^y \partial_y) \Psi(\mathbf{x}) + \Delta_{\text{SO}} \Psi^\dagger(\mathbf{x}) s^z \tau^z \sigma^z \Psi(\mathbf{x}), \quad (2.18)$$

¹¹For example, the hop on sublattice A in the \mathbf{a}_1 direction in figure 2.3(a) corresponds to $\mathbf{d}_{jk} = \boldsymbol{\delta}_1$, $\mathbf{d}_{ki} = -\boldsymbol{\delta}_2$, and $v_{ij}^z = -1$ (right turn). The corresponding hop on sublattice B has $\mathbf{d}_{jk} = -\boldsymbol{\delta}_2$, $\mathbf{d}_{ki} = \boldsymbol{\delta}_1$, and $v_{ij}^z = +1$ (left turn). By definition, $\mathbf{v}_{ji} = -\mathbf{v}_{ij}$. The spin-orbit terms for spin-up electrons are illustrated in figure 6.2(a).

with excitation energies $E^\pm(\mathbf{q}) = \pm\sqrt{(\hbar v_F|\mathbf{q}|)^2 + \Delta_{\text{SO}}^2}$ and \mathbf{q} again defined relative to \mathbf{K} or \mathbf{K}' .

The topological aspects of the Kane-Mele model and their implications are most easily understood by recognising that the Hamiltonian matrix in equation (2.15) has the block form

$$\mathcal{H}(\mathbf{k}) = \begin{pmatrix} h(\mathbf{k}) & 0 \\ 0 & h^*(-\mathbf{k}) \end{pmatrix}. \quad (2.19)$$

Here, the upper (lower) 2×2 block describes spin-up (spin-down) electrons, and the blocks are related by time-reversal, $\Theta h(\mathbf{k})\Theta^{-1} = h^*(-\mathbf{k})$, with $\Theta = K$ (complex conjugation) for spinless fermions [83]. The block structure arises because Hamiltonian (2.13) conserves S^z .¹² Equation (2.19) has the generic form of a two-band Hamiltonian with time-reversal symmetry and spin conservation. The same structure is also obtained for the Bernevig-Hughes-Zhang model [12], which describes the low-energy physics of HgTe quantum wells.¹³

The two-band Hamiltonian $h(\mathbf{k})$ corresponds to the momentum-space representation of the spinless Haldane model [86]

$$\hat{H}_{\text{H}} = -t \sum_{\langle i,j \rangle} c_i^\dagger c_j - t_2 \sum_{\langle\langle i,j \rangle\rangle} e^{i\phi_{ij}} c_i^\dagger c_j, \quad (2.20)$$

also defined on the honeycomb lattice. The first term describes nearest-neighbour hopping, the second term a next-nearest-neighbour hopping with a Berry phase $e^{\pm i\phi}$ due to a staggered magnetic flux through the lattice [86]. Setting $\phi = \pi/2$ and $t_2 = \lambda$ produces hopping terms $i\lambda v_{ij}^z$ and Hamiltonian (2.20) becomes identical to one spin sector of the Kane-Mele model (2.13). Conversely, the Kane-Mele model can be written as two copies of the Haldane model by imposing opposite signs for the Berry phases for spin-up and spin-down electrons [8]. While the Haldane model has only been realised using cold atoms [87], the Kane-Mele model arises naturally from spin-orbit coupling in topological insulators [10].

The gapless Dirac spectrum of $h(\mathbf{k})$ is protected by time-reversal and inversion symmetry. A nonzero t_2 breaks time-reversal symmetry,¹⁴ and allows for a nonzero Hall conductivity. The Haldane model realises the integer quantum Hall effect with $\sigma_{xy} = \pm e^2/h$ in the absence of a net magnetic field [86].¹⁵ The spinless low-energy theory takes the form

$$\mathcal{H}_{\text{H}} = -i\hbar v_F \Psi^\dagger(\mathbf{x}) (\tau^z \sigma^x \partial_x + \sigma^y \partial_y) \Psi(\mathbf{x}) + m \Psi^\dagger(\mathbf{x}) \tau^z \sigma^z \Psi(\mathbf{x}). \quad (2.21)$$

The Hall conductivity can be calculated by coupling the Dirac fermions to a weak electromagnetic field [2, 86, 88]. The low-energy gauge theory contains a topological Chern-Simons

¹² S^z -conservation is not generic for quantum spin Hall systems. However, nonconserving Rashba terms (discussed below) are not essential to understand the topological phase.

¹³The model is defined on the square lattice, with two orbitals per site. It contains orbital-dependent onsite energies and intra- as well as interorbital hopping terms. Spin-orbit coupling connects s and p orbitals at neighbouring sites. In contrast to the Kane-Mele model, there exist two distinct topological phases separated by a gapless point [84]. The existence of two orbitals per site suggests that a sensible modelling of Coulomb repulsion should include Hund coupling [85], in contrast to the Kane-Mele model where a simple Hubbard term is sufficient.

¹⁴Time-reversal symmetry requires $\Theta h(\mathbf{k})\Theta^{-1} = h(-\mathbf{k})$, that is $\gamma(\mathbf{k}) = 0$.

¹⁵Systems exhibiting $\sigma_{xy} \neq 0$ without a magnetic field are also called *quantum anomalous Hall-* or *Chern insulators*.

2.2. Topological insulators

term [20, 89]. Each flavour contributes $\pm e^2/2h$ to the Hall conductivity, with the sign determined by the sign of the mass at \mathbf{K} and \mathbf{K}' , respectively [16]. For the Haldane model (2.20), the matrix τ^z in the mass term implies $m_{\mathbf{K}'} = -m_{\mathbf{K}}$, which breaks time-reversal symmetry corresponding to invariance under exchange of the Dirac points [81]. The total Hall conductivity is $\sigma_{xy} = \pm e^2/h$. The even number of flavours and the resulting integer quantisation of σ_{xy} are a consequence of fermion-doubling on a lattice [90]. In contrast, a mass term $m \Psi^\dagger \sigma^z \Psi$ due to a staggered potential ($+\epsilon$ on sublattice A, $-\epsilon$ on sublattice B) preserves time-reversal symmetry and gives $m_{\mathbf{K}'} = m_{\mathbf{K}}$ as well as $\sigma_{xy} = 0$ [16].

The quantised Hall conductivity can also be obtained without invoking the continuum limit. The relation between the momentum-space topology of wavefunctions and the quantisation of σ_{xy} was first established in [21]. The Hall conductivity has the form $\sigma_{xy} = (e^2/h) \sum_m C_m$ and involves the sum over the integer Chern numbers C_m of the occupied bands. For a two-band system, the Chern number of the valence band is given by

$$C = \frac{1}{2\pi} \int d^2k \mathcal{F}(\mathbf{k}), \quad (2.22)$$

and corresponds to the total Berry flux through the Brillouin zone [21–23, 91]. Here, $\mathcal{F}(\mathbf{k}) = \nabla_{\mathbf{k}} \times \mathcal{A}(\mathbf{k})$, with the Berry phase $\mathcal{A}(\mathbf{k}) = i \langle u | \nabla_{\mathbf{k}} | u \rangle$ whose line-integral around a closed loop in momentum space gives the phase picked up by the Bloch state $|u\rangle$ [91]. In the Haldane model, a nonzero total Hall conductivity arises from the existence of two half-skyrmions of opposite topological charge at \mathbf{K} and \mathbf{K}' [16].

For two-band models, a simpler expression for σ_{xy} can be derived. Writing $\mathbf{h}(\mathbf{k})$ from equation (2.19) in the form $\mathbf{h}(\mathbf{k}) \cdot \boldsymbol{\sigma}$, and assuming an insulating system with the Fermi level in the gap, the Kubo formula gives for σ_{xy} at zero temperature [92]

$$\sigma_{xy} = -\frac{e^2}{h} Q, \quad Q = \frac{1}{4\pi} \int d^2k \hat{\mathbf{h}} \cdot (\partial_{k_x} \hat{\mathbf{h}} \times \partial_{k_y} \hat{\mathbf{h}}). \quad (2.23)$$

with $\hat{\mathbf{h}} = \mathbf{h}/|\mathbf{h}|$. Q takes on integer values and corresponds to the winding number of the mapping from the Brillouin zone to the unit sphere defined by $\hat{\mathbf{h}}$ [16, 92, 93].

As observed experimentally, the quantisation of σ_{xy} is robust with respect to interactions, disorder, and sample imperfections. Within the Haldane model, this can be understood from the fact that the winding number of $\hat{\mathbf{h}}$ cannot change as a result of small variations of the model parameters. Instead, a change of Q requires a closing of the gap, corresponding to a singularity of $\hat{\mathbf{h}}$. Such a change occurs at the interface between a region with $m_{\mathbf{K}'} = -m_{\mathbf{K}}$ (topological) and a region with $m_{\mathbf{K}'} = m_{\mathbf{K}}$ (trivial), see figure 2.4(a). Keeping $m_{\mathbf{K}}$ fixed, the interface can be modelled as a domain wall in the mass $m_{\mathbf{K}'} = m_{\mathbf{K}'}(y)$ which changes from $m_{\mathbf{K}'} = -m_{\mathbf{K}}$ to $m_{\mathbf{K}'} = +m_{\mathbf{K}}$ [16]. Similar to solitons in polyacetylene [94, 95], the domain wall gives rise to a zero-mode localised around the interface in the y -direction, but delocalised in the x -direction along the interface or edge. Fermions can propagate along the interface in only one direction ($+x$ or $-x$) with dispersion $\epsilon(k_x) = \pm \hbar v_F k_x$ depending on the signs of the masses, and form a *chiral liquid*. The existence of a chiral liquid at the interface can also be deduced by imposing gauge invariance on the effective Chern-Simons theory on a geometry with open

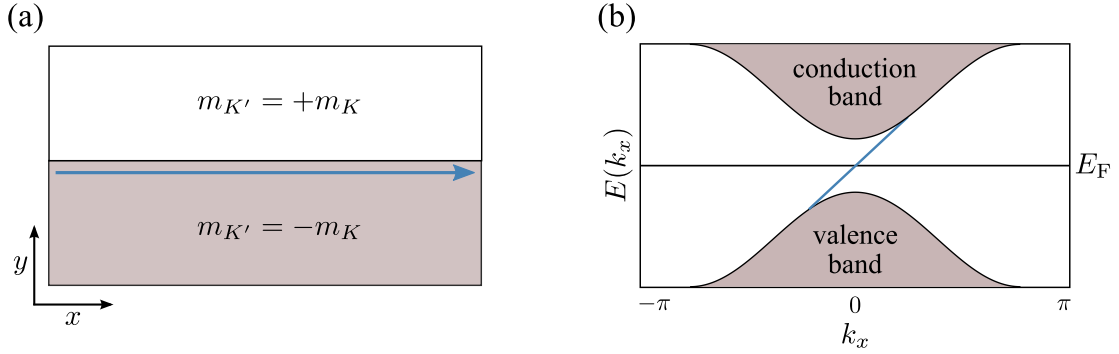


Figure 2.4: (a) Chiral edge state at the interface between a Chern insulator ($m_{K'} = -m_K$) and a trivial insulator ($m_{K'} = m_K$). (b) Corresponding band structure with the bulk valence and conduction bands (grey-shaded) and the gapless chiral edge state.

boundaries [96], or by solving the Haldane model numerically on a geometry with edges [8]. The equivalence of the bulk and edge topological invariants was first shown in [97].

Having established the nontrivial topological properties of the Haldane model with $m_{K'} = -m_K$, we now return to the Kane-Mele model. The mass term in equation (2.21) implies $m_{K'}^s = -m_K^s$, $m_K^\uparrow = -m_K^\downarrow$, and $m_{K'}^\uparrow = -m_{K'}^\downarrow$. Accordingly, $\sigma_{xy}^\uparrow = -\sigma_{xy}^\downarrow$ and $\sigma_{xy} = \sigma_{xy}^\uparrow + \sigma_{xy}^\downarrow = 0$, consistent with the time-reversal symmetry of the Kane-Mele model.¹⁶ Remarkably, while $\sigma_{xy} = 0$ implies the absence of a nonzero Chern number, not all time-reversal invariant Hamiltonians in two dimensions are equivalent. Instead, they fall into one of two classes distinguished by a Z_2 index $\nu = 0, 1$. Systems with $\nu = 0$ are adiabatically connected to trivial band insulators, while those with $\nu = 1$ correspond to topological insulators [8, 9].

The Kane-Mele model (2.13) with $\lambda \neq 0$ is a topological insulator with spin-Hall conductivity $\sigma_{xy}^{\text{spin}} = (\hbar/2e)(\sigma_{xy}^\uparrow - \sigma_{xy}^\downarrow) = \pm e/2\pi$ [8, 98] (the sign depends on the sign of λ). It therefore supports a spin current $\mathbf{J}^{\text{spin}} = (\hbar/2e)(\mathbf{J}^\uparrow - \mathbf{J}^\downarrow)$ in an applied electric field. The topological invariant ν can be defined as $\nu = C^{\text{spin}} \bmod 2$ [13] with the spin Chern number $C^{\text{spin}} = (C^\uparrow - C^\downarrow)/2 = \pm 1$ [98, 99] and the Chern numbers C^s of the two independent Haldane systems. In this case, we can write $\sigma_{xy}^{\text{spin}} = \pm \nu e/2\pi$ in analogy with the integer quantum Hall effect. Because the Kane-Mele model combines two copies of the Haldane model, the above reasoning regarding the existence of zero-modes or edge states also carries over. Each spin direction contributes one chiral edge mode per edge. At a given edge we hence have two counter-propagating and spin-polarised modes, exactly the helical edge modes schematically illustrated in figure 1.1. Figure 2.5(a) shows a zigzag ribbon geometry with edges parallel to the x -axis. Spin-up electrons move along the positive x -direction at the upper edge, while spin-down electrons move in the opposite direction. At the bottom edge, the directions are reversed. The numerically calculated spectrum is shown in figure 2.5(b), revealing the gapped bulk states with spin-orbit gap Δ_{SO} and

¹⁶ For spin-1/2 particles, time-reversal is described by $\Theta = e^{i\pi\sigma^y} K$, corresponding to a spin flip plus complex conjugation [83]. Hamiltonian (2.15) is symmetric under time-reversal: $\Theta \mathcal{H}(\mathbf{k}) \Theta^{-1} = \mathcal{H}(-\mathbf{k})$. At the field-theory level, time-reversal involves a spin flip and the exchange of \mathbf{K} and \mathbf{K}' ; the combination of these two operations leaves the spin-orbit mass term in equation (2.21) invariant.

2.2. Topological insulators

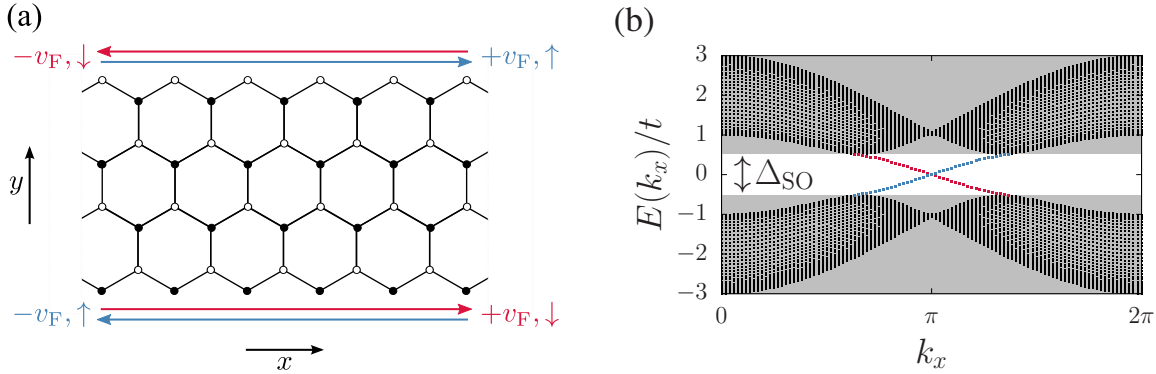


Figure 2.5: (a) Zigzag ribbon with periodic (open) boundary conditions in the x - (y -) direction. (b) Energy spectrum of the Kane-Mele model on a zigzag ribbon. The grey shading indicates bulk states with energy $|E| > \Delta_{SO} = 3\sqrt{3}\lambda$. Only the edge states localised at the top edge are shown. Here, $\lambda = 0.1t$.

the helical edge states from the upper edge that connect the projected Dirac points and have a zero-energy crossing at $k = k_x = \pi$. As for the integer quantum Hall case, the existence of these states may also be inferred from a flux-insertion argument [9, 100]; a Chern-Simons theory for topological insulators has been developed in [101]. Because of their exponential localisation, the edge modes are essentially one-dimensional liquids. In the continuum limit, a single-pair of helical edge states—as realised in the Kane-Mele model—is described by [102, 103]

$$\mathcal{H}_{\text{edge}} = i\hbar v_F \int dx \Psi^\dagger s^z \partial_x \Psi, \quad \Psi^\dagger = (\psi_\uparrow^\dagger, \psi_\downarrow^\dagger), \quad (2.24)$$

where $\psi_\uparrow \equiv \psi_{R\uparrow}$ and $\psi_\downarrow \equiv \psi_{L\downarrow}$ describe right- and left-moving fermions with spin \uparrow and \downarrow , respectively.¹⁷ Although extremely useful for low-energy descriptions, such edge theories are associated with gauge anomalies and can only be consistently defined in two dimensions [104, 105]. For two-dimensional topological insulators, the holographic nature of the edge states also follows from a one-dimensional analogue of the fermion doubling theorem [102].

The above discussion reveals the possibility of topological insulators with a nonzero spin-Hall conductance and edge states, but a comprehensive understanding and the identification of topological insulators as a genuinely new state of matter requires further arguments. The construction of the topological insulator from two independent integer quantum Hall states crucially relies on the conservation of S^z , allowing us to define ν in terms of the Chern numbers C^\uparrow, C^\downarrow . The $U(1)$ spin symmetry of Hamiltonian (2.15) implies a conservation of spin currents and hence a quantised spin-Hall conductivity. While spin conservation allows for a simplified description, it is neither essential nor generic for topological insulators, which are in general described by a full 4×4 Bloch Hamiltonian [9, 92, 106]. A spin-Hall response persists, but $\sigma_{xy}^{\text{spin}}$ is not quantised and spin currents not conserved. Nevertheless, the Z_2 invariant retains its value $\nu = 1$ [9, 98], distinguishing topological and trivial insulators. Without interactions, ν is

¹⁷Because of the locking of momentum and spin we can drop either the L, R or the \uparrow, \downarrow indices.

identical to the parity of the number of pairs of helical edge states [9, 13].¹⁸ This *bulk-boundary correspondence* is a generalisation of the ideas of Halperin [24]. A topological insulator with $\nu = 1$ is hence more than just two copies of the integer quantum Hall state.¹⁹ The Z_2 index can also be determined from the Bloch bands $|u_m(\mathbf{k})\rangle$ [8]. Given inversion symmetry, it suffices to calculate the parity eigenvalues of the states at the time-reversal invariant momenta [106]. Methods to calculate ν for interacting systems will be discussed in chapter 4.

The most important perturbation that violates S^z conservation [reducing the spin symmetry from $U(1)$ to Z_2] is Rashba spin-orbit coupling due to a broken inversion or mirror symmetry $z \rightarrow -z$ [107]. In graphene, it typically arises from the presence of a substrate²⁰ and has the form of a complex nearest-neighbour hopping [8, 9],

$$\hat{H}_R = i\lambda' \sum_{\langle i,j \rangle} \mathbf{c}_i^\dagger \left(\frac{1}{2} \mathbf{s} \times \mathbf{d}_{ij} \right)_z \mathbf{c}_j . \quad (2.25)$$

Rashba coupling is generally difficult to include in numerical simulations and gives rise to a sign problem in quantum Monte Carlo simulations, see chapter 3. The stability of the edge states in the presence of Rashba spin-orbit coupling has been numerically verified [9, 98]. For the Kane-Mele model, the topological phase persists as long as $\lambda' < 2\sqrt{3}\lambda$ [8, 98].

While integer quantum Hall states are stable with respect to any local perturbations (corresponding to class A of the general classification [40, 41]), topological insulators are protected by time-reversal symmetry (class AII). As long as the latter is preserved, local perturbations such as disorder or electron-electron interactions cannot change ν [8, 9, 102, 108]. Exploiting the bulk-boundary correspondence, this stability can also be understood in terms of the helical edge states. Considering a single pair of edge states with dispersion $\epsilon_s(k)$, time-reversal symmetry demands that $\epsilon_\downarrow(-k) = \epsilon_\uparrow(k)$. Because the momenta $\bar{k} = 0, \pi$ are invariant (modulo a reciprocal lattice vector) under time-reversal,

$$\epsilon_\uparrow(\bar{k}) = \epsilon_\downarrow(\bar{k}) , \quad (2.26)$$

a crossing of the edge states at \bar{k} is protected.²¹ While backscattering (the most relevant perturbation in ordinary one-dimensional metals [109]) is completely absent in chiral edge states of integer quantum Hall systems because there are no states with opposite momentum, in helical metals the reason is that the single-particle states $|k, \uparrow\rangle$ and $|-k, \downarrow\rangle$ are Kramers partners and therefore orthogonal [8, 14, 102, 108]. The stability with respect to disorder was numerically verified in [98, 110]. The presence of counter-propagating electrons at a given edge has important implications for strongly interacting systems, as discussed in chapter 5. Regardless of time-reversal symmetry backscattering is not forbidden in systems with an even number of edge state pairs ($\nu = 0$) so that the edge modes can be gapped out [102, 108].

While the above discussion has established that topological insulators are robust with respect to weak perturbations, allowing for their experimental realisation, strong perturbations

¹⁸Because the Haldane model has Chern number $C = \pm 1$, and hence one chiral mode per edge, the Kane-Mele model has one pair of edge states per edge.

¹⁹However, the two states can be connected adiabatically, i.e., without closing the bulk gap [100].

²⁰Inversion symmetry is also broken in the experimentally studied HgTe/CdTe quantum well structures [10].

²¹A topological insulator with one pair of edge states has a crossing at either 0 or π .

2.3. Interaction terms

have the potential of changing the topological invariant and hence the physical properties. Within the Kane-Mele model, the topological phase disappears when the gap is closed by a competing term such as Rashba coupling [98, 110] or a staggered potential [25]. The topological state can also be destroyed if the protecting time-reversal symmetry is broken [39]. Such a symmetry-breaking can be the result of an external magnetic field or, more interestingly, take place spontaneously at interaction-driven phase transitions involving the onset of magnetism. The latter possibility will be explored in detail in chapters 4 and 5.

2.3 Interaction terms

In this section, we define the interaction terms considered in the following chapters.

The Hubbard interaction amounts to a repulsion between electrons of opposite spin occupying the same orbital or site [111]. For the honeycomb lattice models considered here, we write it in the form

$$\hat{H}_U = \frac{U}{2} \sum_i (\hat{n}_i - 1)^2, \quad (2.27)$$

where the density operator is defined as $\hat{n}_i = \mathbf{c}_i^\dagger \mathbf{c}_i = c_{i\uparrow}^\dagger c_{i\uparrow} + c_{i\downarrow}^\dagger c_{i\downarrow}$. We also define the electron spin operator $\hat{S}_i = \frac{1}{2} \sum_{ss'} c_{is}^\dagger \mathbf{s}_{ss'} c_{is'}$. The Kane-Mele model with the Hubbard term (2.27) is referred to as the *Kane-Mele-Hubbard model* and was first considered in [82].

In the absence of efficient screening, for example due to the vanishing density of states at the Fermi level in graphene [112, 113], a more realistic interaction is

$$\hat{H}_V = \frac{1}{4} \sum_{ij} V_{ij} (\hat{n}_i - 1) (\hat{n}_j - 1), \quad (2.28)$$

where the matrix elements are given by²²

$$V_{ij} = \begin{cases} 2U, & \text{if } |\mathbf{r}_i - \mathbf{r}_j| = 0 \\ \frac{\alpha U \delta}{|\mathbf{r}_i - \mathbf{r}_j|}, & \text{if } |\mathbf{r}_i - \mathbf{r}_j| > 0 \end{cases}. \quad (2.29)$$

To facilitate a comparison with results for the Hubbard repulsion (2.27), the interaction is defined such that both the local and the nonlocal part scale with the Hubbard parameter U . Their relative strength is determined by α , with $\alpha = 0$ corresponding to the local Hubbard interaction (2.27). The physical Coulomb interaction has the familiar form $V(r) = e^2/\epsilon_0 r$. Interestingly, the small value of the charge velocity $v_F \approx c/300$ in graphene significantly enhances the ratio of potential and kinetic energy compared to standard QED [113]. Moreover, $v_F \ll c$ implies that the interaction is essentially instantaneous [113]. The Kane-Mele model with the interaction term (2.28) will be referred to as the *Kane-Mele-Coulomb model* [A7].

²² Here, $\delta = \frac{2}{3}|\mathbf{a}_2 - \frac{1}{2}\mathbf{a}_1|$ is the distance between the two sites in the unit cell, see figure 2.1(a). $\delta = a = 1$ in the convention used in this chapter, but $\delta = 1/\sqrt{3}$ for example in chapter 4.

Finally, we will discuss extended Hubbard models with interactions of the form

$$\hat{H}_{UV_1V_2} = U \sum_i \hat{n}_{i\uparrow} \hat{n}_{i\downarrow} + V_1 \sum_{\langle i,j \rangle} \hat{n}_i \hat{n}_j + V_2 \sum_{\langle\langle i,j \rangle\rangle} \hat{n}_i \hat{n}_j \quad (2.30)$$

for spinful fermions and

$$\hat{H}_{V_1V_2} = V_1 \sum_{\langle i,j \rangle} \hat{n}_i \hat{n}_j + V_2 \sum_{\langle\langle i,j \rangle\rangle} \hat{n}_i \hat{n}_j \quad (2.31)$$

for spinless fermions on the honeycomb lattice. Here, V_1 is a repulsion between fermions on nearest-neighbour sites connected by the vectors $\pm\boldsymbol{\delta}_i$ in figure 2.2(a), while V_2 is a repulsion between next-nearest-neighbour sites connected by the vectors $\pm\boldsymbol{a}_i$ in figure 2.3(a). In contrast to the monotonically decaying Coulomb interaction (2.28) discussed in chapter 4, we will consider interactions $V_2 > V_1$ in chapter 6.

All results shown in the following chapters were obtained for half-filled bands, corresponding to two electrons per unit cell for spinful models, and one fermion per unit cell for spinless models. Given particle-hole symmetry, the chemical potential for half-filling is zero. For the simulations, honeycomb lattices with $L \times L'$ unit cells and $N = 2LL'$ lattice sites were used. The units were chosen such that $e = \hbar = k_B = 1$.

3 Quantum Monte Carlo methods

The majority of research underlying this thesis was carried out with the help of quantum Monte Carlo methods. The present chapter begins with an introduction to Monte Carlo methods in general, followed by brief expositions of the auxiliary-field method and the continuous-time interaction-expansion (*CT-INT*) method. Further details regarding the implementation and the applications discussed in later chapters can be found in the appendix, as well as in the references provided below. General introductions to Monte Carlo methods can be found in, e.g., [114, 115], whereas methods for correlated fermions are reviewed in, e.g., [116–120].

The use of Monte Carlo methods can be motivated by considering integrals of the form

$$\langle A \rangle = \int d^N \mathbf{x} A(\mathbf{x}) p(\mathbf{x}), \quad (3.1)$$

where $p(\mathbf{x})$ is positive definite and normalised to unity, $\int d^N \mathbf{x} p(\mathbf{x}) = 1$, and can therefore be interpreted as a probability density. Equation (3.1) has the typical form of an expectation value of a quantity A . If the dimension N is large, standard integration methods such as Simpson’s rule are insufficient because for a given precision the number of mesh points increases exponentially with N [115]. However, given R independent random samples \mathbf{x}_r from the distribution $p(\mathbf{x})$ and corresponding values $A(\mathbf{x}_r)$, a stochastic estimate is

$$\bar{A} = \frac{1}{R} \sum_{r=1}^R A(\mathbf{x}_r). \quad (3.2)$$

According to the central limit theorem, for any probability distribution $p(\mathbf{x})$, this average becomes normally distributed around the true value $\langle A \rangle$ for large R : $\bar{A} = \langle A \rangle \pm \Delta \bar{A}$. The statistical error is $\Delta \bar{A} = \sigma_A / \sqrt{R}$ where σ_A is the intrinsic variance of A with respect to $p(\mathbf{x})$, $\sigma_A^2 = \langle A^2 \rangle - \langle A \rangle^2$. Importantly, $\Delta \bar{A}$ can be reduced by increasing the number of measurements R , and the convergence with R does not explicitly depend on the dimension N . While σ_A is usually not known, it can be estimated from

$$\sigma_A^2 = \frac{1}{R-1} \sum_{r=1}^R [A(\mathbf{x}_r) - \bar{A}]^2. \quad (3.3)$$

The sampling of the integral (3.1) by drawing points \mathbf{x}_r from a distribution $q = p$ rather than from the uniform distribution $q = 1$ is an example of *importance sampling*. The variance σ_A^2 can be reduced by optimising the distribution q for a given integrand to avoid configurations that make negligible contributions; σ_A^2 is minimal (zero) for the academic choice $q = Ap / \langle A \rangle$ [115].

High-dimensional integrals or sums of the form (3.1) arise naturally when considering the thermodynamic expectation value of an observable A . For example, for the classical Ising model, the sum is over spin configurations \mathbf{s} with a spin $s_i = \pm 1$ on each of the N lattice sites,

$$\langle A \rangle = \frac{1}{Z} \sum_{\mathbf{s}} A(\mathbf{s}) e^{-\beta E(\mathbf{s})}, \quad Z = \sum_{\mathbf{s}} e^{-\beta E(\mathbf{s})}. \quad (3.4)$$

Here, $\beta = (k_B T)^{-1}$ is the inverse temperature, E the energy, and Z the partition function. More generally, $Z = \sum_C W(C)$ and expectation values take the form

$$\langle A \rangle = \sum_C \langle \langle A(C) \rangle \rangle_C W(C), \quad (3.5)$$

with the configuration weight $W(C) = e^{-\beta E(C)}/Z$ for the Ising model. By sampling configurations according to their Boltzmann weight [121], Monte Carlo methods avoid regions of phase space that make exponentially small contributions to expectation values. This is a crucial aspect given the fact that even for classical systems the phase space grows exponentially with system size. For the Ising model, the number of possible configurations is 2^N .

For quantum systems, the starting point is the partition function $Z = \text{Tr} e^{-\beta \hat{H}}$, which can be mapped to a classical problem with an additional dimension of length β corresponding to imaginary time via Feynman's path-integral and Wick's rotation [122, 123]. Different representations of the trace result in different quantum Monte Carlo methods. For example, writing the trace as a sum over Fock states leads to world-line methods [124].¹ While a functional integral representation in terms of Grassmann variables cannot be directly sampled, efficient and versatile Monte Carlo algorithms for fermionic systems have been developed by expressing Z as a sum over auxiliary-field configurations [126] (section 3.1) or over configurations of interaction vertices [127] (section 3.2).

For many years, it was commonly believed that a discretisation of imaginary time (the Suzuki-Trotter decomposition [128, 129], see below) is essential for quantum Monte Carlo simulations. This limitation was first overcome for bosons and spins [130–133], while continuous-time algorithms for fermions have appeared more recently [127, 134–138]. Although continuous-time methods have become the standard for the solution of impurity and cluster problems in the context of quantum cluster theories [136, 139], a general method for lattice problems with the same linear scaling with inverse temperature as the auxiliary-field method is not yet available.

In contrast to the discussion of Monte Carlo integration of equation (3.1), it is usually not possible to directly sample W in equation (3.5). Instead, starting from a random initial configuration, new configurations are generated in such a way as to obtain a Markov chain whose equilibrium (reached after a warmup phase) is W [121]. A sufficient condition for the Markov property [the probability $P(C_n \rightarrow C_m)$ to move to a new configuration C_m only depends on the current configuration C_n] is *detailed balance*, $W(C_n)P(C_n \rightarrow C_m) = W(C_m)P(C_m \rightarrow C_n)$ [115].

¹While world-line methods [117, 118, 120, 125] are extremely useful for bosons and spins, they suffer from a severe minus-sign problem for fermions in more than one dimension due to Fermi statistics.

The latter is fulfilled by the Metropolis-Hastings algorithm [121, 140], according to which the Monte Carlo move from C_n to C_m is accepted with probability [140]

$$P(C_n \rightarrow C_m) = \min \left[1, \frac{T(C_n \rightarrow C_m) W(C_m)}{T(C_m \rightarrow C_n) W(C_n)} \right]. \quad (3.6)$$

If the proposals are symmetric, $T(C_n \rightarrow C_m) = T(C_m \rightarrow C_n)$, a more likely configuration is always accepted, whereas a less likely configuration is accepted with probability $W(C_m)/W(C_n)$. In contrast to the exact sampling leading to equation (3.3), consecutive configurations in a Markov chain are usually not statistically independent. The autocorrelations have to be taken into account when calculating error bars of observables, and can be reduced by performing more updates between measurements or using suitable nonlocal updates.

Especially for fermionic systems, the configuration weight $W(C)$ is not necessarily positive [141]. This so-called *sign problem* can be formally overcome by sampling configurations according to $|W|$, and treating the sign of W as part of the observables: $\langle A \rangle_W = \langle A \text{ sign} \rangle_{|W|} / \langle \text{sign} \rangle_{|W|}$. However, this reweighting is only useful for sufficiently large values of $\langle \text{sign} \rangle$. If there is a sign problem for a given combination of model and method, the average sign typically depends exponentially on system size and inverse temperature [142], leading to an exponentially increasing computational effort to reach a given accuracy. While a general solution of the sign problem has been shown to be NP-hard [143], there are a number of interesting models for which the weights are positive as a result of symmetries. In the absence of a sign problem, quantum Monte Carlo simulations scale polynomially with system volume and inverse temperature and can be used to carry out unbiased studies on large lattices. For systems of bosons or nonfrustrated spins, algorithms that scale $\sim \beta N$ can be used to obtain results of essentially arbitrary accuracy even in higher dimensions [120]. On the other hand, fermionic problems remain challenging despite advances in algorithms and hardware. A discussion of recent developments and a comparison of different algorithms for fermions can be found in [138].

3.1 Auxiliary-field method

Despite the above-mentioned recent progress in continuous-time Monte Carlo methods for fermions, discrete-time auxiliary-field methods continue to play a central role for the investigation of correlated fermions due to their versatility and βN^3 scaling of computer time. In contrast to world-line methods, and given certain symmetries of the Hamiltonian, it is possible to show that the configuration weights are strictly positive. This is in particular the case for the Kane-Mele-Hubbard and Kane-Mele-Coulomb models discussed in chapter 4. Auxiliary-field methods can also be used to investigate, e.g., Kondo lattice models [144] or electron-phonon models [145], and allow the calculation of entanglement properties [146]. The method described below goes back to the work of Blankenbecler, Scalapino, and Sugar [126] and is also known as the *BSS method*. The following discussion partly follows [118], and the reader may also find the exposition in [147] and [148] very useful.

The key idea is to express the grand-canonical partition function of an interacting problem

3.1. Auxiliary-field method

in terms of a noninteracting fermions coupled to auxiliary fields,

$$Z = \text{Tr} e^{-\beta(\hat{H}-\mu\hat{N})} = \int \mathcal{D}[\phi] e^{-S[\phi]}. \quad (3.7)$$

Within the functional integral formalism, the Hubbard-Stratonovich decoupling of a fermion-fermion interaction $S_{\text{int}} = \sum_{ij} \rho_i V_{ij} \rho_j$ with Grassmann bilinears $\rho_i = \sum_s \bar{\psi}_{is} \psi_{is}$ takes the general form [149]

$$e^{-\sum_{ij} \rho_i V_{ij} \rho_j} = \int \mathcal{D}[\phi] e^{-\frac{1}{4} \sum_{ij} \phi_i V_{ij}^{-1} \phi_j - i \sum_i \phi_i \rho_i}. \quad (3.8)$$

The decoupling makes the action quadratic in the fermionic fields so that the latter can be integrated out. The resulting problem takes the form of free electrons moving in a space- and time-dependent potential defined by the auxiliary fields. The integral over field configurations can be carried out by Monte Carlo methods. In particular, the Gaussian form of the theory for a fixed field configuration allow expressing arbitrary observables in terms of the single-particle Green function [150].

The BSS method is formulated in discrete imaginary time [126]. Similar to the derivation of the functional integral [115], a Suzuki-Trotter decomposition [128, 129] is used to separate the contributions from the single-particle part \hat{H}_t [e.g., equation (2.5)] and the interaction part \hat{H}_U [e.g., equation (2.27)] of the Hamiltonian. Thereby, the partition function becomes

$$Z \approx \text{Tr} \left[(e^{-\Delta\tau\hat{H}_U} e^{-\Delta\tau\hat{H}_t})^M \right], \quad (3.9)$$

with leading corrections of $\mathcal{O}(\Delta\tau^2)$ and $\Delta\tau = \beta/M$. The Hubbard-Stratonovich transformation used to decouple the interaction is not unique, and the choice depends on the application. For the present discussion, we consider [151]

$$e^{-\Delta\tau U \sum_i (\hat{n}_i - 1)^2} = \gamma^N \sum_{\phi_1, \dots, \phi_N} e^{\alpha \sum_i \phi_i (\hat{n}_{i\uparrow} - \hat{n}_{i\downarrow})}, \quad (3.10)$$

where $\gamma = \frac{1}{2}e^{-\Delta\tau U/2}$, and $\cosh \alpha = e^{\Delta\tau U/2}$. Carrying out this decoupling on each time slice leads to NM Ising fields $\phi_{i,m} = \pm 1$. The exact transformation (3.10) couples the Ising fields to the magnetisation, so that the SU(2) spin symmetry is broken for each configuration and only restored after averaging. Therefore, a different transformation with discrete fields $\phi_{i,m} \in \{-2, -1, 1, 2\}$ and overall error $\mathcal{O}(\Delta\tau^3)$ [152] was used for the Kane-Mele-Hubbard model in chapter 4, see [A3]. While a rather similar algorithm with discrete fields can be derived for nonlocal interactions [153], the simulations of the Kane-Mele-Coulomb model were based on equation (3.8) and Monte Carlo sampling of continuous gauge fields defined in discrete space-time [A7]. Similar methods were previously applied to graphene and in lattice QED [154–156].

Following [118], we write $\hat{H}_t - \mu\hat{N} = \sum_{xy} c_x^\dagger T_{xy} c_y$ with the single-particle matrix T ,² and $\alpha \sum_i \phi_i (\hat{n}_{i\uparrow} - \hat{n}_{i\downarrow}) = \sum_{xy} c_x^\dagger [V_\phi]_{xy} c_y$ with the interaction matrix V_ϕ that depends on the auxiliary-

²Here, x and y correspond to combinations of a lattice site and a spin direction, e.g., $x = (i, s)$, $y = (j, s')$.

field configuration $\phi = \{\phi_{i,m}\}$. Neglecting terms of order $\Delta\tau^2$ and higher we have [126]

$$Z \approx \Gamma \sum_{\phi} \text{Tr} \left[\prod_{m=1}^M e^{\sum_{xy} c_x^\dagger [V_\phi]_{xy} c_y} e^{-\Delta\tau \sum_{xy} c_x^\dagger T_{xy} c_y} \right] = \Gamma \sum_{\phi} \det [1 + B_\phi(\beta, 0)] , \quad (3.11)$$

with $\Gamma = \gamma^{NM}$ and the imaginary-time propagator

$$B_\phi(\tau_2, \tau_1) = B_\phi(m_2\Delta\tau, m_1\Delta\tau) = \prod_{m=m_1+1}^{m_2} e^{V_\phi} e^{-\Delta\tau T} . \quad (3.12)$$

To obtain the form (3.5), $\langle A \rangle = \text{Tr} [\hat{A} e^{-\beta H}] / Z \approx \sum_{\phi} \langle \langle A \rangle \rangle_{\phi} W(\phi)$ with an error $O(\Delta\tau^2)$ [157], we define the configuration weight

$$W(\phi) = \frac{\det[1 + B_\phi(\beta, 0)]}{\sum_{\phi} \det[1 + B_\phi(\beta, 0)]} . \quad (3.13)$$

For each configuration, Wick's theorem can be used to express $\langle \langle A \rangle \rangle_{\phi}$ in terms of the single-particle Green function, which is given by

$$[G_\phi(\tau)]_{xy} = \langle \langle c_x(\tau) c_y^\dagger(\tau) \rangle \rangle_{\phi} = [1 + B_\phi(\tau, 0) B_\phi(\beta, \tau)]_{xy}^{-1} . \quad (3.14)$$

The latter plays a central role in the algorithm because it also determines the ratio of configuration weights, see below. Similarly, dynamic correlation functions can be calculated by averaging Wick decompositions in terms of the time-displaced Green function matrix $G_\phi(\tau_1, \tau_2)$. For spin-1/2 models, the matrices in equation (3.14) have dimension $2N \times 2N$. If spin is conserved, the weight can be factorised into $s = \uparrow, \downarrow$ components, $W = W^\uparrow W^\downarrow$, where W^s has the form of equation (3.13) with $N \times N$ matrices B_ϕ^s [126, 147].

The Monte Carlo sampling is done in terms of a Markov chain. In each step, a single Ising field $\phi_{i,m}$ from the current configuration ϕ is selected and proposed to be updated, leading to a new configuration ϕ' . To decide upon the acceptance of this update according to equation (3.6), the ratio $W(\phi')/W(\phi)$ is calculated. After a sufficient number of updates to obtain a statistically independent configuration, observables can be measured. In practice, two key problems have to be overcome for a useful algorithm. First, to achieve the aforementioned scaling of computer time $\sim \beta N^3$, the local nature of the updates has to be exploited [126].³ Second, a

³Changing a single field $\phi_{i,m}$ implies that only one element of the matrix V_ϕ in equation (3.12) is affected. Accordingly, $B_\phi^s(\beta, 0) = B_\phi^s(\beta, m\Delta\tau)(1 + \Delta^s)B_\phi^s(m\Delta\tau, 0)$ with $\Delta_{jk}^s = \delta_{ji}\delta_{ki}(e^{-2s\alpha\phi_{i,m}} - 1)$ [147]. The ratio of weights is given by $W^s(\phi')/W^s(\phi) = 1 + \{1 - [G_\phi^s(\tau)]_{ii}\}\Delta_{ii}^s$. If the update is accepted, the Green functions $G_\phi^s(\tau)$ can be updated efficiently using the Sherman-Morrison formula [158]

$$(M^{-1} + \mathbf{u}\mathbf{v}^T)^{-1} = M^{-1} - \frac{M^{-1}\mathbf{u}\mathbf{v}^T M^{-1}}{1 + \mathbf{v}^T M^{-1}\mathbf{u}} . \quad (3.15)$$

The sweeps are done sequentially: starting on the first time slice, updates are proposed at all lattice sites before proceeding to the next time slice. Thereby, information stored from previous updates can be re-used [118]. The Green function update on a given time slice requires $O(N^2)$ operations, so sweeping through all NM fields gives the aforementioned $N^3 M$ (or $N^3\beta$) scaling [147]. For more details see [118, 147].

3.1. Auxiliary-field method

direct calculation of the Green function according to equation (3.14) is numerically unstable at low temperatures and requires stabilisation [118, 147, 159–161]. Similar issues arise in the calculation of the time-displaced Green function [118, 162]. The auxiliary-field method produces results with statistical errors (controlled by the number of measurements) and a Trotter discretisation error (controlled by the number of time slices); the latter is a high-energy error that can often be neglected compared to statistical errors, or be removed by extrapolating observables to the limit $\Delta\tau \rightarrow 0$.

While we have only discussed the grand-canonical case so far, the method can also be formulated in a projective, canonical variant to obtain ground-state results [147, 161, 163]. The starting point is the following expression for the ground-state expectation value of \hat{A} ,

$$\langle A \rangle^{(\theta)} = \frac{\langle \Psi_0 | \hat{A} | \Psi_0 \rangle}{\langle \Psi_0 | \Psi_0 \rangle} = \lim_{\theta \rightarrow \infty} \frac{\langle \Psi_T | e^{-\theta \hat{H}} \hat{A} e^{-\theta \hat{H}} | \Psi_T \rangle}{\langle \Psi_T | e^{-2\theta \hat{H}} | \Psi_T \rangle}. \quad (3.16)$$

Here, $|\Psi_0\rangle$ is the ground state of \hat{H} , $|\Psi_T\rangle$ is a trial wavefunction (a Slater determinant) with nonzero overlap $\langle \Psi_T | \Psi_0 \rangle$, and θ is a projection parameter. The projective formulation has many analogies with the finite-temperature algorithm [118, 147]. The sampling is again in terms of local Ising field updates. Fast updates can be implemented, and the numerical stability of the matrices is less critical than for the finite-temperature algorithm. The projective formulation is advantageous to study ground-state properties and has been used for the majority of results in chapter 4. For a detailed discussion and comparison to the finite-temperature method see [118].

The auxiliary-field method is free of a sign problem in a number of nontrivial cases. These include the attractive Hubbard model at any filling, and the repulsive Hubbard model on bipartite lattices at half-filling [164]. In both cases, the proof of the absence of a sign problem is based on a factorisation of the weight (3.13), $W(\boldsymbol{\phi}) = W_\uparrow(\boldsymbol{\phi})W_\downarrow(\boldsymbol{\phi})$. For the attractive Hubbard model, $W_\uparrow(\boldsymbol{\phi}) = W_\downarrow(\boldsymbol{\phi})$ and real,⁴ so that $W(\boldsymbol{\phi}) > 0$ for all configurations $\boldsymbol{\phi}$. For the repulsive Hubbard model, $W(\boldsymbol{\phi}) > 0$ can be demonstrated by a particle-hole transformation $c_{is}^\dagger \mapsto (-1)^i c_{is}$ in one spin sector with $(-1)^i = \pm 1$ depending on the sublattice [164].⁵ For the Kane-Mele models considered in chapter 4, the positivity of $W(\boldsymbol{\phi})$ at half-filling follows from $W_\uparrow(\boldsymbol{\phi}) = W_\downarrow^*(\boldsymbol{\phi})$ (complex conjugation) due to particle-hole and time-reversal symmetry [A1, A3, 166]. A nonzero Rashba term, equation (2.25), does no longer permit a factorisation into spin components and breaks particle-hole symmetry, which leads to a sign problem. Models of spinless fermions exhibit a sign problem in the above BSS formulation because there is only one determinant, but can be expressed in terms of two species of Majorana fermions to obtain positive weights [167]. The absence of a sign problem can also be shown in cases where the weights do not factorise but the determinant is a product over eigenvalues that occur in complex-conjugate pairs as a result of an anti-unitary symmetry such as time-reversal or particle-hole symmetry [70].

⁴The Hubbard-Stratonovich transformation in this case can be chosen to couple to the density $\hat{n}_{i\uparrow} + \hat{n}_{i\downarrow}$ [151].

⁵The transformation provides an exact mapping between the attractive and repulsive models at half-filling [165].

3.2 CT-INT method

The CT-INT method is part of a group of continuous-time Monte Carlo methods for fermions that have been widely adopted as impurity solvers for quantum cluster methods such as dynamical mean-field theory [168]. These methods are versatile because they can be formulated directly in terms of an action, which makes it possible to treat bath degrees of freedom, phonons, or effective models obtained by integrating out high-energy bands. The CT-INT method in the form used here goes back to the work of Rubtsov *et al.* [127]; similar ideas were presented earlier by Rombouts [134]. Other variants such as CT-HYB [135] and CT-AUX [136] were introduced later. As pointed out in [169], there is an exact relation between the continuous-time methods of [127, 134] and the discrete-time Hirsch-Fye method [170]. While for lattice problems CT-INT is formally more expensive than the auxiliary-field method [126] and its recently developed continuous-time variant [137, 138], it is more versatile and in fact competitive for problems with bath degrees of freedom (see chapter 5) or coupled fermion-boson models (see, e.g., [171]). A review of CT-INT with a focus on impurity solvers has been given in [119].

With the application to helical edge states in chapter 5 in mind, we focus on the functional-integral formulation. The Hubbard model is described by the action

$$S = S_0 + S_U = \int_0^\beta d\tau \sum_{ijs} \bar{\psi}_{is}(\tau) [\delta_{ij}\partial_\tau + t_{ij}] \psi_{js}(\tau) + U \int_0^\beta d\tau \sum_i \rho_{i\uparrow}(\tau)\rho_{i\downarrow}(\tau). \quad (3.17)$$

The CT-INT method relies on a weak-coupling expansion of the partition function,

$$\frac{Z}{Z_0} = \langle e^{-S_U} \rangle_0 = \sum_{n=0}^{\infty} \frac{(-1)^n}{n!} U^n \int_0^\beta d\tau_1 \sum_{i_1} \cdots \int_0^\beta d\tau_n \sum_{i_n} \langle \rho_{i_1\uparrow}(\tau_1)\rho_{i_1\downarrow}(\tau_1) \cdots \rho_{i_n\uparrow}(\tau_n)\rho_{i_n\downarrow}(\tau_n) \rangle_0, \quad (3.18)$$

which we write as

$$\frac{Z}{Z_0} = \sum_{n=0}^{\infty} \sum_{\chi_1} \cdots \sum_{\chi_n} \frac{(-1)^n}{n!} w(\chi_1) \cdots w(\chi_n) \langle h(\chi_1) \cdots h(\chi_n) \rangle_0. \quad (3.19)$$

To avoid a trivial sign problem, the interaction is redefined as [172]

$$S_U = \frac{U}{2} \int_0^\beta d\tau \sum_i \sum_{\phi=\pm 1} [\rho_{i\uparrow}(\tau) - \alpha_\uparrow(\phi)][\rho_{i\downarrow}(\tau) - \alpha_\downarrow(\phi)], \quad (3.20)$$

with an Ising field ϕ , and $\alpha_s(\phi) = \frac{1}{2} + s\phi\delta$ with $\delta > 1/2$ at half-filling [172]. Returning to equation (3.19), vertex l is described by variables $\chi_l = \{i_l, \tau_l, \phi_l\}$, weight $w(\chi_l) = U/2$, and $h(\chi_l) = [\rho_{i_l\uparrow}(\tau_l) - \alpha_\uparrow(\phi_l)][\rho_{i_l\downarrow}(\tau_l) - \alpha_\downarrow(\phi_l)]$.

For a finite volume and at finite temperature, the perturbation expansion converges and can be sampled stochastically [127]. Because permutations of the vertices do not change the weight, we can introduce unnumbered vertex configurations C_n [127]. The factor $n!$ from the permutations then cancels the factor $1/n!$ in equation (3.19) and we find

$$\frac{Z}{Z_0} = \sum_{n=0}^{\infty} \sum_{C_n} W(C_n), \quad W(C_n) = (-1)^n w(\chi_1) \cdots w(\chi_n) \det M(C_n), \quad (3.21)$$

3.2. CT-INT method

where we have used Wick's theorem to evaluate the expectation value with respect to S_0 . Since each vertex contributes two fermion bilinears, the matrix $M(C_n)$ has dimension $2n \times 2n$. Similar to the auxiliary-field method, conservation of spin implies that the determinant can be factorised as $\det M(C_n) = \det M^\uparrow(C_n) \det M^\downarrow(C_n)$. The $n \times n$ matrices $M^s(C_n)$ contain the non-interacting Green functions $g_{ij}^s(\tau, \tau') = \langle c_{is}^\dagger(\tau) c_{js}(\tau') \rangle_0$,

$$M^s(C_n) = \begin{pmatrix} g_{i_1 i_1}^s(\tau_1, \tau_1) - \alpha_s(\phi_1) & g_{i_1 i_2}^s(\tau_1, \tau_2) & \cdots & g_{i_1 i_n}^s(\tau_1, \tau_n) \\ g_{i_2 i_1}^s(\tau_2, \tau_1) & g_{i_2 i_2}^s(\tau_2, \tau_2) - \alpha_s(\phi_2) & \cdots & g_{i_2 i_n}^s(\tau_2, \tau_n) \\ \vdots & \vdots & \ddots & \vdots \\ g_{i_n i_1}^s(\tau_n, \tau_1) & g_{i_n i_2}^s(\tau_n, \tau_2) & \cdots & g_{i_n i_n}^s(\tau_n, \tau_n) - \alpha_s(\phi_n) \end{pmatrix}. \quad (3.22)$$

The determinant $\det M(C_n)$ amounts to the summation over all possible Feynman diagrams for a given configuration of vertices C_n .

Expectation values $\langle A \rangle = \langle e^{-S_U} A \rangle_0 / \langle e^{-S_U} \rangle_0$ take the form

$$\langle A \rangle = \frac{\sum_{n=0}^{\infty} \sum_{C_n} \langle \langle A \rangle \rangle_{C_n} W(C_n)}{\sum_{n=0}^{\infty} \sum_{C_n} W(C_n)}, \quad \langle \langle A \rangle \rangle_{C_n} = \frac{\langle h(\chi_1) \cdots h(\chi_n) A \rangle_0}{\det M(C_n)}. \quad (3.23)$$

For a given vertex configuration, $\langle h(\chi_1) \cdots h(\chi_n) A \rangle_0$ can again be decomposed using Wick's theorem [173], with the required single-particle Green function given by

$$\langle \langle c_{is}^\dagger(\tau) c_{js}(\tau') \rangle \rangle_{C_n} = \frac{\det \tilde{M}(C_n)}{\det M(C_n)}, \quad \tilde{M}(C_n) = \begin{pmatrix} & g_{i_1 j}^s(\tau_1, \tau') \\ M(C_n) & \vdots \\ g_{i_1 i_1}^s(\tau, \tau_1) & \cdots & g_{ij}^s(\tau, \tau') \end{pmatrix} \quad (3.24)$$

where the matrix $\tilde{M}(C_n)$ contains one additional row and column compared to $M(C_n)$.

To sample the expansion order and vertex variables in equation (3.21) it is sufficient to add or remove a single vertex at a time using equation (3.6). For example, for the addition of a Hubbard vertex with random position, time, and Ising field we have $T(C_n \rightarrow C_{n+1}) = \frac{1}{N} \frac{1}{\beta} \frac{1}{2}$, whereas $T(C_{n+1} \rightarrow C_n) = \frac{1}{n+1}$. The Metropolis-Hastings probability is [see also equation (3.21)]

$$P(C_n \rightarrow C_{n+1}) = \min \left[1, -\frac{UN\beta}{n+1} \prod_s \frac{\det M^s(C_{n+1})}{\det M^s(C_n)} \right]. \quad (3.25)$$

Additionally, it is useful to also update the fields ϕ_l while keeping the number of vertices constant. Simulations can be started with the trivial configuration of expansion order $n = 0$, and a warm-up is carried out until the average expansion order has stabilised.

Similar to the auxiliary-field method, an efficient algorithm can be obtained by using fast updates that exploit the fact that the matrices $M^s(C_{n\pm 1})$ and $M^s(C_n)$ entering the update probabilities only differ by one row and column.⁶ For the CT-INT method, computer time scales

⁶The ratios of determinants in equations (3.24) and (3.25) can be efficiently calculated using

$$\det \begin{pmatrix} M & \mathbf{u} \\ \mathbf{v}^T & z \end{pmatrix} = \det M \det [z - \mathbf{v}^T M^{-1} \mathbf{u}]. \quad (3.26)$$

as $(\beta N)^3$, with a prefactor that depends on the interaction strength.⁷ In almost all cases, the matrices involved in the CT-INT algorithm are sufficiently well conditioned to not require numerical stabilisation. Finally, a projective variant of CT-INT has been introduced in [172].

As for the BSS method, and given the required symmetries, the absence of a sign problem in the CT-INT method can be shown by factorising the weight. Accordingly, a sign problem is absent for the attractive Hubbard model, the repulsive Hubbard model on bipartite lattices at half-filling, and also the Kane-Mele-Hubbard model. The sign problem caused by the Rashba coupling considered in chapter 5 remains sufficiently weak in order to carry out useful simulations of correlated edge states. Recently, it has been shown that the CT-INT method can also be applied to spinless models without a sign problem [174, 175].

The inverse M^{-1} hence plays a key role, and can be updated using the Sherman-Morrison formula (3.15). To calculate observables, the Green function for the current configuration is calculated from [127]

$$\langle\langle c_{is}^\dagger(\tau) c_{js}(\tau') \rangle\rangle_{C_n} = g_{ij}^s(\tau, \tau') - \sum_{r,s=1}^n g_{ii_r}^s(\tau, \tau_r) [M^s(C_n)]_{rs}^{-1} g_{i_s j}^s(\tau_s, \tau'). \quad (3.27)$$

A similar equation gives the Matsubara Green function required for quantum cluster methods [119].

⁷The dimension of M^{-1} is determined by the expansion order n . For the Hubbard model, $\langle n \rangle \sim \beta LU$ [172]. Fast updates require n^2 operations per vertex, or $n^3 \sim (\beta LU)^3$ operations per sweep.

4 Bulk correlation effects

In this chapter, we review the quantum Monte Carlo results of [A1, A3, A4, A7] on the bulk properties of the Kane-Mele model (2.13) with electron-electron interaction. For $\lambda = 0$, the Kane-Mele model reduces to the tight-binding model (2.5)—which captures the physics of graphene or massless Dirac fermions in 2+1 dimensions—whereas for $\lambda \neq 0$ it describes two-dimensional topological insulators. Here, we will discuss the fate of these phases in the presence of electronic correlations, focussing on systems with periodic boundaries; interaction effects on the edge states will be the topic of chapter 5. The auxiliary-field quantum Monte Carlo method discussed in chapter 3 permits to study either the Hubbard interaction (2.27) or the Coulomb interaction (2.28). For example, the latter gives rise to a logarithmic divergence of the Fermi velocity near E_F in graphene [112, 176, 177]. Because we found very similar physics for the Hubbard and Coulomb interactions, we will discuss them in parallel. We first consider the overall structure of the phase diagram, before addressing the quantum phase transitions and the measurement of the Z_2 topological invariant. Of particular interest will be the universality of the observed phase transitions between the Dirac semimetal or the topological insulator and an antiferromagnet. We will also discuss the possibility of stabilising a charge-density-wave or QSH* phase [57] via a long-range Coulomb interaction that suppresses magnetism [A4]. To avoid the sign problem, the results of this chapter were obtained by neglecting the Rashba term (2.25).

Band theory predicts half-filled systems with one electron per lattice site to be metallic. For the graphene model of chapter 2, the chemical potential is located at zero energy, and the ground state in the absence of interactions is a Dirac semimetal. The fate of metallic states upon adding interactions depends on the details of the band structure. On the square lattice, the nesting of the Fermi surface causes a logarithmic divergence of the spin susceptibility which gives rise to an antiferromagnetic insulating state for any Hubbard repulsion $U > 0$ [178]. In contrast, the semimetal with its isolated Fermi points is stable at weak coupling, which can be seen both from mean-field theory [179] and the renormalisation group flow [180]. Interaction-driven (semi)metal-insulator transitions are referred to as *Mott transitions* [42, 181]. Although a Mott transition does in principle not involve symmetry-breaking, the two phenomena often occur together both in theory and experiment [43].

Field theory makes detailed predictions concerning the possible instabilities and the associated quantum phase transitions [79, 81, 180]. An onsite Hubbard interaction favours a transition to a spin-density-wave state with Heisenberg order parameter $\phi = \langle \bar{\Psi} \mathbf{s} \Psi \rangle$ that breaks the $SU(2)$ spin symmetry, whereas nonlocal interactions favour a charge-density-wave state with Ising order parameter $\chi = \langle \bar{\Psi} \Psi \rangle$ that breaks the sublattice symmetry. Either of these order parameters breaks the chiral symmetry and opens a gap in the Dirac spectrum [80, 180]; their interplay has been studied in [80, 182–186]. According to the Mermin-Wagner theorem [187], continuous symmetries (in particular the spin symmetry of the Kane-Mele model without Rashba coupling)

4.1. Phase diagram

can be spontaneously broken in 2+1 dimensions only at $T = 0$, while discrete order parameters can be nonzero even at $T > 0$.¹ Remarkably, field theory predicts [79, 180] the above transitions to fall outside the Ginzburg-Landau-Wilson paradigm [188],² and instead to have the same universality as Gross-Neveu models [189]. Because the corresponding Gross-Neveu-Yukawa theory has an upper critical spatial dimension of three, the ϵ -expansion [190] can be used to calculate the critical exponents for the case of 2 + 1 dimensions relevant for graphene [79]. At the mean-field level, extended interactions also give rise to complex bond order parameters, with the corresponding ground states being quantum anomalous Hall or quantum spin Hall insulators [44]. Such topological Mott insulators will be discussed in chapter 6. As reviewed below, in addition to the functional renormalisation group calculations [80, 182, 185, 186, 191], the semimetal-insulator transition as a result of strong Hubbard or Coulomb interaction has been studied in particular by quantum Monte Carlo simulations [A7, 153, 155, 179, 192–196]. A review of correlation effects in graphene can be found in [113].

The impact of a Hubbard interaction on the topological phase of the Kane-Mele model was first studied using mean-field theory [82], followed by exact quantum Monte Carlo simulations [A1, A3, A7, 166, 196]. The Kane-Mele-Coulomb model was investigated by means of auxiliary-field quantum Monte Carlo in [A7]. The Kane-Mele-Hubbard model was also treated with approximate quantum cluster methods [197–201], variational Monte Carlo [202], slave-boson [203], slave-spin [204] and slave-rotor methods [205], as well as mappings to spin models to explore the regime of large U [206–208]. Field-theory methods were applied in [103, 209]. Extended Kane-Mele models with additional single-particle terms that can drive quantum phase transitions were studied with quantum Monte Carlo methods in [210–212]. There have also been substantial efforts to determine the topological invariant in the presence of correlations [199, 200, 210–216]. The Kane-Mele-Hubbard model with Rashba coupling was studied in [201]. Finally, the magnetic transition in the presence of spin-orbit coupling was investigated (mainly with quantum cluster methods) in other models of correlated topological insulators, including the Bernevig-Hughes-Zhang-Hubbard model [85, 205, 217, 218], the sodium-iridate model [57], the Hofstadter-Hubbard model [219], and the spinful Haldane-Hubbard model [220–227]. A related problem is the transition from a Chern insulator to a charge-density-wave insulator in the interacting spinless Haldane model [228–230], see also chapter 6.

4.1 Phase diagram

Several aspects of the phase diagram as a function of spin-orbit coupling and electron-electron interaction strength can be deduced from theoretical considerations. The semimetal is stable with respect to weak interactions [180]. Potential interaction-driven phase transitions that involve spontaneous symmetry breaking will therefore take place at a nonzero critical value U_c . Similarly, the noninteracting topological insulator is gapped and protected by time-reversal symmetry, and should therefore also remain stable up to a critical interaction strength.

¹Strictly speaking, the theorem only applies to systems with short-range interactions [187].

²The critical exponents deviate from the values expected from the dimension 2 + 1 of the corresponding classical theory and the symmetry of the order parameter.

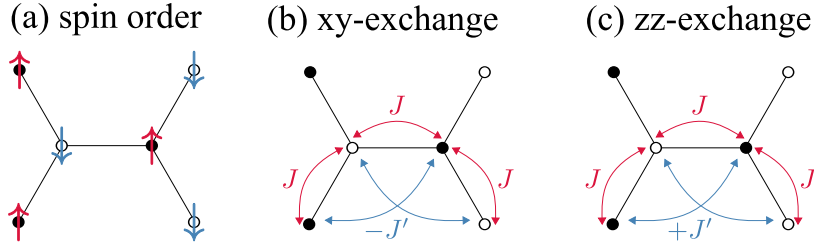


Figure 4.1: (a) Illustration of antiferromagnetic order on the honeycomb lattice. (b), (c) Exchange processes. The hopping t gives rise to kinetic superexchange J and favours antiferromagnetic alignment of nearest-neighbour-spins. Spin-orbit coupling leads to a next-nearest-neighbour exchange $\pm J'$. The latter is (b) ferromagnetic ($-J'$) for the x - and y -components but (c) antiferromagnetic (J') and hence frustrated for the z -components.

For the Hubbard model at half-filling, large values of U/t favour a uniform distribution of charges to avoid the energy penalty for doubly occupied sites. In this regime, charge fluctuations are hence strongly suppressed, and the low-energy physics is determined by the spin degrees of freedom. Second-order perturbation theory reveals that an antiferromagnetic arrangement of the electronic spins lowers the energy as it permits virtual hopping between nearest-neighbour lattice sites (kinetic superexchange) [231]. The low-energy physics is described by the antiferromagnetic honeycomb-Heisenberg model

$$H = J \sum_{\langle ij \rangle} \mathbf{S}_i \cdot \mathbf{S}_j \quad (4.1)$$

with exchange constant $J = 4t^2/U$, onto which the Hubbard model maps in the limit $U/t \rightarrow \infty$ [232]. For sufficiently large J , the ground state of the Heisenberg model is antiferromagnetic with spontaneously broken $SU(2)$ spin symmetry, as illustrated in figure 4.1(a). Together with the stability of the semimetal for weak interactions, we hence expect the honeycomb-Hubbard model to exhibit a magnetic phase transition at a nonzero U_c/t .

Similar reasoning applies for nonzero spin-orbit coupling. The quantum spin Hall state is stable for weak interactions. For $U \gg \lambda, t$, a low-energy description in terms of the spin degrees of freedom can be derived. The corresponding Hamiltonian is [82, 206, 207]

$$H = J \sum_{\langle ij \rangle} \mathbf{S}_i \cdot \mathbf{S}_j + J' \sum_{\langle\langle ij \rangle\rangle} (S_i^z S_j^z - S_i^x S_j^x - S_i^y S_j^y). \quad (4.2)$$

The first term is identical to equation (4.1). The spin-orbit coupling [a next-nearest-neighbour hopping term, cf. equation (2.13)] gives rise to a next-nearest-neighbour exchange coupling $J' = 4\lambda^2/U$ that is ferromagnetic in the transverse (spin- xy) direction and antiferromagnetic in the longitudinal (spin- z) direction. As illustrated in figures 4.1(b) and (c), the spin-spin interactions described by Hamiltonian (4.2) are frustrated for the S^z components but not for the S^x, S^y components. This suggests that for sufficiently large U the ground state will exhibit long-range antiferromagnetic order in the transverse direction, as opposed to Heisenberg order for $\lambda = 0$. For nonzero λ , we therefore expect a quantum phase transition between the topological insulator phase and an easy-plane antiferromagnetic phase at a critical $U_c > 0$.

4.1. Phase diagram

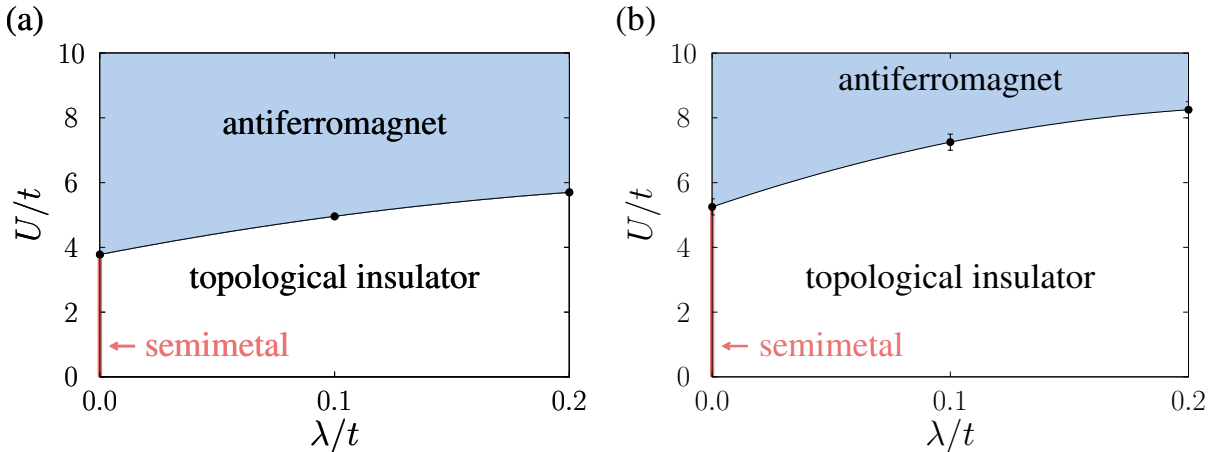


Figure 4.2: Phase diagram of (a) the Kane-Mele-Hubbard and (b) the Kane-Mele-Coulomb model with $\alpha = 1$. The phases are a semimetal for $\lambda = 0$ and $U < U_c(0)$, a topological insulator for $\lambda > 0$ and $U < U_c(\lambda)$, and an antiferromagnetic insulator for $U > U_c(\lambda)$. Figure adapted from [A7].

The above considerations have first been confirmed in a mean-field approach to the Kane-Mele-Hubbard model [82], yielding a phase diagram that consists of a semimetallic phase, a quantum spin Hall phase, and a magnetic insulating phase. Recent quantum Monte Carlo simulations [A7] yield a qualitatively identical phase diagram, which is shown in figure 4.2(a). From chapter 2 we know that the spin-orbit coupling is a relevant mass term for the semimetal. Accordingly, any $\lambda > 0$ opens a gap both for $U = 0$ and for $0 < U < U_c$ [A3], and the ground state becomes a topological insulator.³ Both the semimetal and the topological insulator are stable up to a critical interaction $U_c(\lambda)$. The magnetic transition is of second order [A3]; the universality and the determination of the magnetic phase boundary will be discussed below.

The agreement between mean-field and numerical results at weak and strong coupling is not surprising in view of the general arguments above. However, the role of quantum fluctuations at intermediate U/t is not clear *a priori*, especially due to the small coordination number of the honeycomb lattice ($z = 3$). Indeed, there has been an extended argument over the possibility of an intermediate phase in the honeycomb-Hubbard model [193–196, 235]. Finite-size scaling of quantum Monte Carlo results on lattices with up to 18×18 unit cells seemed to suggest a window around $U/t = 4$ in which the single-particle gap is nonzero but the system is not magnetically (or otherwise) ordered [193]. This region was originally interpreted as a quantum spin liquid, a phase with topological order in which quantum fluctuations prevent long-range order even at zero temperature [46]. Relying on the $\lambda = 0$ data from [193], the intermediate phase was argued to extend to nonzero spin-orbit coupling [A1, A3]. While the low coordination number and ring-exchange processes [236] provide possible mechanisms for the formation of such a phase, a strong counter argument is the absence of frustrated exchange interactions on the bipartite honeycomb lattice. Indeed, the phase was absent in earlier quantum Monte Carlo

³Direct evidence for a topological phase for $U < U_c$ will be given in section 4.3. Indirect evidence is provided by the fact that the single-particle gap remains nonzero [figure 4.5(b)] and time-reversal symmetry unbroken for $U < U_c$. However, a closing of the single-particle gap is not mandatory in the presence of interactions [233, 234].

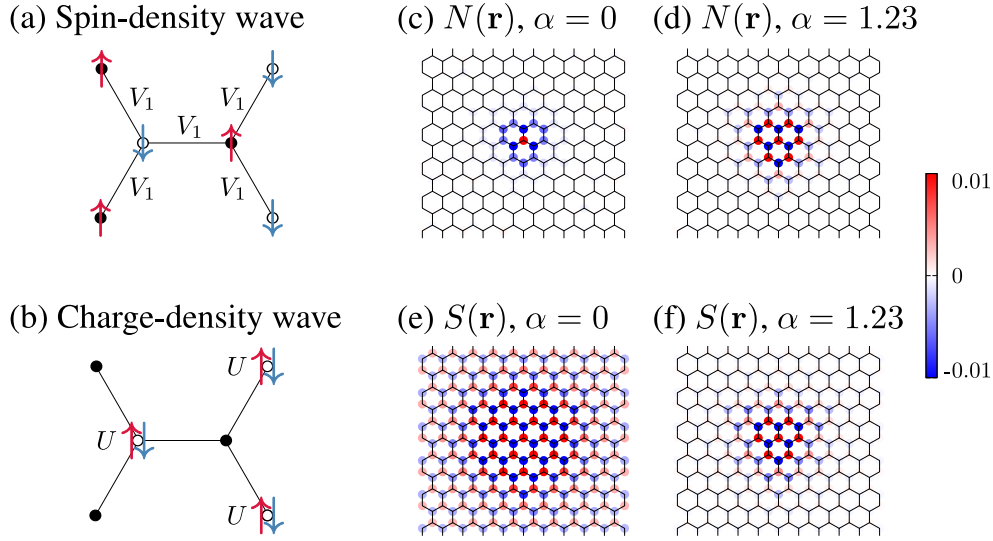


Figure 4.3: Illustration of (a) a spin-density wave and (b) a charge-density wave in the extended Hubbard model with onsite repulsion U and nearest-neighbour repulsion V_1 . (c)–(f) Real-space charge and spin correlations relative to the central site for (c)–(d) the Hubbard interaction ($\alpha = 0$) and (e)–(f) the Coulomb interaction ($\alpha = 1.23$). Here, $\lambda = 0$, $U/t = 3.5$, $L = 15$. Figure adapted from [A7].

results [179], and has since been essentially ruled out by simulations on much larger systems (up to 40×40 unit cells) [194] and the use of improved methods to determine the critical point [195] (pinning fields allow measuring m instead of m^2 , yielding more reliable results close to U_c). As discussed in more detail below, these results are consistent with a simultaneous onset of the single-particle gap and the magnetisation, and hence a direct transition between the semimetal and the antiferromagnet.

Finally, figure 4.2(b) shows the phase diagram of the Kane-Mele-Coulomb model for $\alpha = 1$,⁴ as obtained from quantum Monte Carlo simulations. Remarkably, it only differs from the Kane-Mele-Hubbard phase diagram [figure 4.2(a)] by the critical values. While the weak-coupling arguments given above for the Kane-Mele-Hubbard model remain unchanged, the analysis of the strong-coupling regime is complicated by the nonlocal interaction. Nevertheless, the differences observed for the Coulomb interaction can be qualitatively understood from the energetics of an extended Hubbard model with onsite repulsion U and nearest-neighbour repulsion V_1 . While U favours a spin-density-wave state with uniform charge density, the repulsion V_1 is minimised by a charge-density-wave state with all electrons on either the A or the B sublattice, see figures 4.3(a) and (b). Starting from the Hubbard limit ($V_1 = 0$), the energy difference between the spin-density wave and the charge-density wave reduces upon increasing V_1 . For the Coulomb interaction defined by equation (2.28), the two ground states become degenerate in the classical limit ($t = 0$) for $\alpha = 1.23$. More generally, the nonlocal part of the interaction promotes charge-density-wave correlations that compete with the antiferromagnetic correlations driven by the Hubbard term. This is illustrated by the numerical results of figures 4.3(c)–(f).

⁴See equation (2.28); both the local and nonlocal part of the interaction scale with U .

4.2. Magnetic phase transition

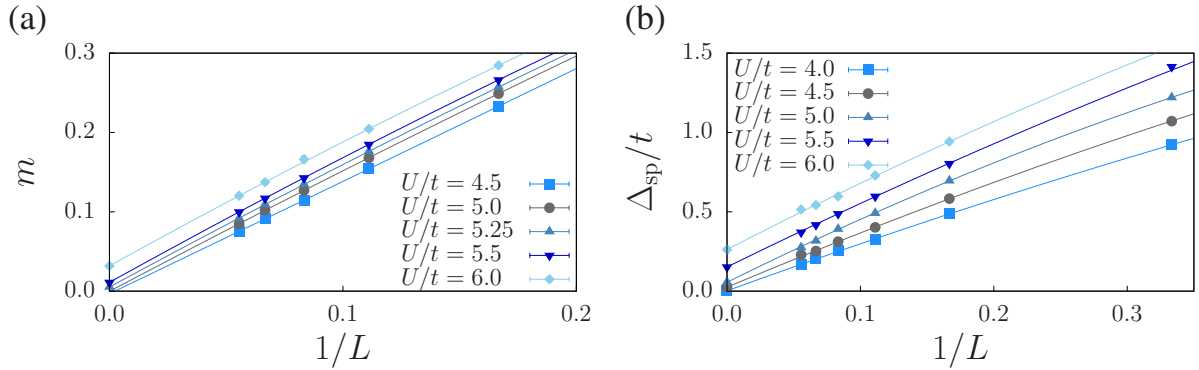


Figure 4.4: Finite-size scaling of (a) the magnetisation and (b) the single-particle gap at the Dirac point for the honeycomb-Coulomb model ($\lambda = 0$, $\alpha = 1$). Figure adapted from [A7].

The competition provides an explanation for the much larger critical values of the magnetic transition in the Kane-Mele-Coulomb model. However, our results suggest that it is insufficient to stabilise a charge-density-wave phase or the exotic QSH* phase [57].⁵ The interplay of charge and spin order on the honeycomb lattice has also been studied using field theory [184] and the functional renormalisation group [80, 185, 186]. Charge-ordered phases due to nonlocal interactions will be further discussed in chapter 6.

4.2 Magnetic phase transition

Having discussed the overall features of the phase diagram, we turn to a detailed discussion of the magnetic transition—an interaction-driven quantum phase transition at which the spin symmetry and time-reversal symmetry are spontaneously broken by the onset of long-range antiferromagnetic order. The critical point can be determined from quantum Monte Carlo simulations by a finite-size scaling of the antiferromagnetic structure factor S_{AF} . The latter corresponds to the $\mathbf{Q} = 0$ Fourier transform of the correlation function $\langle S_i \cdot S_j \rangle$ for $\lambda = 0$, and of $\langle S_i^+ S_j^- + S_i^- S_j^+ \rangle$ for $\lambda > 0$. It is related to the magnetisation per site via $m = \sqrt{S_{\text{AF}}/N}$ [A7].

Figure 4.4(a) shows the finite-size scaling of m (using quadratic fits) for $\lambda = 0$ and a long-range Coulomb interaction with $\alpha = 1$. In the semimetal at small U/t , the magnetisation extrapolates to zero, whereas nonzero extrapolated values are obtained for large U/t . The data suggest an onset of long-range order between $U/t = 5$ and $U/t = 5.5$. In contrast, $U_c/t = 3.78(5)$ for a Hubbard interaction [195]. The critical point can also be determined from the opening of the single-particle gap Δ_{sp} . The finite-size scaling in figure 4.4(b) is slightly less accurate than that for the magnetisation but gives a consistent U_c [A7]. Estimates of U_c/t also vary slightly depending on the method and observable used, especially if the accessible system sizes are insufficient to capture the relevant length scales [195, 196, 235].

⁵The theory of [57] also gives a QSH* phase for the Kane-Mele-Hubbard model [237]. The absence of such a phase from the phase diagram of the latter may have been a consequence of the onset of magnetic order already at intermediate U/t . A suppression of magnetism by competing orders is hence a possible mechanism to reveal a potential QSH* phase, but this is not borne out in the numerical results for the Kane-Mele-Coulomb model.

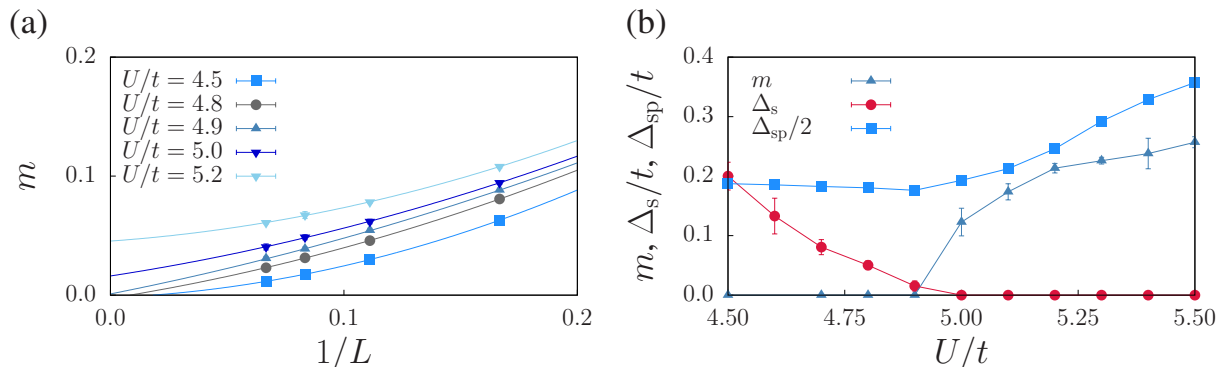


Figure 4.5: (a) Finite-size scaling of the (transverse) magnetisation for the Kane-Mele-Hubbard model. (b) Extrapolated magnetisation, spin and single-particle gap. Here, $\lambda/t = 0.1$. Figure adapted from [A3].

Results for the topological insulator to antiferromagnetic insulator transition in the Kane-Mele-Hubbard model with $\lambda/t = 0.1$ are shown in figure 4.5(a). The finite-size scaling of the magnetisation gives the estimate $U_c/t = 4.95(5)$. The critical point has also been determined from a finite-size scaling of the spin correlations at the largest distance for a given lattice size [A4], and from the single-particle and spin gaps [A3, A4, A7]. Figure 4.5(b) shows the extrapolated magnetisation and the spin gap Δ_s as a function of U/t , revealing the simultaneous onset of long-range order and closing of the spin gap at U_c . In contrast, the single-particle gap Δ_{sp} remains finite across the transition. The absence of a gap-closing does not contradict the discussion in chapter 2: because the protecting time-reversal symmetry is broken at U_c , the topological invariant can change without a closing of the single-particle gap.

The quantum Monte Carlo methods used here also permit to investigate the universality class of the magnetic transitions.⁶ According to Ginzburg-Landau-Wilson theory for second-order phase transitions [238, 239], quantities such as the magnetisation or the spin gap can be described by power-laws with universal critical exponents sufficiently close to the critical point. The exponents are determined by the dimension of the system and the symmetry of the order parameter. The above discussion of effective spin models revealed that the order parameter is different with and without spin-orbit coupling. For $\lambda = 0$, the magnetic order is identical to that of the Heisenberg model, corresponding to a spontaneously broken $SU(2)$ spin symmetry and antiferromagnetic ordering of all spin components. Spin-orbit coupling reduces the spin symmetry from $SU(2)$ to $U(1)$ already at the level of the Hamiltonian, see chapter 2. At the transition, the transverse components order (easy-plane antiferromagnetism), which breaks the remaining $U(1)$ spin symmetry and suggests 3D XY universality.

Another crucial difference between $\lambda = 0$ and $\lambda \neq 0$ is the nature of fermionic excitations in the disordered phase. For $\lambda = 0$, fermionic and spin excitations are gapless for $U < U_c$, as illustrated in figure 4.6(a). In contrast, the spin-orbit term opens a mass gap for single-particle and spin excitations, see figure 4.6(b). For $U > U_c$, in the ordered phase, the spin gap vanishes in both cases because the breaking of a continuous symmetry gives rise to a Goldstone

⁶The continuous nature of the topological insulator to antiferromagnet transition was explicitly demonstrated in terms of the derivative of the free energy in [A3].

4.2. Magnetic phase transition

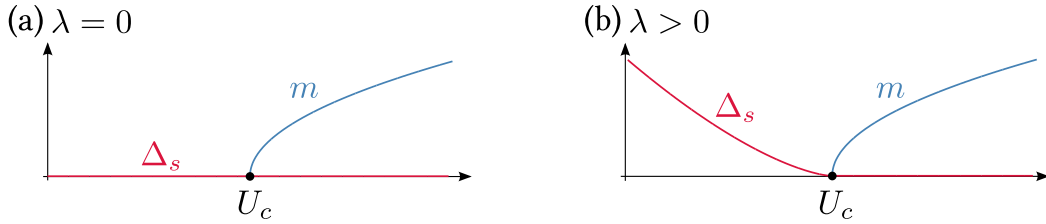


Figure 4.6: Schematic illustration of the behaviour of the magnetisation and the spin gap across the magnetic transition (a) without spin-orbit coupling, (b) with spin-orbit coupling.

mode (spin-wave excitations). While the spin gap hence serves as an order parameter for the transition at $\lambda \neq 0$, it is zero on both sides of the transition for $\lambda = 0$. Remarkably, field theory predicts a deviation from the Ginzburg-Landau-Wilson paradigm for the semimetal–Mott insulator transition caused by the coupling between the bosonic order parameter and the gapless Dirac fermions, as described by Gross-Neveu-Yukawa theory [79]. The critical point is predicted to exhibit SU(2) Gross-Neveu universality [79, 180]. The critical exponents in $2 + 1$ dimensions were estimated using a first-order ϵ -expansion around the upper critical dimension. This procedure yields $z = 1$, $\beta/\nu = 0.9$, and $\nu \approx 0.88$ [79].⁷ These values for the exponents were previously shown to be consistent with quantum Monte Carlo data for the magnetisation and the single-particle gap of the honeycomb-Hubbard model [195].

The agreement between numerics and field theory provides further evidence for a direct transition between the semimetallic and the antiferromagnetic phase; the best available estimate of the critical point is $U_c/t = 3.78(5)$ [195]. Although the data in [195] are consistent with Gross-Neveu universality (the collapse quickly deteriorates upon variation of $U_c^{(\epsilon)}$) it has to be kept in mind that in addition to corrections to scaling [196], the accuracy of the critical exponents is unknown for the present SU(2) case. However, a recent comparison between the ϵ -expansion and direct simulations of Z_2 and U(1) Gross-Neveu models showed good agreement [241, 242]. Comprehensive scaling analyses including estimates of critical exponents and results for the quasi-particle weight can be found in [196, 235]. Finally, Gross-Neveu-Heisenberg scaling was also confirmed in the presence of an interaction V_2 [153].

Here, we review similar results for the case of a long-range Coulomb interaction [A7]. For the latter, a large- N approximation predicts the long-range Coulomb tail to be irrelevant at the critical point [79] and hence the same universality class. Taking the exponents from the ϵ -expansion, we considered the finite-size, zero-temperature scaling law for the magnetisation,

$$m = L^{-\beta/\nu} F [(U - U_c)L^{1/\nu}], \quad (4.3)$$

with a universal scaling function F . According to equation (4.3), data for m obtained for different L should coincide at $U = U_c$, thereby yielding an estimate for the critical value. This expectation is confirmed by figure 4.7(a) which gives $U_c/t = 5.45(10)$, in agreement with figure 4.4. Equation (4.3) further implies that close to U_c a plot of $mL^{\beta/\nu}$ as a function of $(U - U_c)L^{1/\nu}$

⁷The exponent β describes the magnetisation near U_c , $m \sim (U_c - U)^\beta$; ν is the correlation-length exponent, $\xi \sim |U - U_c|^\nu$, and z is the dynamical critical exponent linking correlation time and length via $\xi_\tau = \xi^z$ [240]. In terms of the correlation length, we have $m \sim \xi^{-\beta/\nu}$ and $\Delta_s \sim \xi^{-z}$.

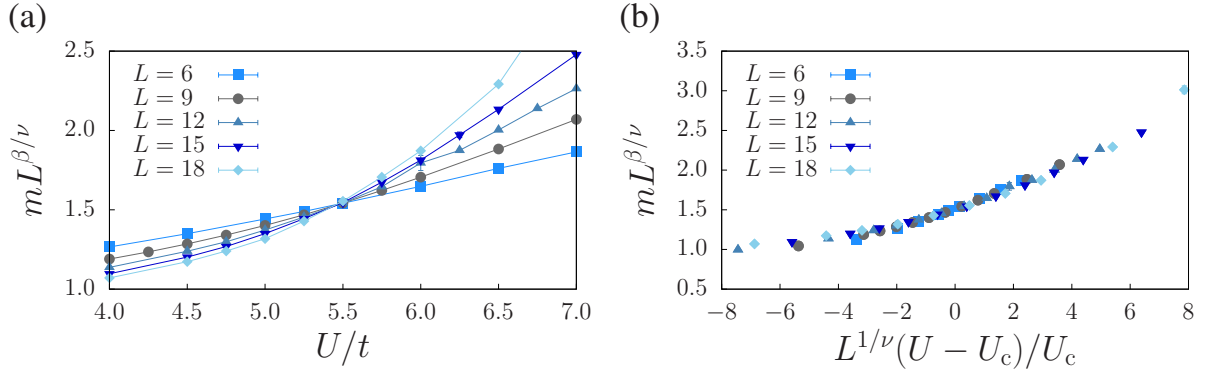


Figure 4.7: (a) Scaling intersection for the magnetisation using the Gross-Neveu critical exponents from the ϵ -expansion [79, 195]. (b) Scaling collapse using the critical value $U_c/t = 5.45$. Here, $\lambda = 0$, $\alpha = 1$. Figure adapted from [A7].

should produce a collapse onto the universal curve described by F . Such a collapse is indeed visible in figure 4.7(b). The results of figure 4.7 hence suggest that the universality class of the semimetal to antiferromagnet transition remains unchanged [SU(2) Gross-Neveu] for the long-range Coulomb interaction, in accordance with [79].

A similar investigation was carried out for the magnetic transition at nonzero spin-orbit coupling, i.e., between the topological insulator and the antiferromagnet. As argued above, based on the U(1) symmetry of the order parameter, the transition is expected to be in the 3D XY universality class [A1, 103, 209]. The critical exponents are known from simulations of the classical 3D XY model as $z = 1$, $\nu = 0.6717(1)$, and $\beta = 0.3486(1)$ [244]. Figure 4.8(a) shows that magnetisation data for the Kane-Mele-Hubbard model with $\lambda/t = 0.1$ intersect at a value $U_c/t = 4.96(4)$ that agrees well with the finite-size scaling in figure 4.5(a). Moreover, a rather good scaling collapse is observed in figure 4.8(b). The 3D XY scaling has also been verified for other values of λ/t [A3, A4], and the spin gap Δ_s [A3]. Finally, good agreement with 3D XY universality is also found for the case of long-range Coulomb interaction [A7].

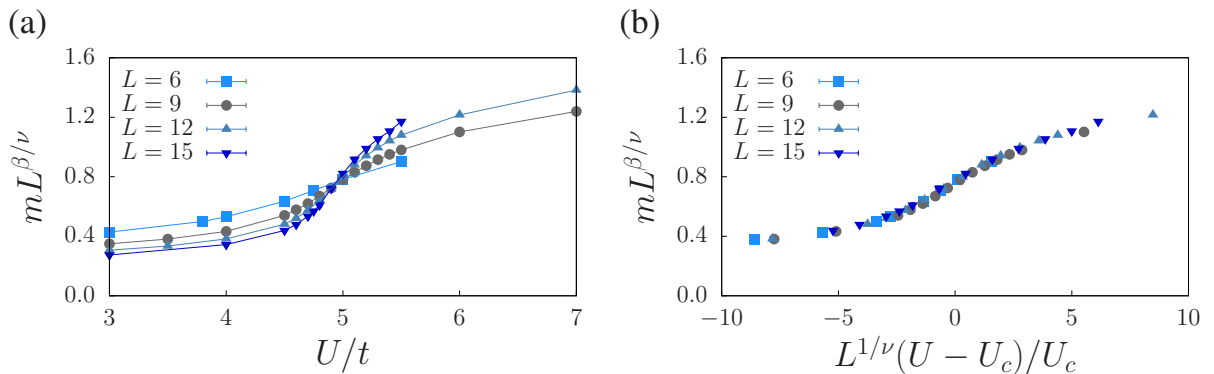


Figure 4.8: (a) Scaling intersection for the magnetisation using the 3D XY critical exponents [243]. (b) Scaling collapse using $U_c/t = 4.96$. Here, $\lambda/t = 0.1$, $\alpha = 0$. Figure adapted from [A3].

4.3. Topological invariant from π -fluxes

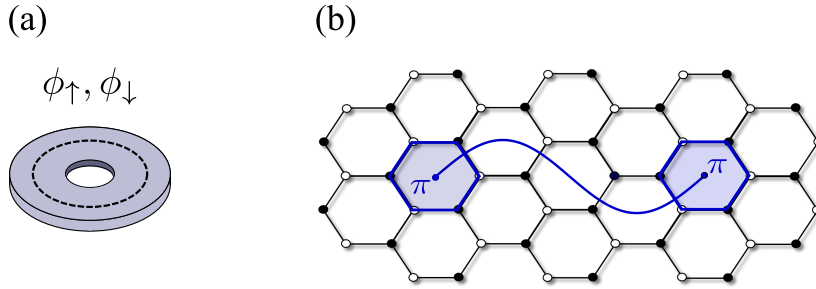


Figure 4.9: (a) The existence of fluxon states can be inferred by considering transport across a Gaussian loop (dashed line) upon adiabatic insertion of magnetic fluxes $\phi_{\uparrow}, \phi_{\downarrow} = \pm\pi$ through a hole in a topological insulator [248].⁹ (b) For a honeycomb lattice with periodic boundaries, π -fluxes can be inserted in pairs. Each flux threads a hexagon (highlighted in blue), and a flux pair is connected by a branch cut (blue line). Hopping processes crossing the cut acquire a phase $e^{i\pi} = -1$. Figure adapted from [A4, 248].

4.3 Topological invariant from π -fluxes

In the discussion of the phase diagram, we argued that the nonzero single-particle gap and time-reversal symmetry imply a topological insulator state for $U < U_c(\lambda)$. Clearly, it is desirable to detect the correlated topological phase directly, especially in searching for interaction-generated topological phases. To do so in an unbiased and efficient way is nontrivial. For example, while the bulk-boundary correspondence implies the existence of gapless helical edge states in noninteracting systems [9, 24], correlation and finite-size effects can gap out the edge states (see chapter 5), leading to a breakdown of the bulk-boundary correspondence [233, 234]. A direct numerical calculation of Chern numbers from the Kubo formula [245] is difficult using imaginary-time quantum Monte Carlo simulations, but has been achieved with quantum cluster methods [217]. If spin is conserved, the Z_2 invariant can then be calculated from C^{\uparrow} and C^{\downarrow} [98, 99]. Finally, it has been proposed to extract the topological invariant from the single-particle Green function using the topological Hamiltonian [246], a trace formula [247], or by analysing the zeros and poles [233, 234, 247]. However, this approach relies on the assumption of an adiabatic connection to a noninteracting state and is hence not unbiased [233]. Quantum Monte Carlo results for the Kane-Mele-Hubbard model reveal that the Green function method fails to capture the change of the topological invariant at U_c [210, 211, 213–215] due to the absence of spontaneous symmetry breaking on finite lattices.

A useful alternative that can easily be combined with quantum Monte Carlo simulations and captures the magnetic transition is based on the response to a π gauge flux [248, 249]. It can be understood from the noninteracting case, but remains fully valid in the presence of interactions [248, 249]. A π -flux⁸ preserves time-reversal symmetry. It represents a topological defect and, analogous to solitons in polyacetylene [94], is associated with characteristic mid-gap states. For π -fluxes in topological insulators, a pumping argument⁹ [248] shows that the quantised

⁸A flux of size $hc/2e$, half the flux quantum for particles with charge e ; $hc/2e = \pi$ in units where $\hbar = c = e = 1$.

⁹Imagine a disk-shaped topological insulator with a hole through which fluxes $\phi_s = \pm\pi$ are adiabatically inserted [figure 4.9(a)]. The time-dependent fluxes induce a tangential in-plane electric field. Because of the quantised spin-Hall response, the field gives rise to a net pumping of charge (for $\phi_{\uparrow} = -\phi_{\downarrow}$) or spin ($\phi_{\uparrow} = \phi_{\downarrow}$) across the dashed Gaussian loop, implying the existence of in-gap fluxon states [248].

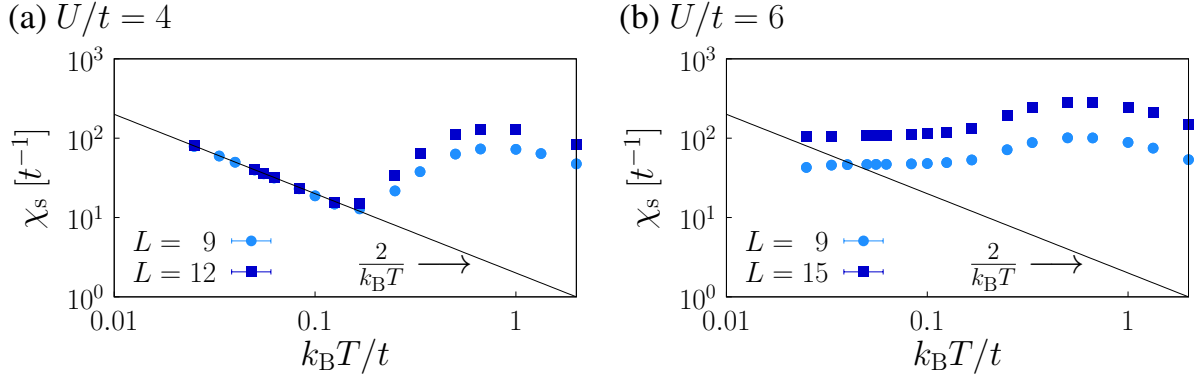


Figure 4.10: Magnetic susceptibility of the Kane-Mele-Hubbard model with one pair of π -fluxes. Here, $\chi_s = \beta(\langle \hat{M}_z^2 \rangle - \langle \hat{M}_z \rangle^2)$ with $\hat{M}_z = \sum_i c_i^\dagger s^z c_i$. (a) In the topological phase, the spin fluxons give rise to a Curie law $\chi_s = 2/k_B T$ at low temperatures, while no such contribution is observed in (b) for the antiferromagnetic phase. Figure adapted from [A4].

spin-Hall conductivity gives rise to two *charge-fluxon states* (charge $\pm e$, spin zero) and two *spin-fluxon states* (charge zero, spin $\pm 1/2$). The spin fluxons form a Kramers doublet related by time-reversal symmetry; they behave like a localised magnetic moment with $S = 1/2$ [248, 249]. Importantly, the fluxon states—similar to the helical edge states—exist even in the presence of Rashba coupling (when $\sigma_{xy}^{\text{spin}}$ is no longer quantised) or interactions (as long as time-reversal symmetry is not broken) [248]. In particular, while repulsive interactions split the degeneracy of the charge-fluxon states, the spin fluxons remain at zero energy [248].

Within a Hamiltonian description, a gauge flux can be implemented in the form of a branch cut (Dirac string) from the flux position to infinity that attaches a phase $e^{i\pi} = -1$ to each hopping process across the cut [250, 251]. For the case of periodic boundary conditions usually used for simulations, fluxes can be inserted in pairs connected by a branch cut, see figure 4.9(b). Importantly, the Monte Carlo configuration weights remain positive [A4].

Figure 4.10(a) shows a clear Curie-law signature from the spin fluxons in the low-temperature magnetic susceptibility in the correlated topological phase ($\lambda/t = 0.2$, $U/t = 4$). In contrast, no such contribution exists in the topologically trivial antiferromagnetic phase ($U/t = 6$). The flux-induced spinon states are also clearly visible in the site-resolved dynamic spin structure factor $S(i, \omega)$ [A4]. Integrating this quantity up to an energy scale smaller than the bulk gap gives the fluxon spectral weight shown in figure 4.11. In the topological phase [figure 4.11(a)], a clear response is visible in the vicinity of the flux-threaded plaquettes, also confirming the localised nature of the fluxons. In contrast, the spectral weight is orders of magnitude smaller in the trivial phase [figure 4.11(b)]. Tracking the fluxon spectral weight as a function of U/t reveals the magnetic transition [A4].

π -fluxes can also be used to construct novel quantum spin models by exploiting the interaction between the localised spin fluxons mediated by the magnetic excitations of the topological insulator [A4]. Finally, putting the Kane-Mele model on a π -flux honeycomb lattice in the spirit of [252] produces several topologically different ground states [A8].

4.3. Topological invariant from π -fluxes

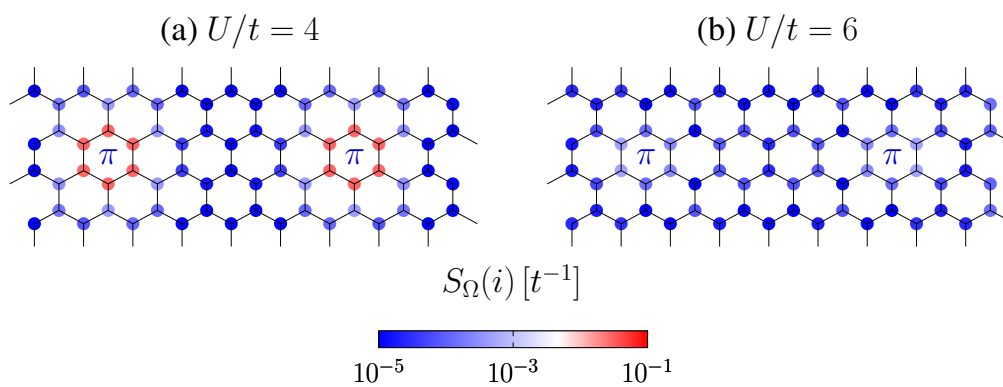


Figure 4.11: Integrated spectral weight of low-energy spin excitations $S_{\Omega}(i)$ in the presence of two π -fluxes for (a) the topological phase and (b) the antiferromagnetic phase. Figure adapted from [A4].

5 Edge correlation effects

This chapter is concerned with the question how (strong) electron-electron interactions affect the characteristic helical edge states of two-dimensional topological insulators. The discussion is based on quantum Monte Carlo results obtained for the Kane-Mele model (2.13) with a Hubbard interaction [equation (2.27)] only at the edge [A1, A2, A9]. While the edge states are typically studied with the bosonisation method [253]—corresponding to a purely one-dimensional description—we took into account the two-dimensional bulk as well to obtain results valid beyond the low-energy limit. A key point to be addressed here is whether the bosonisation predictions [102, 108] are borne out by numerical simulations.

In contrast to the gapped bulk, the gapless edges are very susceptible to interaction effects. While HgTe/CdTe edge states appear to be weakly correlated, stronger correlations have been reported for InAs/GaSb [53]. Mean-field theory produces an insulating edge with long-range, transverse magnetic order for any $U > 0$ due to a divergent magnetic susceptibility [103]. Such edge magnetism has also been studied in the context of graphene [254–258]. Taking into account spin-wave fluctuations yields power-law correlations for sufficiently weak coupling [103]. The correlations at the edge are determined by the interaction strength and the bare Fermi velocity v_F . Because the edge states on a zigzag edge connect the valence and conduction bands [see figure 2.5(b)], v_F is determined by the bulk band gap $\Delta_{SO} \sim \lambda$; in particular, $v_F \rightarrow 0$ for $\lambda \rightarrow 0$.¹ The Fermi velocity can be tuned in experiments with InAs/GaSb [53].

As argued in chapter 2, the same low-energy edge theory [equation (2.24)] arises for different models and edge geometries. While the present method is applicable to more general situations (e.g., edges with magnetic impurities [260] or two pairs of edge states [A8]), we focus on the fundamental case of a single pair of edge states realised in HgTe as well as in the Kane-Mele and Bernevig-Hughes-Zhang models. For the Kane-Mele-Hubbard model on a zigzag ribbon, the protected crossing of the edge states is at $k = \pi$ [figure 2.5(b)]. The effective model was solved exactly with the CT-INT quantum Monte Carlo method of section 3. Restricting interactions to the edge permitted us to include Rashba spin-orbit coupling, as described by equation (2.25).

Within the universal low-energy description, the types of allowed interactions depend on the symmetries of the system. In particular, time-reversal symmetry does not allow elastic single-particle backscattering (the most relevant perturbation in ordinary one-dimensional metals [109]), and spin-conservation in the absence of Rashba coupling rules out umklapp scattering. However, given a half-filled band and nonzero Rashba coupling, the bosonisation predicts that strong umklapp scattering will cause an edge-Mott transition, and hence a breakdown of the bulk-boundary correspondence. In contrast, the correspondence remains intact across the

¹For armchair edges, the edge states cross at $k = 0$ and v_F depends only weakly on λ . In particular, the edge states do not flatten for $\lambda \rightarrow 0$ [259].

5.1. Effective model

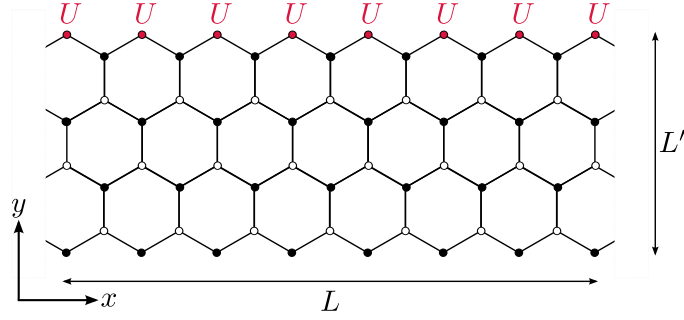


Figure 5.1: Correlated helical edge states were simulated in terms of the Kane-Mele model on $L \times L'$ zigzag ribbons with periodic (open) boundary conditions in the x - (y -) direction. A Hubbard repulsion U was taken into account only at the outermost sites of the upper edge. The resulting effective model, defined by equation (5.1), can be simulated exactly with the CT-INT method.

bulk magnetic transition of chapter 4 which gaps out the edge states at the same time [197].

With more general reviews of helical edge states available [1, 14, 261], we only mention the literature relevant for the discussion in this chapter. Bosonisation analyses of interaction effects in helical Luttinger liquids were presented in [8, 102, 108]. The stability with respect to Rashba coupling and disorder in the absence of interactions was demonstrated numerically in [98]. The impact of spin fluctuations around the mean-field saddle point was studied in [103], while the bulk-boundary correspondence in the presence of interactions was addressed in [233, 234]. Numerical studies of correlation effects were carried out using quantum Monte Carlo methods [A1, A2, A9, 166, 202] and quantum cluster methods [197, 198, 202, 217, 262].

5.1 Effective model

While the strictly one-dimensional bosonisation approach captures the physics in the low-energy limit, such theories have anomalies that reflect the holographic nature of the edge states of quantum Hall and quantum spin Hall systems. Moreover, when interactions are large compared to the bulk band gap, or at finite temperature [53], bulk states become relevant and a complete theory requires a two-dimensional description. However, large lattices are necessary to recover the asymptotic properties at large length scales along the edge, and to avoid spurious edge-edge hybridisation gaps. Such system sizes are beyond the capabilities of auxiliary-field quantum Monte Carlo, exact diagonalisation, and cluster methods, although such methods have been applied to Kane-Mele [166] and Haldane models [229, 230, 263].

To overcome these restrictions, an accurate effective model was developed in the form of a two-dimensional quantum spin Hall system with electron-electron interaction only at the edge [A1], as illustrated for the Kane-Mele-Hubbard model on a zigzag ribbon in figure 5.1. In the general case with Rashba coupling, the effective model is defined by the action [A9]

$$S[\bar{\Psi}, \Psi] = - \iint_0^\beta d\tau d\tau' \sum_{ij} \bar{\Psi}_i(\tau) g_{ij}^{-1}(\tau, \tau') \Psi_j(\tau') + \frac{U}{2} \int_0^\beta d\tau \sum_i [\bar{\Psi}_i(\tau) \Psi_i(\tau) - 1]^2. \quad (5.1)$$

The sums are over the correlated edge sites, $\mathbf{g}_{ij}(\tau, \tau')$ is the 2×2 block matrix containing the Green functions $g_{ij}^{ss'}(\tau, \tau') = \langle c_{is}^\dagger(\tau) c_{js'}(\tau') \rangle_0$ of the two-dimensional Kane-Mele model (2.13), and $\bar{\Psi} = (\bar{\psi}_\uparrow, \bar{\psi}_\downarrow)$ is a Grassmann spinor.

The restriction of interactions to edge sites is based on two arguments. First, correlation effects are much more pronounced at the gapless edges than in the gapped bulk. In particular, the dominant transverse spin correlations are generically much stronger at the edge [166], and for a wide range of parameters the edge-Mott transition is expected to take place well before the bulk magnetic transition. Therefore, it is sensible to neglect minor bulk interaction effects [A3] in studying the edge physics. Second, the edge states are exponentially localised near the edge; for a zigzag ribbon, the local density of states at E_F is nonzero only on the outermost sites where the interaction is taken into account. The possibility of tunnelling between edge and bulk states and the ensuing nonconservation of charge and spin at the edge reflect the physical situation in topological insulators. For the results shown below, the ribbon width was fixed to $L' = 64$, sufficient to avoid any edge-edge hybridisation effects [103, 264, 265].

The model defined by equation (5.1) can be solved exactly using the CT-INT quantum Monte Carlo method outlined in chapter 3. Most importantly, the numerical effort is independent of the ribbon width L' [A1, A2]. This makes the problem computationally equivalent to that of a one-dimensional chain and allowed us to simulate system sizes not accessible with any other numerical method. Because the number of interacting sites grows only with L , the sign problem that occurs for nonzero Rashba coupling (see chapter 3) is not prohibitive, in contrast to simulations of the full Kane-Mele-Hubbard model. It is straight-forward to derive similar effective models for other edge geometries or models of topological insulators, e.g., for the Bernevig-Hughes-Zhang model [12].

5.2 Generic correlation effects

The left- and right-moving edge states are related by time-reversal, and hence form an orthogonal Kramers doublet with a symmetry-protected crossing at either $k = 0$ or $k = \pi$. The corresponding low-energy theory is given by equation (2.24). Unless the protecting symmetry is broken, only interactions that respect time-reversal symmetry are allowed [8, 102, 108]. In particular, this excludes elastic single-particle backscattering terms of the form $\Psi^\dagger s^x \Psi$, $\Psi^\dagger s^y \Psi$ [8]. In this section, we consider the impact of forward scattering $\psi_\uparrow^\dagger \psi_\uparrow \psi_\downarrow^\dagger \psi_\downarrow$, whereas umklapp scattering will be discussed in section 5.3. While the numerical results have been obtained for a half-filled band, the interaction effects discussed in this section are generic for any band filling. In contrast to single-particle backscattering, two-particle backscattering is not forbidden by time-reversal symmetry [102, 108].

The effects of forward scattering can be described using the bosonisation method. For a helical liquid, the resulting theory has half the number of degrees of freedom of a spinful Luttinger liquid, and can be written as [102, 108].

$$H = \frac{v}{2} \int dx [K^{-1}(\partial_x \phi)^2 + K(\partial_x \theta)^2], \quad (5.2)$$

5.2. Generic correlation effects

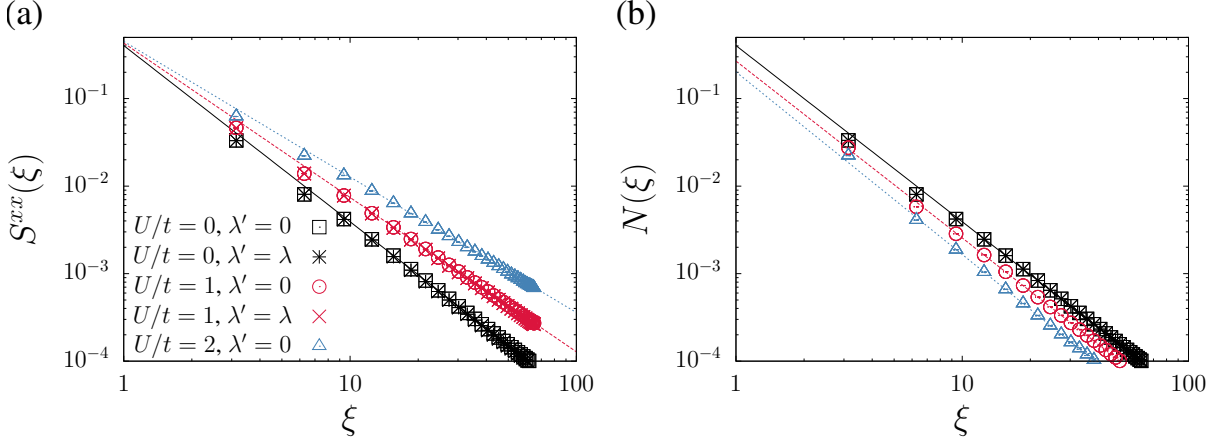


Figure 5.2: Real-space spin and charge correlation functions from projective CT-INT simulations of equation (5.1). Here, $\lambda/t = 0.2$, and $L = 65$. ξ is the conformal distance, see text. Lines are fits to a/ξ^b at large distances. Figure adapted from [A9].

with fields $\phi = \phi_{\uparrow} + \phi_{\downarrow}$ and $\theta = \phi_{\uparrow} - \phi_{\downarrow}$. This theory is quadratic and hence exactly solvable [253]. Interactions renormalise the Luttinger parameter K and the velocity v . We have $K = 1$ and $v = v_F$ for the noninteracting case, and $K < 1$ ($K > 1$) for repulsive (attractive) interactions.² For the case of the Kane-Mele-Hubbard model with a zigzag edge $v_F \sim \lambda$. Therefore, edge correlation effects in the effective model depend on the ratio U/λ [A2]. Estimates for the Luttinger parameters K and v from simulations are given in figure 5.4(a).

As characteristic for Luttinger liquids, correlation functions decay with power-laws. In particular, the equal-time spin correlation functions are given by [A2]³

$$S^{xx}(x) = \langle \hat{S}^x(x) \hat{S}^x(0) \rangle \sim \frac{\cos(2k_F x)}{x^{2K}}, \quad (5.3)$$

$$S^{zz}(x) = \langle \hat{S}^z(x) \hat{S}^z(0) \rangle \sim \frac{1}{x^2}, \quad (5.4)$$

whereas charge correlations decay as [A2]

$$N(x) = \langle \hat{n}(x) \hat{n}(0) \rangle \sim \frac{1}{x^2}. \quad (5.5)$$

While the decay of S^{zz} and N is predicted to remain unchanged in the presence of interactions, transverse spin correlations (S^{xx}) should be enhanced by repulsive interactions $U > 0$ for which the exponent $2K$ decreases with increasing U . Similar to chapter 4, the asymmetry between S^{xx} and S^{zz} is due to spin-orbit coupling.

²For a Hubbard interaction and weak-coupling [A2]

$$K = \sqrt{\frac{v_F - U/2\pi}{v_F + U/2\pi}}, \quad v = \sqrt{v_F^2 - (U/2\pi)^2}.$$

³There are no logarithmic corrections to these correlation functions [A2].

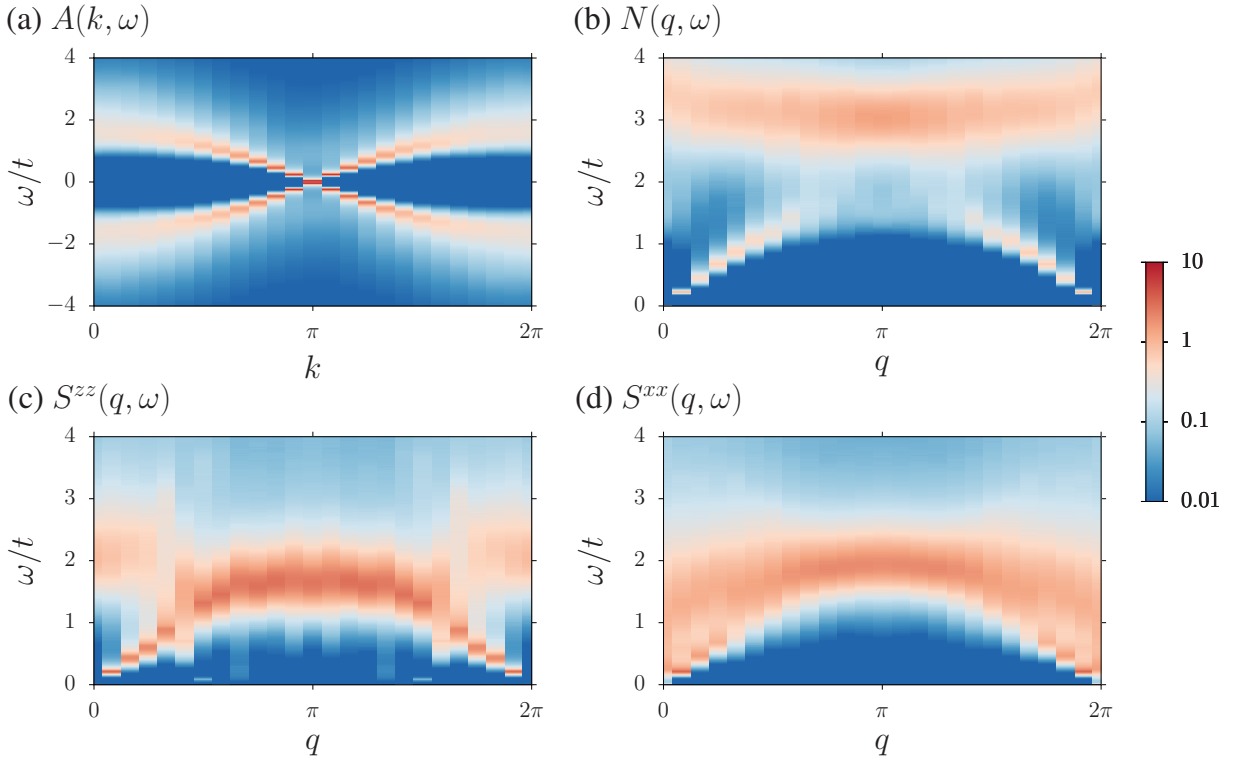


Figure 5.3: Excitation spectra for (a) single-particle, (b) charge, (c) longitudinal spin, and (d) transverse spin excitations from projective CT-INT simulations of the effective model (5.1). Here, $\lambda/t = 0.2$, $L = 24$, and $U/t = 2$. Figure adapted from [1].

The bosonisation predictions can be tested using the effective model (5.1). Figure 5.2 shows spin and charge correlation functions for different values of U/t . To reveal the expected power-laws, the results are plotted in terms of the conformal distance $\xi = L \sin(\pi x/L)$ [266]. For $U/t = 0$ we see the $1/x^2$ decay characteristic of noninteracting fermions. With increasing U/t , the transverse spin correlations decay more slowly with distance, while the charge correlations retain the same power-law exponent. The numerical results are hence fully consistent with equations (5.3) and (5.5). Power-law fits to S^{xx} at large distances produced $K = 0.882(1)$ for $U/t = 1$ and $K = 0.774(2)$ for $U/t = 2$ for the parameters of figure 5.2. While S^{xx} does not exhibit any oscillations in the half-filled case shown in figure 5.2, the $\cos(2k_F x)$ contribution in equation (5.3) becomes visible upon doping [A2]. Within the effective model, the magnetic correlations are ferromagnetic along the chain of interacting sites shown in figure 5.1. Finally, the numerical results in figure 5.2 reveal no significant impact of the Rashba spin-orbit term ($\sim \lambda'$), even for sizeable values $\lambda' = \lambda$; the correlation functions are virtually identical, in accordance with the fact that the Rashba term is an irrelevant perturbation of the Luttinger liquid fixed point at weak coupling. Our results show that the edge states are indeed well described by the helical Luttinger model, even for interactions U larger than the bulk band gap.

Using the maximum entropy method [267] for the analytic continuation from imaginary

5.3. Edge-Mott transition

time to real frequencies,⁴ we also calculated spectral functions. Figure 5.3(a) shows the single-particle spectral function for $U/t = 2$, revealing the expected crossing of the edge states at $k = \pi$ as well as the high-energy bulk states not captured by the bosonisation. The absence of any features related to spin-charge separation is a generic feature of one-dimensional systems with spin-orbit coupling [269]. Interaction effects manifest themselves in terms of a reduced Fermi velocity $v < v_F$ [see also figure 5.4(a)] and a suppression of spectral weight near the Fermi level [A1]. The single-particle spectrum of edge states of correlated topological insulators has also been obtained with quantum cluster methods [197, 198, 262, 265, 270].

Figures 5.3(b)–(d) show results for two-particle excitation spectra. The charge structure factor in figure 5.3(b) and the longitudinal spin structure factor in figure 5.3(c) exhibit a linear mode at long wavelengths with the renormalised velocity v , which can be related to spin-conserving excitations within the helical low-energy branches. In contrast, excitations at higher energies involve bulk states and are not spin-selective. The spectral weight at low energies is smaller for charge than for spin excitations. In particular, the spectral weight Z for low-energy charge excitations⁵ is continuously suppressed with increasing U , see figure 5.4(a). Finally, the transverse spin structure factor in figure 5.3(d) involves excitations between the two helical modes and therefore exhibits a continuum of low-energy excitations near $q = 0$.

5.3 Edge-Mott transition

The effects of forward scattering discussed in the previous section are generic for correlated helical liquids. Correlation functions change via the parameters K and v , but the edge states remain gapless and critical even for strong coupling. Under special conditions, namely for a half-filled band and in the presence of Rashba spin-orbit coupling, a helical liquid can undergo a Mott transition to a state with long-range magnetic order at zero temperature [102, 103, 108]. At this edge-Mott transition, time-reversal symmetry is spontaneously broken at the edge at $T = 0$. Since interaction effects are generally stronger at the edge than in the bulk, this allows for a quantum spin Hall insulator with gapped edge states, and hence a breakdown of the bulk-boundary correspondence in interacting systems [108, 234]. The Mott transition at the edge is to be contrasted with the opening of a gap in the edge states driven by the onset of long-range magnetic order in the bulk. In the latter case, time-reversal symmetry is broken in the entire system, and the quantum spin Hall state is destroyed. A bulk magnetisation m acts as a transverse magnetic field at the edge, leading to a relevant mass term (single-particle backscattering) $\sim m(\psi_\uparrow^\dagger \psi_\downarrow + \psi_\downarrow^\dagger \psi_\uparrow)$ and a gap in the edge states [103, 197].

The edge-Mott transition is the result of umklapp scattering [102],

$$H_u = \int dx \left[e^{-i4k_F x} \psi_\uparrow^\dagger(x) \psi_\uparrow^\dagger(x+a) \psi_\downarrow(x+a) \psi_\downarrow(x) + \text{H.c.} \right], \quad (5.6)$$

corresponding to scattering of two electrons from the \uparrow to the \downarrow branch (or vice versa) and a momentum transfer $\pm 4k_F$. Such processes do not conserve spin, and hence require a Rashba

⁴ The results shown here were obtained with the so-called stochastic maximum-entropy method [268].

⁵ Z is related to the Drude weight via $D = Zv$ [A2].

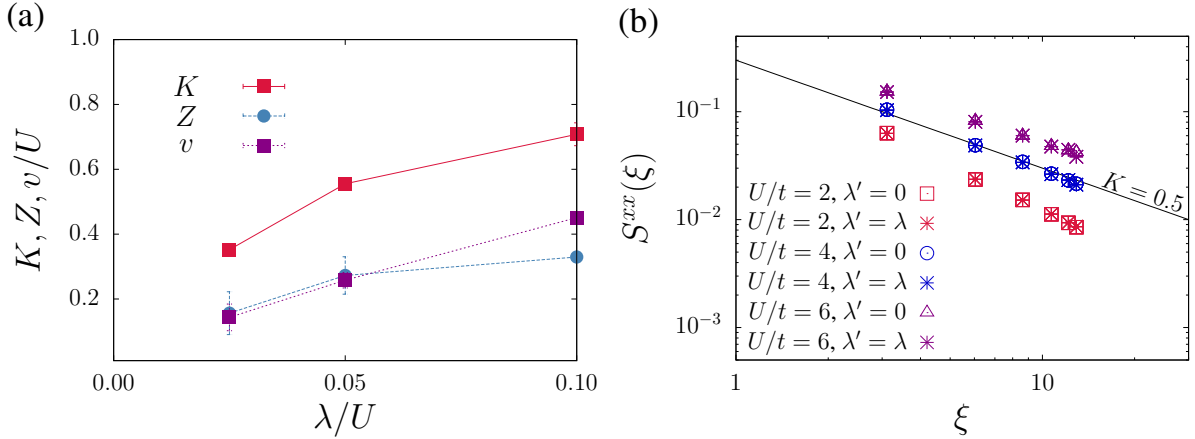


Figure 5.4: (a) Luttinger parameter K , renormalised velocity v , and charge spectral weight Z . (b) Real-space transverse spin correlations. Results obtained from projective CT-INT simulations of the effective model (5.1). The solid line in (b) illustrates the $1/x$ decay expected for $K = 1/2$, see equation (5.3). Here, $\lambda/t = 0.2$, and $L = 13$. Figure adapted from [A2, A9].

spin-orbit term to be present. This is the case in most experimental situations, and Rashba coupling was also taken into account within the effective model (5.1). The second condition for umklapp scattering to play a role is for the band to be half-filled (the case usually considered in numerical simulations but not generic for experiments), so that the total change of momentum equals a reciprocal lattice vector, $4k_F = 2\pi$.

A renormalisation group analysis [102, 108] reveals that umklapp scattering becomes a relevant perturbation of the helical Luttinger liquid for $K < 1/2$, that is, beyond a critical interaction strength. At $K = 1/2$, the transverse spin correlations S^{xx} become long-ranged (formally described by $K = 0$). The order breaks time-reversal symmetry and opens a Mott gap in the edge states. Because the edge states are one-dimensional at sufficiently low energies, the possibility of long-range magnetic order crucially relies on the reduced, discrete (Z_2) spin symmetry of the model in the presence of Rashba coupling which permits Ising long-range order at $T = 0$.⁶

While the renormalisation group analysis of the helical Luttinger liquid clearly predicts a Mott transition at $K = 1/2$, we investigated to what extent this transition can be observed numerically, and how the Mott regime differs from generic correlation effects at strong coupling. To this end, we compared simulation results with and without Rashba coupling λ' . Whereas the helical liquid remains gapless even for strong interactions in the absence of umklapp scattering for $\lambda' = 0$, a gapped Mott state is expected for $\lambda' \neq 0$ and U large enough to achieve $K < 1/2$. Previous numerical results for K in the Kane-Mele-Hubbard model imply that the Mott regime is realised in a wide region of parameters [A2, 166], see also figure 5.4(a).

Because $K > 1/2$ for the results in figure 5.2, Rashba coupling was irrelevant. Figure 5.4(b) shows results for the transverse spin correlations for stronger interactions U . Because the nu-

⁶For graphene (typically modelled with $\lambda = \lambda' = 0$), the Mermin-Wagner theorem [187] has been argued to be invalid because the unscreened interaction is momentum-dependent, thereby allowing for a spontaneous breaking of the continuous $U(1)$ spin symmetry at the edge [257, 258].

5.3. Edge-Mott transition

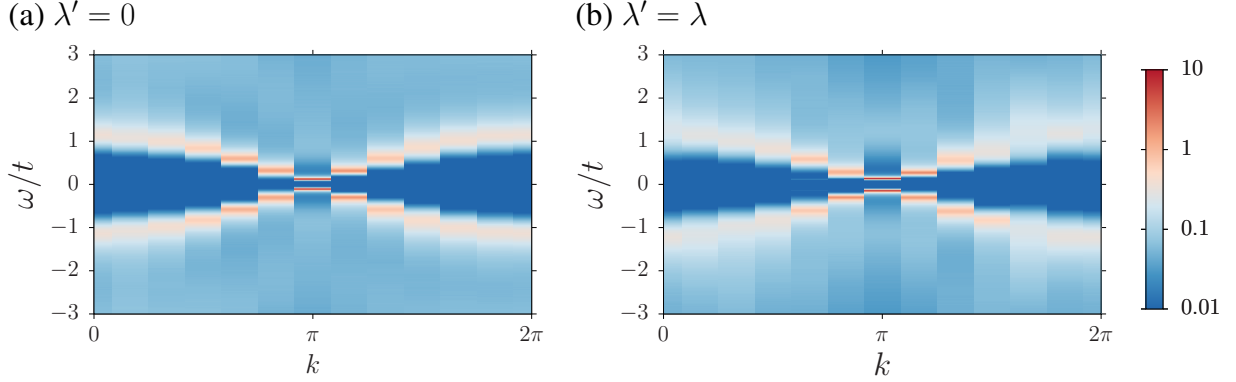


Figure 5.5: Single-particle spectral function from CT-INT simulations of the effective model (5.1). Here, $\lambda/t = 0.2$, $U/t = 6$, and $L = 12$. Figure adapted from [A9].

merical effort for solving the effective model with the CT-INT method scales as U^3 , the system size in the periodic direction (along the edge) is significantly smaller ($L = 13$) than in figure 5.2 ($L = 65$). To estimate the Luttinger parameter K , the solid line in figure 5.4(b) illustrates the $1/x$ decay expected for $K = 1/2$. For the parameters chosen, the critical value for the Mott phase appears to be reached between $U/t = 4$ and $U/t = 6$. Interestingly, the correlations are again comparable for simulations with and without Rashba coupling. However, for the system size used and for large U , we cannot reliably distinguish between a slow power-law decay (slower than $1/x$) and potential long-range order.

To detect the expected Mott gap, we considered the single-particle spectral function

$$A(k, \omega) = -\frac{1}{\pi} \text{Im} G(k, \omega), \quad G(k, \omega) = \frac{1}{2} [G^{\uparrow\uparrow}(k, \omega) + G^{\downarrow\downarrow}(k, \omega)], \quad (5.7)$$

with the spin-diagonal single-particle Green functions G^{ss} . Figure 5.5 shows the single-particle spectral function at very low temperature ($\beta t = 60$) for strong coupling $U/t = 6$. In contrast to the weak-coupling spectral function in figure 5.3(a), we see a correlation-induced gap at the Fermi level both for $\lambda' = 0$ and $\lambda' \neq 0$. Although the gap is slightly smaller than for $\lambda' \neq 0$, its existence for $\lambda' = 0$ has to be reconciled with the fact that umklapp scattering and hence a Mott phase are absent in helical liquids without Rashba coupling.

Because the calculation of the full spectral function was restricted to a small system size $L = 12$ in order to ensure high-quality data and a reliable analytic continuation with the maximum entropy method, a finite-size scaling of the spectral weight at the Fermi level is required. The analytic continuation can be avoided by considering only the spectral function at the Fermi energy, $A(k, 0)$, which can be obtained from the relation

$$A(k, 0) = \frac{1}{2} \lim_{\beta \rightarrow \infty} \beta G(k, \beta/2). \quad (5.8)$$

Because the spectrum of a finite, gapless system has a δ -peak at the Fermi level, we expect $\beta G(k_F, \beta/2)$ to diverge in the limit $\beta \rightarrow \infty$ ($T \rightarrow 0$). In contrast, for a gapped system, this quantity should approach zero.

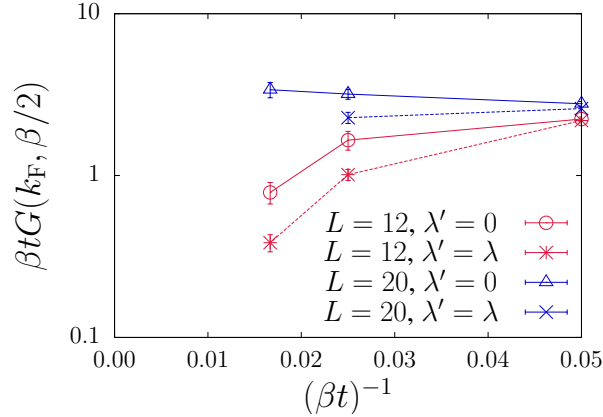


Figure 5.6: Rescaled single-particle Green function at $k = k_F = \pi$ and $\tau = \beta/2$ from CT-INT simulations of the effective model (5.1). Here, $\lambda/t = 0.2$, and $U/t = 6$. Figure adapted from [A9].

Results for $\beta G(k_F, \beta/2)$ as a function of βt are shown in figure 5.6. For $L = 12$, the results are indeed consistent with the gaps observed in the spectra in figure 5.5 (the spectral weight is smaller for nonzero Rashba coupling). However, for a larger system size $L = 20$, the data for $\lambda' = 0$ suggest the absence of a gap, as expected for the case without umklapp scattering. For $\lambda' \neq 0$, the spectral weight is much larger for $L = 20$ than for $L = 12$, but the slight decrease with increasing βt is compatible with a Mott gap at $T = 0$.

The numerical results are reconciled with theoretical expectations as follows. In the absence of Rashba coupling, the bosonisation predicts an increasingly slow decay of transverse correlations with increasing U but no long-range order even at $T = 0$. However, a decay slower than $1/x$ is hard to discern numerically from long-range order. For small system sizes and low temperatures, the length scale of spin-wave fluctuations exceeds L , and the system appears to be in an ordered Mott state, reminiscent of the gapped and ordered state observed for any $U > 0$ in mean-field theory. However, once the fluctuation length scales become smaller than the system size (as achieved by either increasing L or T), the expected gapless edge states become visible, albeit with slowly decaying spin correlations and a suppression of spectral weight at the Fermi level [A2]. For nonzero Rashba coupling λ' , a Mott state with Ising magnetic order is expected for $K < 1/2$ at $T = 0$. However, the additional effects of umklapp scattering seem to be masked to a large extent by the quasi-long-range order driven by forward scattering and already present for $\lambda' = 0$. For example, the spin correlations in figure 5.4(b) are almost identical for $\lambda' = 0$ and $\lambda' \neq 0$, and the gap in figure 5.5 is only slightly larger for $\lambda' \neq 0$. Similar to the spin-wave fluctuations that destroy the mean-field order, the thermal fluctuations (domain walls) that destroy the Ising order at $T > 0$ can have length scales beyond the numerically accessible system sizes. In contrast to the bulk magnetic transition studied in chapter 4, and to Ising quantum phase transitions in one dimension, the Mott transition in helical liquids is hence much more difficult to pin down numerically.

6 Topological Mott insulators

In chapters 4 and 5 we considered the impact of electronic interactions on the topological insulator phase of the Kane-Mele model. As discussed in chapter 2, this phase arises from spin-orbit coupling in a noninteracting Hamiltonian and can be fully understood in terms of topological band theory. The correlated topological insulator is adiabatically connected to the noninteracting limit, and persists up to $U_c(\lambda) > 0$. Dramatic changes in the form of quantum phase transitions only take place at strong coupling.¹ In this chapter, we explore the fascinating possibility of topological insulators that are dynamically generated from electron-electron interactions via symmetry breaking. Such a mechanism, which would lift the requirement of strong intrinsic spin-orbit coupling, was first demonstrated for interacting electrons on the honeycomb lattice [44]. Dynamically generated spin-orbit coupling from interactions had previously been discussed in [271]. These findings inspired a search for similar phases in other settings. At least at the mean-field level, interaction-generated topological insulators or *topological Mott insulators*² exist in a variety of other models, including interacting electrons on π -flux [273], checkerboard [274], Kagomé [275, 276], and decorated honeycomb lattices [276], as well as in three dimensions [277]. Possible experimental realisations of this idea include transition-metal oxide heterostructures [61], pyrochlore iridate thin films [59], and honeycomb superlattices [278]. Fractional interaction-generated Chern insulators have also been predicted [277].

The mean-field predictions of topological Mott insulators have spurred investigations of the impact of quantum fluctuations and competing orders. Most of these activities focussed on the simplest case, spinless fermions on the honeycomb lattice with extended interactions [equation (2.20) with $t_2 = 0$ combined with equation (2.31)]. For the latter, mean-field theory predicts a Chern insulator or integer quantum Hall phase arising from an interaction-generated complex bond order parameter $\langle c_i^\dagger c_j \rangle = \chi_{ij} = \chi_{ji}^* = \pm i|\chi|$ that exactly mimics the t_2 -term of the Haldane model (2.20) with $\phi_{ij} = \pm\pi/2$ and $t_2 = |\chi|$ [44], see figure 6.2(a). Therefore, the mean-field topological Mott insulator is adiabatically connected to the Chern insulator phase of the Haldane model. The corresponding field-theory order parameter, $\langle \bar{\Psi} \gamma^{35} \Psi \rangle$, breaks time-reversal symmetry but preserves chiral symmetry [25, 81] [80, 81].³ Importantly, in addition to the nonzero Chern number, quantised Hall conductance, and chiral edge states (see chapter 2), it has an order parameter χ_{ij} . While similar physics can also arise from the spontaneous ordering of spins [60–63] or complex orbitals [60–63], we focus on the simplest case of Haldane-type bond order.

¹The interacting edge Luttinger liquid is in principle orthogonal to the noninteracting Fermi liquid but, for example, the spin correlation functions evolve continuously with the Luttinger parameter K (see chapter 5).

²While other definitions are in use in the literature [272], we follow [44] and define a topological Mott insulator as an insulating state with an interaction-generated bulk gap and protected gapless edge states.

³In the spinless case considered here, the field Ψ has four components corresponding to the sublattice and pseudospin degrees of freedom, see discussion before equation (2.12).

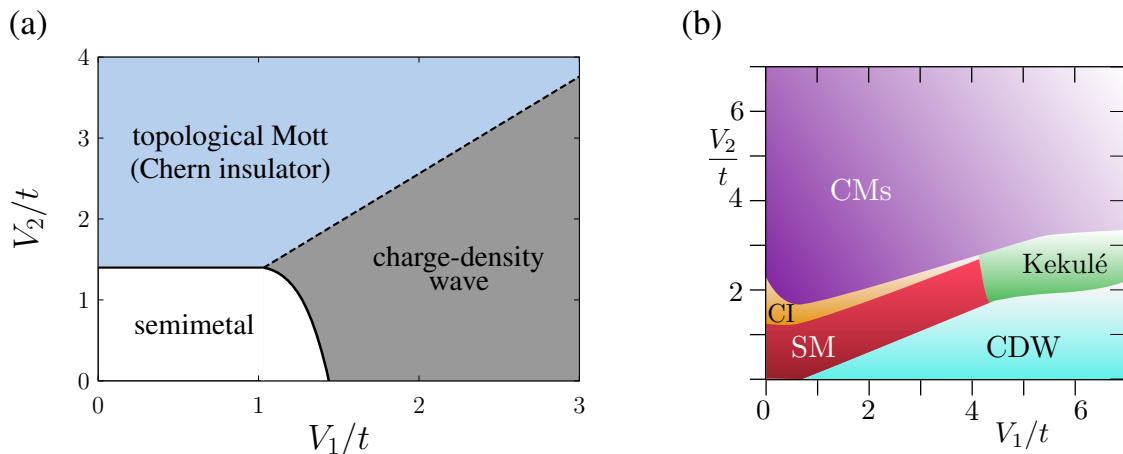


Figure 6.1: Phase diagrams of the spinless-fermion honeycomb model with interactions V_1 and V_2 . (a) Mean-field phase diagram based on the results of [44]. The solid (dashed) line indicates a second (first) order transition. (b) Improved mean-field phase diagram taken from [279], including semimetallic (SM), charge-density-wave (CDW), Chern insulator (CI), charge-modulated (CMs), and Kekulé phases.

Mean-field phase diagrams for spinless fermions on the honeycomb lattice are shown in figure 6.1. As in the spinful case (see chapter 4), the semimetal is stable at weak coupling [81]. Strong nearest-neighbour repulsion V_1 favours a charge-density-wave phase with broken inversion symmetry. This phase is the spinless analogue of the charge-density wave illustrated in figure 4.3(b), and is adiabatically connected to the ground state of noninteracting spinless Dirac fermions with a staggered potential [2], see discussion in chapter 2. It is characterised by a charge imbalance $\langle \hat{n}_A \rangle - \langle \hat{n}_B \rangle \neq 0$ between sublattices; the corresponding order parameter $\langle \bar{\Psi} \Psi \rangle$ breaks chiral symmetry but preserves time-reversal symmetry [81]. The interaction-driven semimetal to charge-density-wave transition has recently become accessible to exact quantum Monte Carlo simulations [167, 175, 280, 281], allowing for a confirmation of the expected Gross-Neveu-Ising universality [81, 180].

Within a two-site mean-field theory [44], a large V_2 gives rise to the Chern insulator phase, see figure 6.1(a). More complex mean-field treatments with larger unit cells and additional order parameters [273, 282] yield a richer phase diagram, see figure 6.1(b). Most importantly for the present discussion, these results suggest that the topological Mott phase is only stable at intermediate V_2 , whereas a charge-modulated phase is favoured at strong coupling [282]. Additionally, the phase diagram contains a Kekulé-ordered⁴ region for $V_1 \sim V_2$ [273, 282] whose existence was confirmed in recent numerical work [279, 286, 287]. The competition of different ordered phases plays a significant role for the selection of the ground state in this problem. While the charge-density-wave, Chern-insulator and Kekulé phases were previously expected based on field-theory arguments [81], the charge-modulated phase was first discussed in [282].

For spinful fermions, interaction-generated quantum spin Hall phases (adiabatically connec-

⁴Kekulé order is a two-dimensional analogue of the Peierls dimerisation [283]. It breaks translation symmetry, and in Dirac systems supports topological zero modes associated with defects in the order parameter [284, 285].

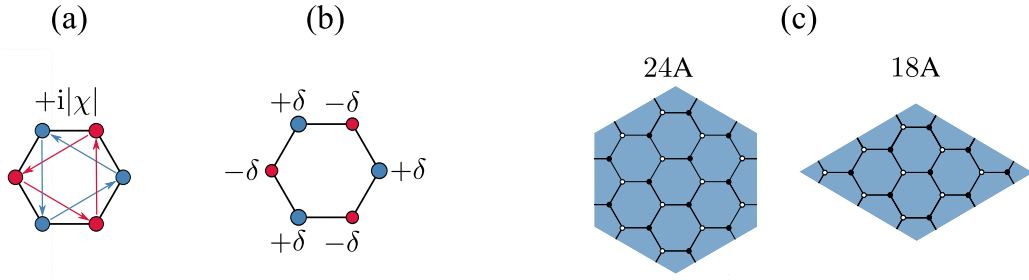


Figure 6.2: (a) Bond order in the mean-field topological Mott phase, showing the directed hops with magnitude $\chi_{ij} = +i|\chi|$. For the opposite direction, $\chi_{ji} = -i|\chi|$. (b) Deviations $\pm\delta$ from the average charge $1/2$ in the charge-density-wave phase. The symbol size indicates the charge density. (c) The main clusters used to obtain the exact diagonalisation results.

ted to the ground state of the noninteracting Kane-Mele model) arise [44]. The latter have a bond order parameter $\langle \bar{\Psi} \mathbf{s}_y^{35} \Psi \rangle$ with opposite sign for spin-up and spin-down electrons and preserve time-reversal symmetry [44, 79, 80]. Other phases in the spinful case include the spin- and charge-density-wave phases discussed in chapter 4 [44]. While the dominant non-local interactions required for a topological Mott state on the honeycomb lattice [$V_2 > V_1$ in figure 6.1(a)] appear to be difficult to realise experimentally, the phase was also observed for more realistic interactions on lattices with larger unit cells [61].

Quantum fluctuations may play a crucial role due to the low coordination number and the competition between different order parameters. Their impact has been investigated using nonperturbative field theory [81, 180] and the functional renormalisation group method on the one hand [44, 288], and numerical methods such as exact diagonalisation [A5, 279, 286, 287], the density-matrix renormalisation group [289], and quantum Monte Carlo [153] on the other hand. As discussed in more detail below, several of these works (including the case of the π -flux model [290, 291]) challenge the existence of a topological Mott phase. Numerical evidence for a stable interaction-generated topological insulator has been given for models with a quadratic band crossing point [292, 293]. In contrast to Dirac systems, the latter have a nonzero density of states at the Fermi level that permits weak-coupling instabilities [274]. For the honeycomb lattice, the full phase diagram as a function of V_1 and V_2 based on exact diagonalisation and density-matrix renormalisation group results contains further charge-ordered phases not previously seen in mean-field theory [287, 289]. Despite the recent development of quantum Monte Carlo methods for fermions with nonlocal interactions [A7, 167, 175, 280, 281] (see also chapter 4), the parameter regimes of the topological Mott and charge-modulated phases remain inaccessible due to the sign problem [153].

We first discuss numerical results regarding the stability of the mean-field topological Mott insulator (section 6.1) which suggest that such a phase is absent if quantum fluctuations are taken into account. Instead, strong repulsions V_2 favour the charge-modulated phase. The transition between the semimetal and the charge-modulated phase, as well as the properties of the latter will be discussed in section 6.2. To restrict the parameter space, we focus on the case $V_1 = 0, V_2 > 0$ [cf. equation (2.31)], which provides the most favourable setting for the topo-

6.1. Existence of a topological Mott insulator

logical Mott insulator [44]. We only considered honeycomb lattices with periodic boundaries. While the topological Mott phase has ordering wavevector $Q = 0$ and hence fits on any cluster, the charge-modulated phase has a six-site unit cell [see figure 6.2(b)]. Moreover, the cluster geometry should be chosen such that the allowed wavevectors include the Dirac points. Most results were obtained for the clusters 24A and 18A in [229] illustrated in figure 6.2(c). A more detailed discussion of the impact of the cluster geometry can be found in [287].

6.1 Existence of a topological Mott insulator

Even restricting our attention to the simple spinless-fermion model on the honeycomb lattice, the question of the stability of the mean-field quantum spin Hall phase has turned out to be a remarkably rich problem. Here, we discuss results from exact diagonalisation and cluster perturbation theory [A5].

In the thermodynamic limit, the topological Mott insulator spontaneously breaks time-reversal symmetry. Numerically, symmetry breaking is absent in finite-size simulations, but can be captured with the infinite-size DMRG method [289]. Using exact diagonalisation as in [A5], a potential Chern-insulating phase would appear as a superposition of the two possible ground states with reversed circulating currents related by time reversal. Therefore, a calculation of the Chern number is expected to give zero, and the topological Mott state has to be detected by other means. A finite-size scaling of bond-bond (or current-current) correlations is complicated by the relatively small system sizes and the influence of cluster geometry [287]. Other possible diagnostics include the ground-state degeneracy, level crossings, and energy spectra. In the following, we present two key arguments for the absence of a topological phase [A5].

In mean-field theory [44], the topological Mott phase is equivalent to the Chern insulator phase of the Haldane model (2.20). Therefore, it is possible to adiabatically connect the non-interacting ground state of the Haldane model and the interaction-generated Chern insulator. Such a connection can be achieved by defining the Hamiltonian

$$\hat{H}(t_2, V_2) = \hat{H}_H(t_2) + \hat{H}_{V_1 V_2}(V_1 = 0, V_2), \quad (6.1)$$

where $\hat{H}_H(t_2)$ is the noninteracting Haldane Hamiltonian (2.20), and $\hat{H}_{V_1 V_2}(V_1 = 0, V_2)$ is the interaction term (2.31) with $V_1 = 0$. We explicitly set $\phi_{ij} = \pm\pi/2$ in $\hat{H}_H(t_2)$, the value found for the mean-field ground state [44]. Upon variation of t_2 and V_2 , $\hat{H}(t_2, V_2)$ interpolates between the Haldane model [86] ($t_2 > 0, V_2 = 0$) and the spinless-fermion model of [44] ($t_2 = 0, V_2 > 0$).

At the mean-field level, the Chern-insulator ground state of $\hat{H}(0, V_2)$ is adiabatically connected to the Chern phase of $\hat{H}(t_2, 0) = \hat{H}_H$. In the simpler mean-field theory of [44], the topological Mott phase exists for any $V_2/t \gtrsim 1.4$, see figure 6.1(a). Mean-field theory with a larger unit cell gives a semimetal for $V_2/t \lesssim 1.6$, a topological Mott state for $1.6 \lesssim V_2/t \lesssim 2.4$, and a charge-modulated phase for $V_2/t \gtrsim 2.4$ [282], see figure 6.1(b). Nevertheless, an adiabatic connection persists for suitable paths in the parameter space spanned by t_2 and V_2 .

Turning now to the full quantum problem, we expect an adiabatic connection between the noninteracting Haldane model $\hat{H}(t_2, 0)$ and the spinless-fermion honeycomb model $\hat{H}(0, V_2)$ if the topological Mott insulator exists. In particular, switching on t_2 should act as a symmetry

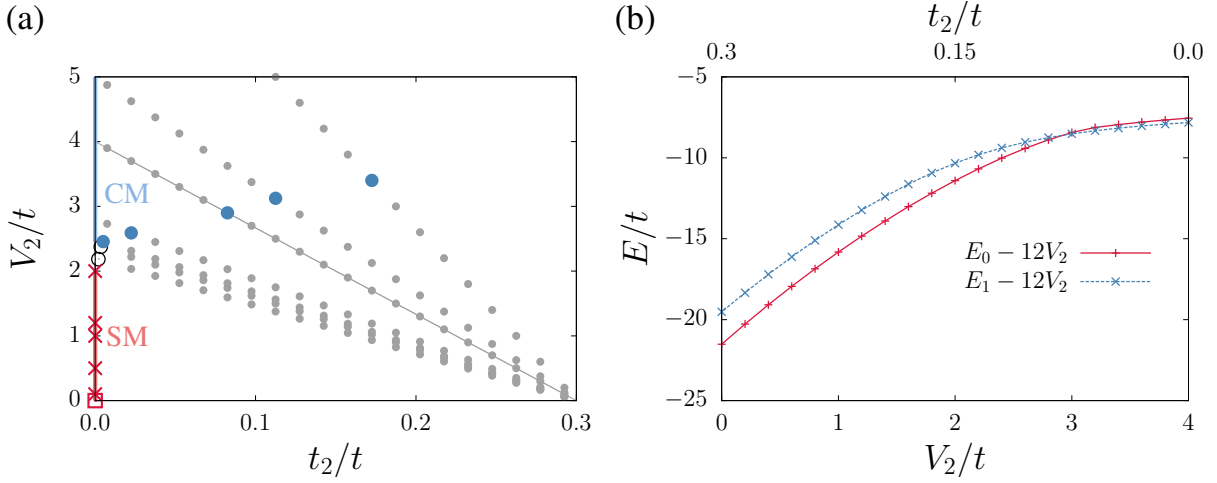


Figure 6.3: (a) Different paths in the parameter space of $\hat{H}(t_2, V_2)$ [equation (6.1)] connecting the Haldane model ($t_2/t = 0.3, V_2 = 0$, bottom right) and the spinless-fermion honeycomb model ($t_2 = 0$). Filled grey symbols indicate the parameter sets considered. Solid blue and open black symbols indicate level crossings where the fidelity $F = 0$, while red symbols correspond to points where F changes significantly. For the meaning of the different symbol types see the text. SM (CM) indicates the semimetallic (charge-modulated) phase. (b) The lowest two energy levels along the path indicated by the solid grey line in (a). Results are for the 24A cluster shown in figure 6.2(c). Figure adapted from [A5].

breaking field and select one of the two degenerate topological ground states potentially generated by V_2 . If a topological phase exists, it should be reinforced by the additional Haldane hopping t_2 . To verify if this scenario is indeed realised, we considered the quantum fidelity

$$F = \langle \Phi_0(t_2, V_2) | \Phi_0(t_2 + \Delta t_2, V_2 + \Delta V_2) \rangle, \quad (6.2)$$

which measures the overlap between ground states of $\hat{H}(t_2, V_2)$ for slightly different values of the parameters t_2 and V_2 . It represents an unbiased diagnostic to detect transitions between different phases without assuming a specific order parameter [294, 295], and is particularly suitable for transitions between phases with different topological invariants⁵ since the latter involve a level crossing even on finite systems [229, 230].

Figure 6.3(a) shows exact diagonalisation results for the fidelity obtained on the 24A cluster. The grey symbols indicate points in parameter space (t_2, V_2) for which $\hat{H}(t_2, V_2)$ was solved. The point on the bottom right corresponds to the Haldane model with $t_2/t = 0.3$ and $V_2 = 0$, while the points on the ordinate correspond to the spinless-fermion honeycomb model with $t_2 = 0$ and repulsion V_2 . The red and blue symbols indicate quantum phase transitions, as indicated either by a level crossing (where $F \rightarrow 0$) or a substantial change of the fidelity.

Let us first consider paths in parameter space that connect the Haldane model to the spinless-fermion honeycomb model with a $V_2/t > 2.5$, for which the charge-modulated phase is expected [282]. The first four paths starting from the top of figure 6.3(a) fulfil this condition. Upon increasing V_2 and decreasing t_2 along the paths indicated, we initially observe that the gapped

⁵More precisely, between phases whose Chern numbers differ by an odd number.

6.1. Existence of a topological Mott insulator

topological phase of the Haldane model is stable with respect to small V_2 . Further along these parameter paths we encounter a level crossing (solid blue symbol) that indicates a transition to a topologically trivial ground state. We will show below that this nontopological phase is the charge-modulated phase, in accordance with mean-field theory. The level crossing is shown in figure 6.3(b) for a final value $V_2/t = 3$ [the path indicated by the grey line in figure 6.3(a)]. E_0 is the ground-state energy for small V_2/t where the system is in the topological phase. E_1 is the energy of the first excited state for small V_2/t , but becomes the lowest energy level for large V_2/t corresponding to the charge-modulated phase. Level crossings are also observed for paths with a smaller final V_2 , for which the critical point moves to smaller values of t_2 . For final values V_2/t in the interval $[2, 2.5]$, a transition (level crossing) at small but finite t_2 remains (open symbols), but the latter involves a change of the ground-state momentum sector. We have verified that this is a cluster-dependent feature which is absent, e.g., on the 18A and 30A clusters. Finally, for $V_2/t \lesssim 2$, we find that the overlap of $|\Phi_0(t_2, V_2)\rangle$ and $|\Phi_0(0, V_2)\rangle$ (i.e., the fidelity F) is significantly smaller than 1 for any $t_2 > 0$.⁶ This implies that the ground state for $t_2 = 0$ is the semimetal which undergoes a transition to the topological phase of the Haldane model at $t_2 = 0^+$ (red symbols), similar to the noninteracting Haldane model (see chapter 2).

Our results for the fidelity reveal that there exists no adiabatic connection between the ground states of $\hat{H}(t_2 = 0, V_2)$ and $\hat{H}(t_2, V_2 = 0)$ for any value of V_2 . This strongly suggests that the topological Mott insulator found in mean-field theory is not stable when quantum fluctuations are taken into account. The importance of fluctuations can be further substantiated by systematically adding them to the mean-field solution. This can be done using a variation of cluster perturbation theory [296, 297]. This method treats hopping and interactions within a finite cluster of N_c sites exactly in terms of an exact calculation of the single-particle Green function. Interactions beyond the cluster can be decoupled by a mean-field approximation [298]. Here, the next-nearest-neighbour repulsion was decoupled as

$$\hat{n}_i \hat{n}_j \mapsto \langle \hat{n}_i \rangle \hat{n}_j + \hat{n}_i \langle \hat{n}_j \rangle - \langle \hat{n}_i \rangle \langle \hat{n}_j \rangle - \langle c_i^\dagger c_j \rangle c_j^\dagger c_i - c_i^\dagger c_j \langle c_j^\dagger c_i \rangle + |c_i^\dagger c_j|^2, \quad (6.3)$$

and only the imaginary bond-order terms $\chi_{ij} = \langle c_i^\dagger c_j \rangle = \pm i|\chi|$ relevant for the topological Mott phase were kept. Within cluster perturbation theory, the decoupled interactions together with hopping processes beyond the cluster are treated in first-order perturbation theory. This approach becomes exact in the noninteracting case, and also for an infinitely large cluster [296]. As a function of cluster size N_c , the results systematically approach the exact results for the thermodynamic limit.

For a two-site cluster, all V_2 interaction terms are treated at the mean-field level, and the resulting cluster perturbation theory is equivalent to the mean-field theory of [44] with vanishing charge order parameter. Accordingly, the ground-state energy in figure 6.4(a) for $N_c = 2$ exhibits a clear minimum at a nonzero value of χ , corresponding to a stable topological Mott phase. For larger N_c , we treat some of the interaction terms exactly [see inset of figure 6.4(a)], and thereby include quantum fluctuations. Crucially, the energy minimum quickly moves from $\chi > 0$ to $\chi = 0$ with increasing cluster size, and the topological ground state is destroyed by fluctuations already for $N_c = 6$.

⁶We find $F = 1/\sqrt{2} \approx 0.7$ for $V_2 > 0$ and $F \approx 0.45$ for $V_2 = 0$.

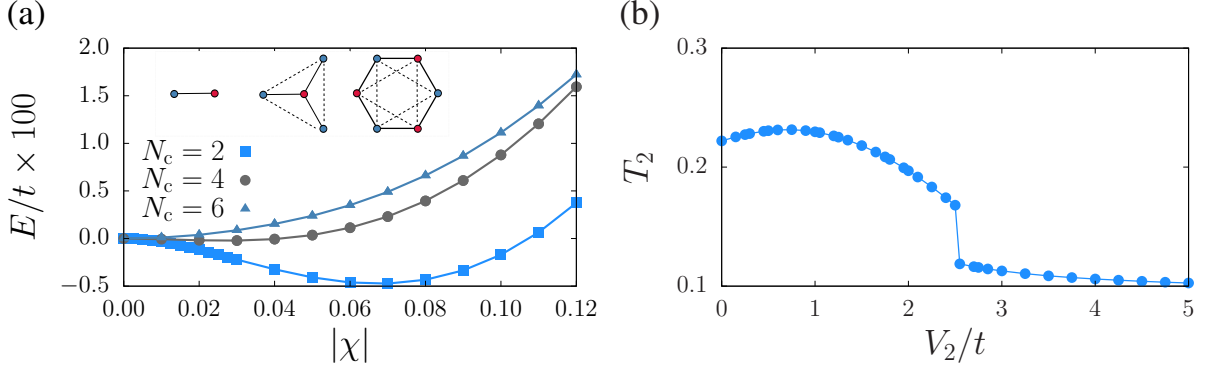


Figure 6.4: (a) Rescaled ground-state energy from cluster perturbation theory for different cluster sizes N_c . Here, $V_2/t = 2$. The inset shows the clusters used, with dashed lines indicating interaction terms that were treated exactly. (b) Bond susceptibility T_2 [equation (6.4)] for $\hat{H}(t_2, V_2)$ with $t_2/t = 0.01$ from exact diagonalisation using the 24A cluster. Figure adapted from [A5].

Although we did not find a stable interaction-generated topological phase, the bond-bond correlation function (calculated with $\phi_{ij} = \pm\pi/2$ and a small symmetry-breaking $t_2 = 0.01t$)

$$T_2 = \frac{1}{L^2} \left\langle \left[\sum_{\langle\langle i,j \rangle\rangle} (e^{i\phi_{ij}} c_i^\dagger c_j + e^{-i\phi_{ij}} c_j^\dagger c_i) \right]^2 \right\rangle \quad (6.4)$$

is initially enhanced by switching on V_2 [figure 6.4(b)]. This tendency toward the formation of complex bond order provides an explanation for the existence of the topological phase in mean-field theory. However, because the semimetal is stable at weak coupling, no phase transition takes place at small V_2 , whereas the charge-modulated phase dominates and T_2 is suppressed at larger V_2 . A weak-coupling topological Mott phase has been reported for models with a quadratic band crossing point [292, 293].

The absence of the interaction-generated topological phase on the honeycomb lattice has been confirmed by several other investigations. The absence of a doubly-degenerate ground state (expected due to the two possible bond-order patterns related by time-reversal) was shown in [279]. A finite-size scaling of the bond order parameter on clusters with up to 42 sites [287] reveals that the correlations observed in figure 6.4(b) and in [263] are short-ranged.⁷ These results also agree with the findings of a recent infinite-size density-matrix renormalisation group study [289]. While short-range bond order of the Haldane-type is again observed, the topological Mott state is not a stable ground state, even if the system is initialised in such a configuration [289]. Whereas the mean-field results were supported by earlier functional renormalisation group results in the spinful case [44], it has recently been shown that an improved patching close to the Dirac points yields the opposite conclusion, namely the absence of a topological

⁷The authors of [263] argue that the topological phase may only be observable for suitable clusters and boundary conditions. This seems to contradict the fact that the ordering wavevector is $Q = 0$, and that the Chern insulator phase of the Haldane model is readily visible on small clusters with or without edges [229]. The two level crossings observed as a function of V_2 on an 18-site cluster with open boundaries in [263] are absent on the 32-site cluster [287], similar to the discussion of figure 6.3(a) above.

6.2. Charge-modulated phase

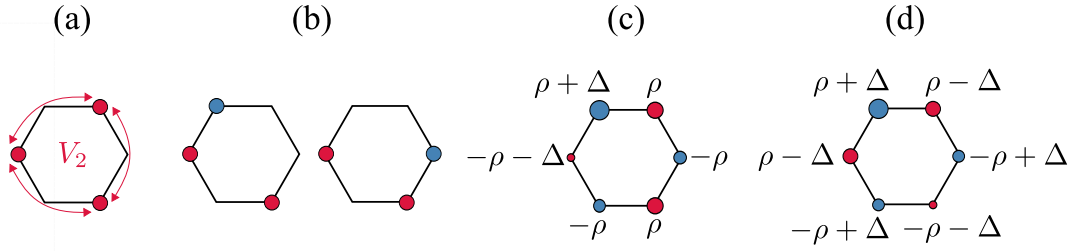


Figure 6.5: (a) Charge-density wave in the classical limit with maximal next-nearest-neighbour energy. (b) Degenerate configurations with one charge moved to the other sublattice. (c) Charge modulation suggested by mean-field theory [282]. (d) Charge modulation found numerically in [289]. The symbol size in (c) and (d) indicates the charge density.

Mott phase in the spinless model in the coupling range where the method is reliable [288]. Similarly, improved functional-renormalisation-group results for the spinful case find no stable topological Mott phase, although enhanced bond correlations were observed [185, 186]. Instead, the ground state for dominant V_2 is a spinful analogue of the charge-modulated phase [185, 186].

6.2 Charge-modulated phase

While the perhaps most interesting phase predicted for the spinless-fermion honeycomb model—the topological Mott insulator—appears to be absent, large values of V_2 instead give rise to a novel charge-ordered phase [282]. As first shown in mean-field theory [282], it has a six-site unit cell and an associated dominant ordering wavevector $\mathbf{Q} = \pm\mathbf{K}$. The charge order in the charge-modulated phase is different from that in the charge-density-wave phase illustrated in figure 6.2(b). In the classical limit $t = 0$, the energy penalty due to V_1 is minimised by configurations with all charges on one sublattice, see figure 6.5(a). However, such a charge-density wave maximises the interaction energy due to V_2 . Setting $V_1 = 0$, the energy is minimised by moving one of the charges to the other sublattice, leading to configurations as shown in figure 6.5(b). For $t = V_1 = 0$, the system decouples into two triangular lattices with repulsion V_2 , corresponding to a frustrated Ising model [287]. The classical ground state is highly degenerate [A5, 279, 287]; in addition to the possible charge configurations on a given sublattice, degeneracies also arise from the various ways of distributing the charges among the two sublattices [A5].

Although the enormous degeneracy is lifted by the hopping t (i.e., quantum fluctuations), a charge modulation remains. Two possible charge patterns are shown in figures 6.5(c) and 6.5(d), parameterised in terms of the deviations ($0 < \Delta < \rho < 1/2$) from $\langle \hat{n}_i \rangle = 1/2$. The pattern in figure 6.5(c) was obtained in mean-field theory [282], while the pattern in figure 6.5(d) was recently observed in density-matrix renormalisation group calculations [289]. In contrast to the charge-density wave with a modulation between sublattices, the charge-modulated phase also exhibits charge modulation within each sublattice. The phase has also been observed in functional renormalisation group studies of honeycomb models [288, 299, 300].

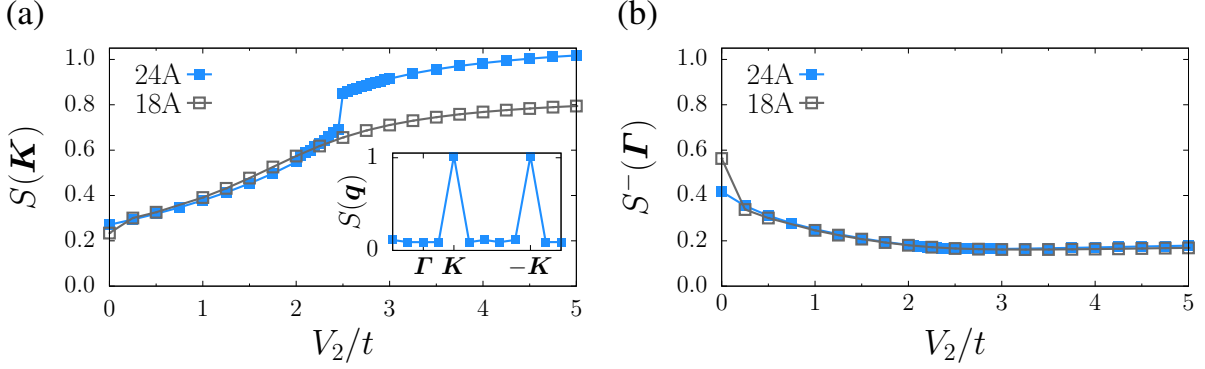


Figure 6.6: (a) Charge structure factor $S(\mathbf{K})$ [equation (6.5)]. The inset shows $S(\mathbf{q})$ for different momenta \mathbf{q} at a fixed $V_2/t = 5$ in the charge-modulated phase. (b) Charge structure factor $S^-(\Gamma)$ [equation (6.6)]. Here, $t_2 = V_1 = 0$. Results obtained by exact diagonalisation. Figure adapted from [A5].

Here, we tracked the onset of charge modulation by calculating the structure factor

$$S(\mathbf{q}) = \frac{1}{2} [S^+(\mathbf{q}) + S^-(\mathbf{q})] \quad (6.5)$$

with

$$S^\pm(\mathbf{q}) = \frac{1}{N} \sum_{ij} e^{-i\mathbf{q} \cdot (\mathbf{r}_i - \mathbf{r}_j)} \langle [(\hat{n}_i^A - \frac{1}{2}) \pm (\hat{n}_i^B - \frac{1}{2})] [(\hat{n}_j^A - \frac{1}{2}) \pm (\hat{n}_j^B - \frac{1}{2})] \rangle. \quad (6.6)$$

Figure 6.6(a) shows results as a function of V_2 for the 18A and 24A clusters. Starting from the semimetallic phase, we observe a continuous increase of $S(\mathbf{q})$ for $\mathbf{q} = \pm\mathbf{K}$, as expected for the charge-modulated phase. The 24A cluster exhibits a jump in $S(\mathbf{K})$ at intermediate V_2/t related to the aforementioned cluster-specific level crossing. In contrast, a smooth increase is found for the 18A cluster. Although charge order is predominantly described by $\mathbf{q} = \pm\mathbf{K}$ [see inset of figure 6.6(a)], subdominant correlations persist also for other \mathbf{q} , suggesting that the true ground state does not have a unique ordering wavevector but instead retains some of the frustration of the classical limit [A5, 287]. The charge-modulated phase is hence intrinsically fluctuating and partially disordered, as expected for frustrated interactions. In particular, charge-density-wave order [measured by $S^-(\Gamma)$ shown in figure 6.6(b) and identical to $S(\Gamma)$ in the inset of figure 6.6(a)] is suppressed but remains nonzero even for large V_2/t . While in [A5] we concluded that the comparable signals at $\mathbf{q} = \Gamma$ and other $\mathbf{q} \neq \pm\mathbf{K}$ suggest equal charge on the two sublattices, a nonzero $S^-(\Gamma)$ is compatible with the finite charge-imbalance between the sublattices reported in later work [287, 289].⁸

From the results in figure 6.3(a), we estimate the transition from the semimetal to charge-modulated phase to occur in the range $2 \lesssim V_2/t \lesssim 2.5$. A continuous quantum phase transition in the same range has been observed in the thermodynamic limit in terms of the entanglement entropy [289]. Similar estimates were obtained in other numerical studies [279, 287].

Using exact diagonalisation we could also calculate the single-particle density of states, see figure 6.7. The results are consistent with gapless, semimetallic behaviour for $V_2/t \lesssim 2$, and

⁸For the charge modulation in figure 6.5(c) [6.5(d)], the sublattices have equal charge for $\rho = 2\Delta$ [$\rho = 3\Delta$].

6.2. Charge-modulated phase

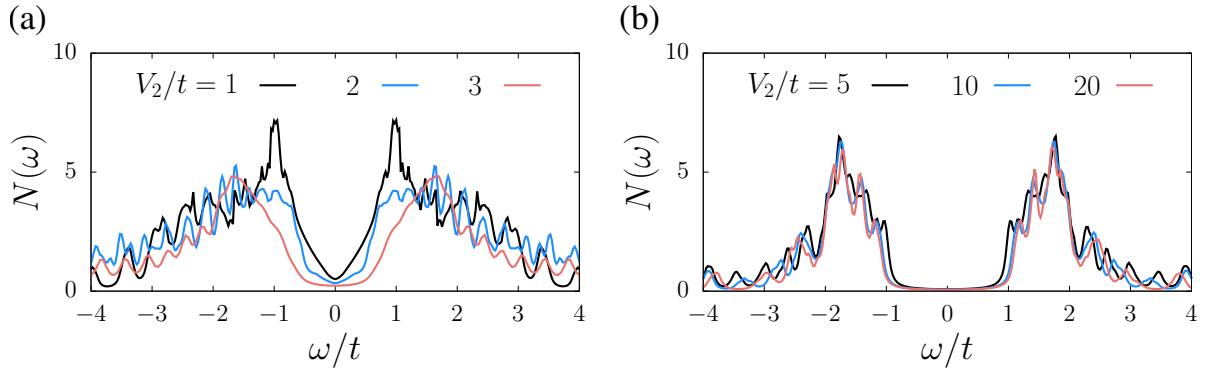


Figure 6.7: Density of states for different values of V_2/t obtained from exact diagonalisation with twisted boundary conditions on the 24A cluster. Here, $t_2 = V_1 = 0$. Figure adapted from [A5].

a gap in the charge-modulated phase at larger V_2/t . As shown in figure 6.7(b), in the strong-coupling regime $V_2/t \gg 1$ where the sublattices essentially decouple, the single-particle gap becomes independent of V_2/t and the gapped low-energy excitations have energy $\omega \sim t$. While the insulating state emerges from the interaction V_2 and is hence a type of Mott insulator, a gap that scales with the bare tight-binding parameter t is typical of band insulators. In the strong-coupling limit, the charge-modulated phase may be regarded as the insulating analogue of pinball liquids [A5]. The latter correspond to systems in which a fraction of the charge carriers is charge-ordered, whereas the remaining particles form a metal [301].

Summary

The role of electron-electron interactions for two-dimensional topological insulators was investigated using numerical methods. The focus was on the following three topics: (i) The impact of correlations on the bulk properties of time-reversal invariant topological insulators, and on the Dirac semimetal as realised in graphene [A1, A3, A4, A7]. (ii) Interaction effects on the helical edge states of topological insulators [A1, A2, A8, A9]. (iii) The possibility of an interaction-generated topological Mott or Chern insulator state [A5] as predicted from mean-field theory [44]. All three problems were defined in terms of fermionic models on the honeycomb lattice either with or without complex hopping terms, and with local and/or nonlocal electron-electron repulsion. In particular, the Kane-Mele model was used, which describes electron hopping and spin-orbit coupling [8, 9]. Topics (i) and (ii) were investigated by auxiliary-field and interaction-expansion quantum Monte Carlo methods, respectively, whereas topic (iii) was studied by means of exact diagonalisation and cluster perturbation theory [296, 297].

(i) Bulk correlation effects were studied in the framework of the Kane-Mele model with additional electron-electron interaction. The Dirac semimetal (for zero spin-orbit coupling) and the topological insulator (for nonzero spin-orbit coupling) of the noninteracting case both remain stable for weak to intermediate electron-electron interactions, but undergo magnetic phase transitions at strong coupling. The resulting antiferromagnetic order is of the Heisenberg type without spin-orbit coupling, and of the easy-plane type with spin-orbit coupling. The universality of the semimetal-Mott insulator transition is modified by the presence of gapless fermionic excitations [180]. Similar to previous results for a Hubbard repulsion [195], the numerical data for a long-range Coulomb repulsion are consistent with the critical exponents of the SU(2) Gross-Neveu class obtained from the ϵ -expansion [79]. In contrast, the magnetic transition at nonzero spin-orbit coupling is purely bosonic, and the data support 3D XY universality. For the topological insulator, a long-range Coulomb interaction gives qualitatively the same results as a local Hubbard repulsion. The critical value for the magnetic transition is larger due to enhanced charge-density-wave fluctuations, but no new phases arise and the universality remains unchanged. The transition from the topological insulator to the antiferromagnet involves the spontaneous breaking of the protecting time-reversal symmetry but no closing of the single-particle gap. The change of the topological invariant at the transition was successfully detected by measuring the response to magnetic π -fluxes, an approach that is valid in the presence of interactions and can be combined with quantum Monte Carlo methods.

(ii) While mean-field theory qualitatively captures bulk interaction effects in topological insulators [82], a description of correlation effects on the quasi-one-dimensional edge states requires a bosonisation approach. However, the latter is only valid at low energies because it neglects the bulk states. Considering the two-dimensional Kane-Mele-Hubbard model with interactions only at the edge, and solving it exactly with the CT-INT quantum Monte Carlo

method, correlated helical edge states were simulated on large lattices. For weak to intermediate interactions (including values larger than the bulk gap), complete agreement with the bosonisation results for the real-space correlation functions was observed. In this regime, Rashba spin-orbit coupling was shown to be an irrelevant perturbation of the Luttinger liquid fixed point. At strong coupling and for a half-filled band, umklapp scattering is expected to be relevant and to give rise to an edge-Mott transition with Ising universality [102, 108]. However, on the accessible system sizes, this transition could not be distinguished from the generic correlation effects. The latter are associated with a mean-field magnetic instability which gives rise to very long length scales for the decay of magnetic correlations that are difficult to distinguish from long-range order numerically.

(iii) A topological Mott insulator—a phase with a bulk gap due to interactions but protected gapless edge states—was first found in a mean-field analysis of fermions on the honeycomb lattice with dominant next-nearest-neighbour repulsion [44]. In the simplest case of spinless fermions, a bond order parameter mimics the complex hopping of the Haldane model [86], giving rise to a Chern insulator state with quantised Hall conductivity. The corresponding spinful model supports an interaction-generated quantum spin Hall phase. In order to assess the role of quantum fluctuations and the competition with other order parameters, the spinless model was studied numerically. The absence of a topological phase from the exact phase diagram was demonstrated by showing that there exists no adiabatic connection between the ground states of the interacting model and the Haldane model. Moreover, the bond order parameter found in mean-field theory is quickly suppressed to zero upon including quantum fluctuations. Instead, the gapped strong-coupling phase is a novel charge-modulated insulator with a six-site unit cell and interesting connections to frustrated systems.

Zusammenfassung

Die Rolle von Elektron-Elektron-Wechselwirkung für zweidimensionale topologische Isolatoren wurde mit Hilfe von numerischen Methoden untersucht. Die Resultate lassen sich folgenden drei Themenkomplexen zuordnen. (i) Den Einfluss von Korrelationen auf das Innere von topologischen Isolatoren mit Zeitumkehrsymmetrie, sowie auf das Dirac-Semimetall wie es experimentell in Graphen realisiert ist [A1, A3, A4, A7]. (ii) Wechselwirkungseffekte im Zusammenhang mit den helikalen Randzuständen von topologischen Isolatoren [A1, A2, A8, A9]. (iii) Topologische Mott-Isolatoren bzw. Chern-Isolatoren deren Existenz basierend auf Molekularfeldnäherungen [44] vorhergesagt wurde [A5]. Alle drei Fragestellungen lassen sich im Rahmen von Modellen für Fermionen auf dem hexagonalen Honigwabengitter definieren, entweder mit oder ohne komplexem Hüpfen sowie mit lokaler oder langreichweitiger Elektron-Elektron-Wechselwirkung. Insbesondere wurde das Kane-Mele-Modell betrachtet, welches elektronisches Hüpfen und Spin-Bahn-Kopplung beschreibt [8, 9]. Die Themen (i) und (ii) wurden mit Hilfe von Quanten-Monte-Carlo-Methoden untersucht, während für Punkt (iii) exakte Diagonalisierung und Cluster-Störungstheorie [296, 297] zum Einsatz kamen.

(i) Bulk-Korrelationseffekte wurden im Rahmen des Kane-Mele-Modells mit zusätzlicher Elektron-Elektron-Wechselwirkung untersucht. Für schwache bis mittlere Wechselwirkungen bleiben die freien Grundzustände – das Dirac-Semimetall im Fall ohne Spin-Bahn-Kopplung und der topologische Isolator im Fall mit Spin-Bahn-Kopplung – stabil. Hingegen verursachen starke Wechselwirkungen magnetische Phasenübergänge zu antiferromagnetischen Phasen. Die magnetische Ordnung ist ohne Spin-Bahn-Kopplung vom Heisenberg-Typ, während sich im Fall mit Spin-Bahn-Kopplung Ordnung in der transversalen Richtung einstellt. Die Kopplung zwischen dem Ordnungsparameter und lückenlosen fermionischen Anregungen ändert die Universalitätsklasse des Übergangs vom Semimetall zum Mott-Isolator [180]. Wie schon zuvor für eine lokale Hubbard-Abstoßung gezeigt [195], sind die numerischen Daten für das Modell mit langreichweitiger Coulomb-Abstoßung in Übereinstimmung mit den Werten der kritischen Exponenten für die SU(2)-Gross-Neveu-Klasse aus der ϵ -Entwicklung [79]. Im Gegensatz dazu fällt der Phasenübergang vom topologischen Isolator zum Antiferromagneten in die erwartete 3D-XY-Universalitätsklasse. Hubbard- und Coulomb-Wechselwirkungen ergeben im Rahmen des Kane-Mele-Modells qualitativ identische Physik. Zwar führen die durch den nichtlokalen Teil der Wechselwirkung verstärkten Ladungsdichtewellenfluktuationen zu deutlich größeren kritischen Werten für den magnetischen Phasenübergang, aber es wurden weder neue Phasen noch anderes kritisches Verhalten gefunden. Der Übergang vom topologischen Isolator zum topologisch trivialen Antiferromagneten erfolgt ohne das Schließen der Einteilchenlücke, aber mit der spontanen Brechung der zugrunde liegenden Zeitumkehrsymmetrie. Die entsprechende Änderung der topologischen Invarianten konnte anhand der Antwort des Systems auf magnetische π -Flüsse im Rahmen von Quanten-Monte-Carlo-Simulationen gezeigt werden.

(ii) Während die Molekularfeldtheorie elektronische Korrelationen im Inneren von topologischen Isolatoren qualitativ richtig erfasst, bedarf es für die analytische Beschreibung von Wechselwirkungseffekten auf die quasi-eindimensionalen Randzustände anderer Methoden. Insbesondere die Bosonisierung lässt aber die Bulk-Zustände bei höheren Energien außer Acht. Stattdessen kann eine Beschreibung dieses Problems im Rahmen des Kane-Mele-Modells mit Hubbard-Wechselwirkung nur am Rand erfolgen, welches mit Hilfe von Quanten-Monte-Carlo-Simulationen numerisch exakt lösbar ist. Insbesondere bietet die Verwendung der CT-INT-Methode die Möglichkeit große Systeme mit oder ohne Rashba-Spin-Bahn-Kopplung zu untersuchen. Für schwache bis mittelstarke Wechselwirkungen wurde vollständige Übereinstimmung zwischen den Korrelationsfunktionen der zweidimensionalen Simulationen und jenen der eindimensionalen Bosonisierung gefunden. Wie erwartet ist die Rashba-Kopplung in diesem Regime irrelevant. Für starke Wechselwirkungen und ein halbgefülltes Band sagt die Bosonisierung einen Mott-Übergang mit Ising-Universalität vorher, welcher durch relevante Umklappstreuung verursacht wird [102, 108]. Allerdings zeigen die Simulationen, dass dieser Übergang numerisch nur schwer von generischen Korrelationseffekten zu unterscheiden ist.

(iii) Topologische Mott-Isolatoren zeichnen sich durch eine Mott-Anregungslücke im Inneren und geschützte metallische Randzustände aus. Ihre Existenz wurde zuerst basierend auf Molekularfeldnäherungen für Modelle von Fermionen auf dem Honigwabengitter vorhergesagt [44]. Im einfachsten Fall von spinlosen Fermionen führt eine dominante Abstoßung zwischen übernächsten Nachbarn zu einem komplexen Bond-Ordnungsparameter der genau dem komplexen Hüpfen des Haldane-Modells [86] entspricht und einen Chern-Isolator mit quantisierter Hall-Leitfähigkeit erzeugt. In einem entsprechenden Modell mit Spin generieren die Wechselwirkungen einen Quanten-Spin-Hall-Grundzustand. Um den Einfluss von Quantenfluktuationen und das Wechselspiel mit anderen Ordnungsparametern zu verstehen, wurde dieses Modell numerisch untersucht. Das Fehlen einer adiabatischen Verbindung zwischen dem wechselwirkenden Modell und dem freien Haldane-Modell zeigt, dass die topologische Phase nicht stabil ist. Entsprechend verschwindet der Bond-Ordnungsparameter sehr schnell wenn Quantenfluktuationen um die Molekularfeldlösung in Betracht gezogen werden. Stattdessen handelt es sich bei der isolierenden Phase, welche durch Wechselwirkungen aus dem Semimetall hervorgeht, um eine neuartige ladungsgeordnete Phase. Diese hat eine Einheitszelle mit sechs Gitterplätzen und weist interessante Verbindungen zu frustrierten System auf.

Bibliography

- [1] M. Hohenadler and F. F. Assaad, *J. Phys.: Condens. Matter* **25** (2013), 143201.
- [2] G. W. Semenoff, *Phys. Rev. Lett.* **53** (1984), 2449.
- [3] K. S. Novoselov et al., *Nature* **438** (2005), 197.
- [4] K. S. Novoselov et al., *Science* **306** (2004), 666.
- [5] A. H. Castro Neto, F. Guinea, N. M. R. Peres, K. S. Novoselov and A. K. Geim, *Rev. Mod. Phys.* **81**, 109 (2009), 109.
- [6] K. S. Novoselov, V. I. C. Fal'ko, P. R. L. Gellert, M. G. Schwab and K. Kim, *Nature* **490** (2012), 192.
- [7] P. R. Wallace, *Phys. Rev.* **71** (1947), 622.
- [8] C. L. Kane and E. J. Mele, *Phys. Rev. Lett.* **95** (2005), 226801.
- [9] C. L. Kane and E. J. Mele, *Phys. Rev. Lett.* **95** (2005), 146802.
- [10] M. König et al., *Science* **318** (2007), 766.
- [11] O. Pankratov, S. Pakhomov and B. Volkov, *Solid State Commun.* **61** (1987), 93.
- [12] B. A. Bernevig, T. L. Hughes and S. Zhang, *Science* **314** (2006), 1757.
- [13] M. Z. Hasan and C. L. Kane, *Rev. Mod. Phys.* **82** (2010), 3045.
- [14] X.-L. Qi and S.-C. Zhang, *Rev. Mod. Phys.* **83** (2011), 1057.
- [15] M. Z. Hasan and J. E. Moore, *Annu. Rev. Cond. Mat. Phys.* **2** (2011), 55.
- [16] E. Fradkin, *Field Theories of Condensed Matter Physics*, Cambridge University Press, 2013.
- [17] B. A. Bernevig, *Topological Insulators and Topological Superconductors*, Princeton University Press, 2013.
- [18] L. Landau, *Zh. Eksp. Teor. Fiz.* **7** (1937), 19.
- [19] K. von Klitzing, G. Dorda and M. Pepper, *Phys. Rev. Lett.* **45** (1980), 494.
- [20] C. Nayak, S. H. Simon, A. Stern, M. Freedman and S. Das Sarma, *Rev. Mod. Phys.* **80** (2008), 1083.
- [21] D. J. Thouless, M. Kohmoto, M. P. Nightingale and M. den Nijs, *Phys. Rev. Lett.* **49** (1982), 405.
- [22] J. E. Avron, R. Seiler and B. Simon, *Phys. Rev. Lett.* **51** (1983), 51.

Bibliography

- [23] M. Kohmoto, *Annals of Physics* **160** (1985), 343.
- [24] B. I. Halperin, *Phys. Rev. B* **25** (1982), 2185.
- [25] F. D. M. Haldane, *Phys. Rev. Lett.* **61** (1988), 2015.
- [26] I. Knez, R.-R. Du and G. Sullivan, *Phys. Rev. Lett.* **107** (2011), 136603.
- [27] A. Roth et al., *Science* **325** (2009), 294.
- [28] C.-C. Liu, W. Feng and Y. Yao, *Phys. Rev. Lett.* **107** (2011), 076802.
- [29] P. Vogt et al., *Phys. Rev. Lett.* **108** (2012), 155501.
- [30] C.-C. Liu, H. Jiang and Y. Yao, *Phys. Rev. B* **84** (2011), 195430.
- [31] F.-f. Zhu et al., *Nat. Mater.* **14** (2015), 1020.
- [32] L. Fu, C. L. Kane and E. J. Mele, *Phys. Rev. Lett.* **98** (2007), 106803.
- [33] J. E. Moore and L. Balents, *Phys. Rev. B* **75** (2007), 121306.
- [34] D. Hsieh et al., *Nature* **452** (2008), 970.
- [35] Y. Xia et al., *Nat. Phys.* **5** (2009), 398.
- [36] X.-L. Qi, T. L. Hughes, S. Raghu and S.-C. Zhang, *Phys. Rev. Lett.* **102** (2009), 187001.
- [37] L. Fu, *Phys. Rev. Lett.* **106** (2011), 106802.
- [38] N. H. Lindner, G. Refael and V. Galitski, *Nat. Phys.* **7** (2011), 490.
- [39] X. Chen, Z.-X. Liu and X.-G. Wen, *Phys. Rev. B* **84** (2011), 235141.
- [40] A. P. Schnyder, S. Ryu, A. Furusaki and A. W. W. Ludwig, *Phys. Rev. B* **78** (2008), 195125.
- [41] A. Kitaev, *AIP Conf. Proc.* **1134** (2009), 22.
- [42] N. F. Mott, *Rev. Mod. Phys.* **40** (1968), 677.
- [43] F. Gebhard, *The Mott metal-insulator transition: models and methods*, Springer Verlag, 1997.
- [44] S. Raghu, X. Qi, C. Honerkamp and S. Zhang, *Phys. Rev. Lett.* **100** (2008), 156401.
- [45] P. W. Anderson, *Materials Research Bulletin* **8** (1973), 153.
- [46] L. Balents, *Nature* **464** (2010), 199.
- [47] X. G. Wen, *Phys. Rev. B* **40** (1989), 7387.
- [48] X. Chen, Z.-C. Gu and X.-G. Wen, *Phys. Rev. B* **82** (2010), 155138.
- [49] M. Levin and A. Stern, *Phys. Rev. Lett.* **103** (2009), 196803.
- [50] S. Wolgast, C. Kurdak, K. Sun, J. W. Allen, D.-J. Kim and Z. Fisk, *Phys. Rev. B* **88** (2013), 180405.
- [51] B. J. Kim et al., *Phys. Rev. Lett.* **101** (2008), 076402.
- [52] B. J. Kim et al., *Science* **323** (2009), 1329.

-
- [53] T. Li et al., Phys. Rev. Lett. **115** (2015), 136804.
- [54] A. Shitade, H. Katsura, J. Kunes, X.-L. Qi, S.-C. Zhang and N. Nagaosa, Phys. Rev. Lett. **102** (2009), 256403.
- [55] C. Weeks, J. Hu, J. Alicea, M. Franz and R. Wu, Phys. Rev. X **1** (2011), 021001.
- [56] K. K. Gomes, W. Mar, W. Ko, F. Guinea and H. C. Manoharan, Nature **483** (2012), 306.
- [57] A. Rüegg and G. A. Fiete, Phys. Rev. Lett. **108** (2012), 046401.
- [58] D. Xiao, W. Zhu, Y. Ran, N. Nagaosa and S. Okamoto, Nat. Commun. **2** (2011), 596.
- [59] X. Hu, A. Rüegg and G. A. Fiete, Phys. Rev. B **86** (2012), 235141.
- [60] K.-Y. Yang, W. Zhu, D. Xiao, S. Okamoto, Z. Wang and Y. Ran, Phys. Rev. B **84** (2011), 201104.
- [61] A. Rüegg and G. A. Fiete, Phys. Rev. B **84** (2011), 201103.
- [62] A. Rüegg, C. Mitra, A. A. Demkov and G. A. Fiete, Phys. Rev. B **85** (2012), 245131.
- [63] F. Wang and Y. Ran, Phys. Rev. B **84** (2011), 241103.
- [64] B. Béri and N. R. Cooper, Phys. Rev. Lett. **107** (2011), 145301.
- [65] N. Goldman et al., Phys. Rev. Lett. **105** (2010), 255302.
- [66] A. Singha et al., Science **332** (2011), 1176.
- [67] L. Tarruell, D. Greif, T. Uehlinger, G. Jotzu and T. Esslinger, Nature **483** (2012), 302.
- [68] L. Balents, Nature **464** (2010), 199.
- [69] K. G. Wilson, Rev. Mod. Phys. **47** (1975), 773.
- [70] C. Wu and S.-C. Zhang, Phys. Rev. B **71** (2005), 155115.
- [71] H. Min, J. E. Hill, N. A. Sinitsyn, B. R. Sahu, L. Kleinman and A. H. MacDonald, Phys. Rev. B **74** (2006), 165310.
- [72] Y. Xu et al., Phys. Rev. Lett. **111** (2013), 136804.
- [73] M. O. Goerbig, Rev. Mod. Phys. **83** (2011), 1193.
- [74] C. Kittel, *Quantum Theory of Solids*, Wiley, 1963.
- [75] N. H. Shon and T. Ando, J. Phys. Soc. Jpn. **67** (1998), 2421.
- [76] R. Winkler and U. Zülicke, ANZIAM J. **57** (2015), 3.
- [77] T. Lancaster and S. J. Blundell, *Quantum Field Theory for the Gifted Amateur*, Oxford University Press, 2014.
- [78] T. W. Appelquist, M. Bowick, D. Karabali and L. C. R. Wijewardhana, Phys. Rev. D **33** (1986), 3704.
- [79] I. F. Herbut, V. Juričić and O. Vafek, Phys. Rev. B **80** (2009), 075432.
- [80] L. Classen, I. F. Herbut, L. Janssen and M. M. Scherer, Phys. Rev. B **93** (2016), 125119.

Bibliography

- [81] I. F. Herbut, V. Juričić and B. Roy, Phys. Rev. B **79** (2009), 085116.
- [82] S. Rachel and K. Le Hur, Phys. Rev. B **82** (2010), 075106.
- [83] J. J. Sakurai, *Modern Quantum Mechanics*, Addison-Wesley, 1994.
- [84] V. Juricic, A. Mesaros, R.-J. Slager and J. Zaanen, Phys. Rev. Lett. **108** (2012), 106403.
- [85] J. C. Budich, B. Trauzettel and G. Sangiovanni, Phys. Rev. B **87** (2013), 235104.
- [86] F. D. M. Haldane, Phys. Rev. Lett. **61** (1988), 1029.
- [87] G. Jotzu et al., Nature **515** (2014), 237.
- [88] A. N. Redlich, Phys. Rev. Lett. **52** (1984), 18.
- [89] J. S. Shiing-Shen Chern, Annals of Mathematics **99** (1974), 48.
- [90] H. Nielsen and M. Ninomiya, Physics Letters B **105** (1981), 219.
- [91] D. Xiao, M.-C. Chang and Q. Niu, Rev. Mod. Phys. **82** (2010), 1959.
- [92] X.-L. Qi, Y.-S. Wu and S.-C. Zhang, Phys. Rev. B **74** (2006), 085308.
- [93] W.-Y. Hsiang and D.-H. Lee, Phys. Rev. A **64** (2001), 052101.
- [94] W. P. Su, J. R. Schrieffer and A. J. Heeger, Phys. Rev. Lett. **42** (1979), 1698.
- [95] R. Jackiw and C. Rebbi, Phys. Rev. D **13** (1976), 3398.
- [96] X. G. Wen, Int. J. Mod. Phys. B **6** (1992), 1711.
- [97] Y. Hatsugai, Phys. Rev. Lett. **71** (1993), 3697.
- [98] D. N. Sheng, Z. Y. Weng, L. Sheng and F. D. M. Haldane, Phys. Rev. Lett. **97** (2006), 036808.
- [99] D. N. Sheng, L. Balents and Z. Wang, Phys. Rev. Lett. **91** (2003), 116802.
- [100] L. Fu and C. L. Kane, Phys. Rev. B **74** (2006), 195312.
- [101] X. Qi, T. L. Hughes and S. Zhang, Phys. Rev. B **78** (2008), 195424.
- [102] C. Wu, B. A. Bernevig and S.-C. Zhang, Phys. Rev. Lett. **96** (2006), 106401.
- [103] D.-H. Lee, Phys. Rev. Lett. **107** (2011), 166806.
- [104] C. Callan and J. Harvey, Nucl. Phys. B **250** (1985), 427.
- [105] X. G. Wen, Phys. Rev. B **43** (1991), 11025.
- [106] L. Fu and C. L. Kane, Phys. Rev. B **76** (2007), 045302.
- [107] Y. A. Bychkov and E. I. Rashba, J. Phys. C: Solid State Phys. **17** (1984), 6039.
- [108] C. Xu and J. E. Moore, Phys. Rev. B **73** (2006), 045322.
- [109] C. L. Kane and M. P. A. Fisher, Phys. Rev. Lett. **68** (1992), 1220.
- [110] M. Onoda, Y. Avishai and N. Nagaosa, Phys. Rev. Lett. **98** (2007), 076802.
- [111] J. Hubbard, Proc. R. Soc. London **276** (1963), 238.

-
- [112] J. González, F. Guinea and M. A. H. Vozmediano, Nucl. Phys. B **424** (1994), 595.
- [113] V. N. Kotov, B. Uchoa, V. M. Pereira, F. Guinea and A. H. Castro Neto, Rev. Mod. Phys. **84** (2012), 1067.
- [114] D. P. Landau and K. Binder, *A Guide to Monte Carlo Simulations in Statistical Physics*, Cambridge University Press, 2000.
- [115] J. W. Negele and H. Orland, *Quantum Many-Particle Systems*, Perseus Books, 1998.
- [116] W. von der Linden, Phys. Rep. **220** (1992), 53.
- [117] N. Kawashima and K. Harada, J. Phys. Soc. Jpn. **73** (2004), 1379.
- [118] F. F. Assaad and H. G. Evertz, *Computational Many Particle Physics*, ed. by H. Fehske, R. Schneider and A. Weiße, vol. 739, Lecture Notes in Physics, Springer Verlag, 2008, 277.
- [119] E. Gull, A. J. Millis, A. I. Lichtenstein, A. N. Rubtsov, M. Troyer and P. Werner, Rev. Mod. Phys. **83** (2011), 349.
- [120] L. Pollet, Rep. Prog. Phys. **75** (2012), 094501.
- [121] N. Metropolis, A. W. Rosenbluth, M. N. Rosenbluth, A. H. Teller and E. Teller, J. Chem. Phys. **21** (1953), 1087.
- [122] R. P. Feynman, Phys. Rev. **91** (1953), 1291.
- [123] M. Suzuki, S. Miyashita and A. Kuroda, Prog. Theor. Phys. **58** (1977), 1377.
- [124] J. E. Hirsch, R. L. Sugar, D. J. Scalapino and R. Blankenbecler, Phys. Rev. B **26** (1982), 5033.
- [125] H. G. Evertz, Adv. Phys. **52** (1997), 1.
- [126] R. Blankenbecler, D. J. Scalapino and R. L. Sugar, Phys. Rev. D **24** (1981), 2278.
- [127] A. N. Rubtsov, V. V. Savkin and A. I. Lichtenstein, Phys. Rev. B **72** (2005), 035122.
- [128] H. F. Trotter, Proc. Amer. Math. Soc. **10** (1959), 545.
- [129] M. Suzuki, Phys. Lett. A **113** (1985), 299.
- [130] A. Sandvik and J. Kurkijärvi, Phys. Rev. B **43** (1991), 5950.
- [131] H. G. Evertz, G. Lana and M. Marcu, Phys. Rev. Lett. **70** (1993), 875.
- [132] B. B. Beard and U.-J. Wiese, Phys. Rev. Lett. **77** (1996), 5130.
- [133] N. V. Prokof'ev, B. V. Svistunov and I. S. Tupitsyn, J. Exp. Theor. Phys. **87** (1998), 310.
- [134] S. M. A. Rombouts, K. Heyde and N. Jachowicz, Phys. Rev. Lett. **82** (1999), 4155.
- [135] P. Werner, A. Comanac, L. D. Medici, M. Troyer and A. J. Millis, Phys. Rev. Lett. **97** (2006), 076405.
- [136] E. Gull, P. Werner, O. Parcollet and M. Troyer, Europhys. Lett. **82** (2008), 57003.
- [137] M. Iazzi and M. Troyer, Phys. Rev. B **91** (2015), 241118.

Bibliography

- [138] L. Wang, M. Iazzi, P. Corboz and M. Troyer, *Phys. Rev. B* **91** (2015), 235151.
- [139] T. Maier, M. Jarrell, T. Pruschke and M. H. Hettler, *Rev. Mod. Phys.* **77** (2005), 1027.
- [140] W. K. Hastings, *Biometrika* **57** (1970), 97.
- [141] E. Y. Loh, J. E. Gubernatis, R. T. Scalettar, S. R. White, D. J. Scalapino and R. L. Sugar, *Phys. Rev. B* **41** (1990), 9301.
- [142] M. Iazzi, A. A. Soluyanov and M. Troyer, *Phys. Rev. B* **93** (2016), 115102.
- [143] M. Troyer and U.-J. Wiese, *Phys. Rev. Lett.* **94** (2005), 170201.
- [144] S. Capponi and F. F. Assaad, *Phys. Rev. B* **63** (2001), 155114.
- [145] R. T. Scalettar, N. E. Bickers and D. J. Scalapino, *Phys. Rev. B* **40** (1989), 197.
- [146] T. Grover, *Phys. Rev. Lett.* **111** (2013), 130402.
- [147] S. R. White, D. J. Scalapino, R. L. Sugar, E. Y. Loh, J. E. Gubernatis and R. T. Scalettar, *Phys. Rev. B* **40** (1989), 506.
- [148] R. dos Santos, *Braz. J. Phys.* **33** (2003), 36.
- [149] A. Altland and B. D. Simons, *Condensed Matter Field Theory*, Cambridge University Press, 2010.
- [150] J. E. Hirsch, *Phys. Rev. B* **31** (1985), 4403.
- [151] J. E. Hirsch, *Phys. Rev. B* **28** (1983), 4059.
- [152] F. F. Assaad, M. Imada and D. J. Scalapino, *Phys. Rev. B* **56** (1997), 15001.
- [153] M. Golor and S. Wessel, *Phys. Rev. B* **92** (2015), 195154.
- [154] S. Hands and C. Strouthos, *Phys. Rev. B* **78** (2008), 165423.
- [155] J. E. Drut and T. A. Lähde, *Phys. Rev. Lett.* **102** (2009), 026802.
- [156] J. E. Drut and T. A. Lähde, *Phys. Rev. B* **79** (2009), 165425.
- [157] R. M. Fye, *Phys. Rev. B* **33** (1986), 6271.
- [158] W. H. Press, S. A. Teukolsky, W. T. Vetterling and B. P. Flannery, *Numerical Recipes in C*, Cambridge University Press, 1992.
- [159] S. R. White, R. L. Sugar and R. T. Scalettar, *Phys. Rev. B* **38** (1988), 11665.
- [160] J. E. Hirsch, *Phys. Rev. B* **38** (1988), 12023.
- [161] S. Sorella, S. Baroni, R. Car and M. Parrinello, *Europhys. Lett.* **8** (1989), 663.
- [162] M. Feldbacher and F. F. Assaad, *Phys. Rev. B* **63** (2001), 073105.
- [163] G. Sugiyama and S. Koonin, *Annals of Physics* **168** (1986), 1.
- [164] J. E. Hirsch, *Phys. Rev. B* **31** (1985), 4403.
- [165] R. R. P. Singh and R. T. Scalettar, *Phys. Rev. Lett.* **66** (1991), 3203.
- [166] D. Zheng, G.-M. Zhang and C. Wu, *Phys. Rev. B* **84** (2011), 205121.

-
- [167] Z.-X. Li, Y.-F. Jiang and H. Yao, *Phys. Rev. B* **91** (2015), 241117.
- [168] A. Georges, G. Kotliar, W. Krauth and M. J. Rozenberg, *Rev. Mod. Phys.* **68** (1996), 13.
- [169] K. Mielson, A. Macridin and M. Jarrell, *Phys. Rev. E* **79** (2009), 057701.
- [170] J. E. Hirsch and R. M. Fye, *Phys. Rev. Lett.* **56** (1986), 2521.
- [171] M. Hohenadler, F. F. Assaad and H. Fehske, *Phys. Rev. Lett.* **109** (2012), 116407.
- [172] F. F. Assaad and T. C. Lang, *Phys. Rev. B* **76**, 035116 (2007), 035116.
- [173] D. J. Luitz and F. F. Assaad, *Phys. Rev. B* **81** (2010), 024509.
- [174] E. F. Huffman and S. Chandrasekharan, *Phys. Rev. B* **89** (2014), 111101.
- [175] L. Wang, P. Corboz and M. Troyer, *New J. Phys.* **16** (2014), 103008.
- [176] J. González, F. Guinea and M. A. H. Vozmediano, *Phys. Rev. B* **59** (1999), R2474.
- [177] D. C. Elias et al., *Nat. Phys.* **7** (2011), 701.
- [178] R. Shankar, *Rev. Mod. Phys.* **66** (1994), 129.
- [179] S. Sorella and E. Tosatti, *Europhys. Lett.* **19** (1992), 699.
- [180] I. F. Herbut, *Phys. Rev. Lett.* **97** (2006), 146401.
- [181] N. F. Mott, *Proc. Phys. Soc. A* **62** (1949), 416.
- [182] C. Honerkamp, *Phys. Rev. Lett.* **100** (2008), 146404.
- [183] Y. Araki and G. W. Semenoff, *Phys. Rev. B* **86** (2012), 121402.
- [184] L. Classen, I. F. Herbut, L. Janssen and M. M. Scherer, *Phys. Rev. B* **92** (2015), 035429.
- [185] D. Sánchez de la Peña, J. Lichtenstein and C. Honerkamp, *arXiv:1606.01124* (2016).
- [186] Y. Volpez, D. D. Scherer and M. M. Scherer, *arXiv:1606.01125* (2016).
- [187] N. D. Mermin and H. Wagner, *Phys. Rev. Lett.* **17** (1966), 1133.
- [188] K. G. Wilson and J. Kogut, *Phys. Rep.* **12** (1974), 75.
- [189] D. J. Gross and A. Neveu, *Phys. Rev. D* **10** (1974), 3235.
- [190] K. G. Wilson and M. E. Fisher, *Phys. Rev. Lett.* **28** (1972), 240.
- [191] L. Janssen and I. F. Herbut, *Phys. Rev. B* **89** (2014), 205403.
- [192] T. Paiva, R. T. Scalettar, W. Zheng, R. R. P. Singh and J. Oitmaa, *Phys. Rev. B* **72** (2005), 085123.
- [193] Z. Y. Meng, T. C. Lang, S. Wessel, F. F. Assaad and A. Muramatsu, *Nature* **464** (2010), 847.
- [194] S. Sorella, Y. Otsuka and S. Yunoki, *Sci. Rep.* **2** (2012), 992.
- [195] F. F. Assaad and I. F. Herbut, *Phys. Rev. X* **3** (2013), 031010.
- [196] F. P. Toldin, M. Hohenadler, F. F. Assaad and I. F. Herbut, *Phys. Rev. B* **91** (2015), 165108.

Bibliography

- [197] W. Wu, S. Rachel, W.-M. Liu and K. Le Hur, *Phys. Rev. B* **85** (2012), 205102.
- [198] S.-L. Yu, X. C. Xie and J.-X. Li, *Phys. Rev. Lett.* **107** (2011), 010401.
- [199] J. C. Budich, R. Thomale, G. Li, M. Laubach and S.-C. Zhang, *Phys. Rev. B* **86** (2012), 201407.
- [200] F. Grandi, F. Manghi, O. Corradini, C. M. Bertoni and A. Bonini, *New J. Phys.* **17** (2015), 023004.
- [201] M. Laubach, J. Reuther, R. Thomale and S. Rachel, *Phys. Rev. B* **90** (2014), 165136.
- [202] Y. Yamaji and M. Imada, *Phys. Rev. B* **83** (2011), 205122.
- [203] J. Wen, M. Kargarian, A. Vaezi and G. A. Fiete, *Phys. Rev. B* **84** (2011), 235149.
- [204] M. Mardani, M.-S. Vaezi and A. Vaezi, arXiv:1111.5980 (2011).
- [205] A. Medhi, V. B. Shenoy and H. R. Krishnamurthy, *Phys. Rev. B* **85** (2012), 235449.
- [206] A. Vaezi, M. Mashkooari and M. Hosseini, *Phys. Rev. B* **85** (2012), 195126.
- [207] J. Reuther, R. Thomale and S. Rachel, *Phys. Rev. B* **86** (2012), 155127.
- [208] M. Kargarian, A. Langari and G. A. Fiete, *Phys. Rev. B* **86** (2012), 205124.
- [209] C. Griset and C. Xu, *Phys. Rev. B* **85** (2012), 045123.
- [210] H.-H. Hung, L. Wang, Z.-C. Gu and G. A. Fiete, *Phys. Rev. B* **87** (2013), 121113.
- [211] T. C. Lang, A. M. Essin, V. Gurarie and S. Wessel, *Phys. Rev. B* **87** (2013), 205101.
- [212] H.-Q. Wu, Y.-Y. He, Y.-Z. You, C. Xu, Z. Y. Meng and Z.-Y. Lu, *Phys. Rev. B* **92** (2015), 165123.
- [213] Z. Y. Meng, H.-H. Hung and T. C. Lang, *Mod. Phys. Lett. B* **28** (2014), 1430001.
- [214] Y.-Y. He, H.-Q. Wu, Z. Y. Meng and Z.-Y. Lu, *Phys. Rev. B* **93** (2016), 195163.
- [215] Y.-Y. He, H.-Q. Wu, Z. Y. Meng and Z.-Y. Lu, *Phys. Rev. B* **93** (2016), 195164.
- [216] F. F. Assaad, T. C. Lang and F. Parisen Toldin, *Phys. Rev. B* **89** (2014), 125121.
- [217] T. Yoshida, S. Fujimoto and N. Kawakami, *Phys. Rev. B* **85** (2012), 125113.
- [218] S. Miyakoshi and Y. Ohta, *Phys. Rev. B* **87** (2013), 195133.
- [219] D. Cocks, P. P. Orth, S. Rachel, M. Buchhold, K. Le Hur and W. Hofstetter, *Phys. Rev. Lett.* **109** (2012), 205303.
- [220] J. Wu, J. P. L. Faye, D. Sénéchal and J. Maciejko, *Phys. Rev. B* **93** (2016), 075131.
- [221] V. S. Arun, R. Sohal, C. Hickey and A. Paramekanti, *Phys. Rev. B* **93** (2016), 115110.
- [222] W. Zheng, H. Shen, Z. Wang and H. Zhai, *Phys. Rev. B* **91** (2015), 161107.
- [223] C. Hickey, P. Rath and A. Paramekanti, *Phys. Rev. B* **91** (2015), 134414.
- [224] D. Prychynenko and S. D. Huber, *Physica B: Condensed Matter* **481** (2016), 53.
- [225] Z.-L. Gu, K. Li and J.-X. Li, arXiv:1512.05118 (2015).

-
- [226] T. I. Vanhala, T. Siro, L. Liang, M. Troyer, A. Harju and P. Törmä, *Phys. Rev. Lett.* **116** (2016), 225305.
- [227] J. Imriška, L. Wang and M. Troyer, *Phys. Rev. B* **94** (2016), 035109.
- [228] L. Wang, H. Shi, S. Zhang, X. Wang, X. Dai and X. C. Xie, arXiv:1012.5163 (2010).
- [229] C. N. Varney, K. Sun, M. Rigol and V. Galitski, *Phys. Rev. B* **82** (2010), 115125.
- [230] C. N. Varney, K. Sun, M. Rigol and V. Galitski, *Phys. Rev. B* **84** (2011), 241105.
- [231] P. W. Anderson, *Phys. Rev.* **79** (1950), 350.
- [232] V. J. Emery, *Highly conducting one-dimensional solids*, ed. by J. T. Devreese, Plenum Press, 1979, 247.
- [233] V. Gurarie, *Phys. Rev. B* **83** (2011), 085426.
- [234] A. M. Essin and V. Gurarie, *Phys. Rev. B* **84** (2011), 125132.
- [235] Y. Otsuka, S. Yunoki and S. Sorella, *Phys. Rev. X* **6** (2016), 011029.
- [236] H.-Y. Yang, A. M. Läuchli, F. Mila and K. P. Schmidt, *Phys. Rev. Lett.* **105** (2010), 267204.
- [237] G. Fiete, private communication.
- [238] M. E. Fisher, *Rep. Prog. Phys.* **30** (1967), 615.
- [239] B. Widom, *Scholarpedia* **10** (2009), 9054.
- [240] S. Sachdev, *Quantum Phase Transitions*, Cambridge University Press, 2011.
- [241] S. Chandrasekharan and A. Li, *Phys. Rev. D* **88** (2013), 021701.
- [242] B. Roy, V. Juričić and I. F. Herbut, *Phys. Rev. B* **87** (2013), 041401.
- [243] M. Campostrini, M. Hasenbusch, A. Pelissetto, P. Rossi and E. Vicari, *Phys. Rev. B* **63** (2001), 214503.
- [244] M. Campostrini, M. Hasenbusch, A. Pelissetto and E. Vicari, *Phys. Rev. B* **74** (2006), 144506.
- [245] Q. Niu, D. J. Thouless and Y.-S. Wu, *Phys. Rev. B* **31** (1985), 3372.
- [246] Z. Wang and B. Yan, *J. Phys: Condens. Matter* **25** (2013), 155601.
- [247] G. E. Volovik, *The Universe in a Helium Droplet*, Clarendon Press, 2003.
- [248] X.-L. Qi and S.-C. Zhang, *Phys. Rev. Lett.* **101** (2008), 086802.
- [249] Y. Ran, A. Vishwanath and D.-H. Lee, *Phys. Rev. Lett.* **101** (2008), 086801.
- [250] X.-L. Qi, Y.-S. Wu and S.-C. Zhang, *Phys. Rev. B* **74** (2006), 045125.
- [251] D.-H. Lee, G.-M. Zhang and T. Xiang, *Phys. Rev. Lett.* **99** (2007), 196805.
- [252] E. H. Lieb, *Phys. Rev. Lett.* **73** (1994), 2158.
- [253] J. Voit, *Rep. Prog. Phys.* **57** (1995), 977.

Bibliography

- [254] K. Wakabayashi, M. Fujita, H. Ajiki and M. Sigrist, Phys. Rev. B **59** (1999), 8271.
- [255] D. Soriano and J. Fernández-Rossier, Phys. Rev. B **82** (2010), 161302.
- [256] H. Feldner, Z. Y. Meng, T. C. Lang, F. F. Assaad, S. Wessel and A. Honecker, Phys. Rev. Lett. **106** (2011), 226401.
- [257] D. J. Luitz, F. F. Assaad and M. J. Schmidt, Phys. Rev. B **83** (2011), 195432.
- [258] M. J. Schmidt, Phys. Rev. B **86** (2012), 075458.
- [259] M. Fujita, K. Wakabayashi, K. Nakada and K. Kusakabe, J. Phys. Soc. Jpn. **65** (1996), 1920.
- [260] F. Goth, D. J. Luitz and F. F. Assaad, Phys. Rev. B **88** (2013), 075110.
- [261] G. Tkachov and E. M. Hankiewicz, Phys. Status Solidi **250** (2013), 215.
- [262] L. Wang, X. Dai and X. C. Xie, Eur. Phys. Lett. **98** (2012), 57001.
- [263] T. Duric, N. Chancellor and I. F. Herbut, Phys. Rev. B **89** (2014), 165123.
- [264] Y. Tanaka and N. Nagaosa, Phys. Rev. Lett. **103** (2009), 166403.
- [265] Y. Tada, R. Peters, M. Oshikawa, A. Koga, N. Kawakami and S. Fujimoto, Phys. Rev. B **85** (2012), 165138.
- [266] J. Cardy, *Scaling and Renormalization in Statistical Physics*, Cambridge University Press, 1996.
- [267] M. Jarrell and J. E. Gubernatis, Phys. Rep. **269** (1996), 133.
- [268] K. S. D. Beach, arXiv:0403055 (2004).
- [269] A. V. Moroz, K. V. Samokhin and C. H. W. Barnes, Phys. Rev. Lett. **84** (2000), 4164.
- [270] T. L. Schmidt, S. Rachel, F. von Oppen and L. I. Glazman, Phys. Rev. Lett. **108** (2012), 156402.
- [271] C. Wu and S.-C. Zhang, Phys. Rev. Lett. **93** (2004), 036403.
- [272] D. Pesin and L. Balents, Nat. Phys. **6** (2010), 376.
- [273] C. Weeks and M. Franz, Phys. Rev. B **81** (2010), 085105.
- [274] K. Sun, H. Yao, E. Fradkin and S. A. Kivelson, Phys. Rev. Lett. **103** (2009), 046811.
- [275] Q. Liu, H. Yao and T. Ma, Phys. Rev. B **82** (2010), 045102.
- [276] J. Wen, A. Rüegg, C.-C. J. Wang and G. A. Fiete, Phys. Rev. B **82** (2010), 075125.
- [277] Y. Zhang, Y. Ran and A. Vishwanath, Phys. Rev. B **79** (2009), 245331.
- [278] J. W. F. Venderbos, M. Manzardo, D. V. Efremov, J. van den Brink and C. Ortix, Phys. Rev. B **93** (2016), 045428.
- [279] N. A. García-Martínez, A. G. Grushin, T. Neupert, B. Valenzuela and E. V. Castro, Phys. Rev. B **88** (2013), 245123.
- [280] Z.-X. Li, Y.-F. Jiang and H. Yao, New J. Phys. **17** (2015), 085003.

-
- [281] S. Hesselmann and S. Wessel, *Phys. Rev. B* **93** (2016), 155157.
- [282] A. G. Grushin, E. V. Castro, A. A Cortijo, F. de Juan, M. A. H. Vozmediano and B. Valenzuela, *Phys. Rev. B* **87** (2013), 085136.
- [283] R. E. Peierls, *Quantum Theory of Solids*, Clarendon Press, 1955.
- [284] C.-Y. Hou, C. Chamon and C. Mudry, *Phys. Rev. Lett.* **98** (2007), 186809.
- [285] R. Jackiw and S.-Y. Pi, *Phys. Rev. Lett.* **98** (2007), 266402.
- [286] T. Durić, N. Chancellor and I. F. Herbut, *Phys. Rev. B* **89** (2014), 165123.
- [287] S. Capponi and A. M. Läuchli, *Phys. Rev. B* **92** (2015), 085146.
- [288] D. D. Scherer, M. M. Scherer and C. Honerkamp, *Phys. Rev. B* **92** (2015), 155137.
- [289] J. Motruk, A. G. Grushin, F. de Juan and F. Pollmann, *Phys. Rev. B* **92** (2015), 085147.
- [290] Y. Jia, H. Guo, Z. Chen, S.-Q. Shen and S. Feng, *Phys. Rev. B* **88** (2013), 075101.
- [291] H. Guo and Y. Jia, *J. Phys: Condens. Matter* **26** (2014), 475601.
- [292] H.-Q. Wu, Y.-Y. He, C. Fang, Z. Y. Meng and Z.-Y. Lu, arXiv:1602.02034 (2016).
- [293] W. Zhu, S. S. Gong, T. S. Zeng, L. Fu and D. N. Sheng, arXiv:1604.07512 (2016).
- [294] W.-L. You, Y.-W. Li and S.-J. Gu, *Phys. Rev. E* **76** (2007), 022101.
- [295] P. Zanardi and N. Paunković, *Phys. Rev. E* **74** (2006), 031123.
- [296] D. Sénéchal, D. Perez and D. Plouffe, *Phys. Rev. B* **66** (2002), 075129.
- [297] C. Gros and R. Valentí, *Phys. Rev. B* **48** (1993), 418.
- [298] M. Aichhorn, H. G. Evertz, W. von der Linden and M. Potthoff, *Phys. Rev. B* **70** (2004), 235107.
- [299] M. M. Scherer, S. Uebelacker, D. D. Scherer and C. Honerkamp, *Phys. Rev. B* **86** (2012), 155415.
- [300] M. M. Scherer, S. Uebelacker and C. Honerkamp, *Phys. Rev. B* **85** (2012), 235408.
- [301] C. Hotta and N. Furukawa, *Phys. Rev. B* **74** (2006), 193107.